THESIS FOR THE DEGREE OF DOCTOR OF PHILOSOPHY

Kraft lignin valorization by hydrotreatment over Mo-based sulfided catalysts

Muhammad Abdus Salam

Department of Chemistry and Chemical Engineering

CHALMERS UNIVERSITY OF TECHNOLOGY

Gothenburg, Sweden 2022

Kraft lignin valorization by hydrotreatment over Mo-based sulfided catalysts

Muhammad Abdus Salam
ISBN: 978-91-7905-622-3

Doktorsavhandlingar vid Chalmers tekniska högskola
Ny serie nr 5088
ISSN 0346-718X

Department of Chemistry and Chemical Engineering
Chalmers University of Technology
SE-412 96 Gothenburg
Sweden
Telephone + 46 (0)31-772 1000

Cover:
Kraft lignin hydrotreatment to green chemical and fuels over the sulfided catalyst and ultra-stable Y zeolite (reproduced from ref. [1] with permission from The Royal Society of Chemistry)

Printed by Chalmers digitaltryck
Gothenburg, Sweden 2022

Kraft lignin valorization by hydrotreatment over Mo-based sulfided catalysts

MUHAMMAD ABDUS SALAM
Department of Chemistry and Chemical Engineering
Chalmers University of Technology

Abstract

The production of green fuels and chemicals from bio-based feedstock can suppress the dependency on fossil resources and help mitigate global climate challenges. Kraft lignin is a thermochemically modified natural lignin obtained from the pulping process as a byproduct. It is an underutilized fraction, often used to recover heat and energy in the current industrial practice. Chemically, it is highly rich in aromatics and thus has a huge potential to provide platform chemicals/fuels. However, the major challenge in the valorization of Kraft lignin is its recalcitrance to depolymerization due to the presence of strong interunit carbon-carbon linkages. Also, upon depolymerization, active monomeric fragments undergo repolymerization reactions forming undesired solid residue/char, thus making the transformation highly challenging.

In this context, Mo-based sulfide catalysts being sulfur tolerant and active for removing heteroatom-such as S, N, O, metals have been modified and studied with the aim to elucidate the selective cleavage of common lignin linkages, the hydrotreating potential of Kraft lignin, and upgrading of lignin derived bio-oil. The reactivity of lignin dimers, representing common lignin linkages, shows that NiMo sulfides over ultra-stable Y-zeolite support, with a higher amount of Brønsted acidity, can efficiently cleave both etheric and carbon-carbon linkages and yield deoxygenated aromatics and cycloalkanes by hydrodeoxygenation (HDO). Such hydrogenolysis, hydrocracking, and deoxygenation activity were also found to vary with the silica/alumina ratio of the Y-zeolites. The optimum activity was obtained with catalysts having a suitable balance of acidic and deoxygenation sites (metal sulfides). Additionally, one-pot hydrotreatment of Kraft lignin with a suitably functional catalyst shows a significant reduction in the repolymerization reactions, leading to a high yield of bio-oil rich in alkylbenzene and cycloalkane, a fraction suitable for example for jet fuel applications. Characterization reveals that the key function of a suitable catalyst is hydrogen activation at a lower temperature which facilitates stabilization of the lignin fragments, the moderate acidity of the catalysts, and high HDO activity of the catalyst. Furthermore, unsupported Ni/Mo-sulfides have been synthesized and found highly active for deoxygenation reaction and Kraft lignin hydrotreatment, resulting mainly from their defect-rich morphology.

Conventional Mo-based sulfide catalysts thus can be tailored to enable their effective application in the upgrading of complex biorefinery feedstocks to value added components.

Keywords: Kraft Lignin, depolymerization, char, hydrodeoxygenation, Bio-oil, metal sulfide, Y-zeolite, acidity

List of publications

This thesis is based on the content of the following appended papers:

I. **Upgrading of triglycerides, pyrolysis oil, and lignin over metal sulfide catalysts: A review on the reaction mechanism, kinetics, and catalyst deactivation.**

You Wayne Cheah, **Muhammad Abdus Salam**, Joby Sebastian, Sreetama Ghosh, Prakhar Arora, Olov Öhrman, Louise Olsson, and Derek Creaser

Manuscript

II. **NiMoS on alumina-USY zeolite for hydrotreating lignin dimers: Effect of support acidity and cleavage of C-C bond**

Muhammad Abdus Salam, Prakhar Arora, Houman Ojagh, You Wayne Cheah, Louise Olsson, and Derek Creaser

Sustainable Energy & Fuels, 2020,4, 149-163, https://doi.org/10.1039/C9SE00507B

III. **Hydrotreatment of lignin dimers over NiMoS-USY: effect of silica/alumina ratio**

Muhammad Abdus Salam, You Wayne Cheah, Phuoc Hoang Ho, Louise Olsson, and Derek Creaser

Sustainable Energy & Fuels, 2021,5, 3445-3457, https://doi.org/10.1039/D1SE00412C

IV. **Elucidating the role of NiMoS-USY during the hydrotreatment of Kraft lignin**

Muhammad Abdus Salam, You Wayne Cheah, Phuoc Hoang Ho, Abdenour Achour, Elham Nejadmoghadam, Olov Öhrman, Prakhar Arora, Louise Olsson, and Derek Creaser

Submitted

V. **Thermal annealing effects on hydrothermally synthesized unsupported MoS_2 for enhanced deoxygenation of propylguaiacol and Kraft lignin.**

You Wayne Cheah, **Muhammad Abdus Salam**, Joby Sebastian, Sreetama Ghosh, Olov Öhrman, Louise Olsson, and Derek Creaser

Sustainable Energy & Fuels, 2021,5, 5270-5286, https://doi.org/10.1039/D1SE00686J

Publications not included in this thesis

I. **Role of transition metals on MoS_2-based supported catalysts for hydrodeoxygenation (HDO) of propylguaiacol.**

You Wayne Cheah, **Muhammad Abdus Salam**, Prakhar Arora, Olov Öhrman, Derek Creaser and Louise Olsson

Sustainable Energy & Fuels, 2021, 5, 2097-2113, https://doi.org/10.1039/D1SE00184A

II. **The Effect of Si/Al Ratio on the Oxidation and Sulfur Resistance of Beta Zeolite-Supported Pt and Pd as Diesel Oxidation Catalysts**

Phuoc Hoang Ho, Jungwon Woo, Rojin Feizie Ilmasani, Muhammad Abdus Salam, Derek Creaser, and Louise Olsson

ACS Engineering Au, https://doi.org/10.1021/acsengineeringau.1c00016

III. **The role of catalyst poisons during hydrodeoxygenation of renewable oils**

Prakhar Arora, Hoda Abdolahi, You Wayne Cheah, **Muhammad Abdus Salam**, Eva Lind Grennfelt, Henrik Rådberg, Derek Creaser, and Louise Olsson

Catalysis today, 367 (2021), 28-42, https://doi.org/10.1016/j.cattod.2020.10.026

IV. **Catalytic hydrotreatment of pyrolysis oil phenolic compounds over Pt/Al_2O_3 and Pd/C**

Funkenbusch, LiLu T., Michael E. Mullins, **Muhammad Abdus Salam**, Derek Creaser, and Louise Olsson

Fuel 243 (2019): 441-448, https://doi.org/10.1016/j.fuel.2019.01.139

V. **Hydroconversion of abietic acid into value-added fuel components over sulfided NiMo catalysts with varying support acidity**

Houman Ojagh, Derek Creaser, **Muhammad Abdus Salam**, Eva Lind Grennfelt, and Louise Olsson

Fuel processing technology 190 (2019): 55-66, https://doi.org/10.1016/j.fuproc.2019.03.008

VI. **The effect of rosin acid on hydrodeoxygenation of fatty acid**

Houman Ojagh, Derek Creaser, **Muhammad Abdus Salam,** Eva Lind Grennfelt. Louise Olsson

Journal of Energy Chemistry 28 (2019) 85–94, https://doi.org/10.1016/j.jechem.2018.01.023

VII. **Influence of bio-oil phospholipid on the hydrodeoxygenation activity of $NiMoS/Al_2O_3$ catalyst.**

Muhammad Abdus Salam, Derek Creaser, Prakhar Arora, Stefanie Tamm, Eva Lind Grennfelt, Louise Olsson

Catalysts 2018, 8(10), 418; https://doi.org/10.3390/catal8100418

Contribution report

Paper I

I have planned, discussed, written part of the manuscript, and revised the entire manuscript with a focus on integrating its parts with the other authors.

Paper II

I have planned, performed the experiments, analyzed the data with co-authors, wrote the first draft of the manuscript, and revised the manuscript based on feedback from co-authors.

Paper III

I have planned, performed the experiments, analyzed the data with co-authors, wrote the first draft of the manuscript, and revised the manuscript based on feedback from co-authors.

Paper IV

I have planned, performed the experiments, analyzed the data with co-authors, wrote the first draft of the manuscript, and revised the manuscript based on feedback from co-authors.

Paper V

I have planned, performed some experiments (batch reactor, GC-MS analysis), analyzed the data with co-authors, and revised the manuscript.

List of abbreviations

BET	Brunauer Emmett Teller
BJH	Barret Joyner Halenda
BPE	Benzyl phenyl ether
BTX	Benzene-Toluene-Xylene
CUS	Coordinately Unsaturated Sites
DA	Deoxygenated aromatics
DBF	Dibenzofuran
DCOx	Decarboxylation and decarbonylation
DHDPM	4, 4’ dihydroxydiphenylmethane
DDO	Direct HDO
DMDS	Dimethyl disulfide
DME	Dimethyl ether
EDX	Energy dispersive X-ray
EMCCD	Electron Multiplying Charge-Coupled Device
FAME	Fatty acid methyl ester
FID	Flame ionization detector
FTIR	Fourier transform infrared spectroscopy
GC	Gas chromatography
GHG	Greenhouse gas
HAADF	High angle annular dark field
HEFA	Hydroprocessed esters and fatty acids
HDO	Hydrodeoxygenation
HDM	Hydrodemetallization
HDN	Hydrodenitrogenation
HDS	Hydrodesulfurization
HVO	Hydrotreated Vegetable Oil
HVGO	Heavy vacuum gas oil
ICP-SFMS	Inductively coupled plasma sector field mass spectrometry
LCO	Light cycle oil
MFC	Mass Flow Controllers
MS	Mass spectrometer
PPE	Phenethyl phenyl ether
PG	4-Propylguaiacol
TAN	Total acid number
TMS	Transition metal sulfides
TOF	Turn Over Frequencey
TCD	Thermal conductivity detector
TEM	Transmission electron microscopy
TG	Triglycerides

TPO	Temperature programmed oxidation
TPD	Temperature programmed desorption
XPS	X-ray photoelectron spectroscopy
XRD	X-ray powder diffraction
USY	Ultra-stable Y zeolite
2-PP	2-phenylphenol
2O compounds	4-Propylcatechol

Contents

1 Introduction

1.1 Background

Limited fossil-based resources, increasing greenhouse gas (GHG) emissions and their impact on global climate change have shifted the focus towards a fossil-free sustainable society. As shown in **Fig.1**, historic global CO_2 emission increased by ~40% since 2000 [2]. Considering the announced pledges, global emissions can only be reduced by 40% by 2050 [2]. In the EU, as of 2020, ~31% lower GHG emissions were achieved compared to 1990 which is well below the pre-estimated target [3]. However, based on the 2050 green deal of 'net-zero emission' a significant amount of GHG emissions needs to be reduced. Thus, ambitious goals, combined with stringent policies are set to propel stakeholders to surge energy efficiency and cut GHG emissions to limit the global temperature within the range of 1.5°C.

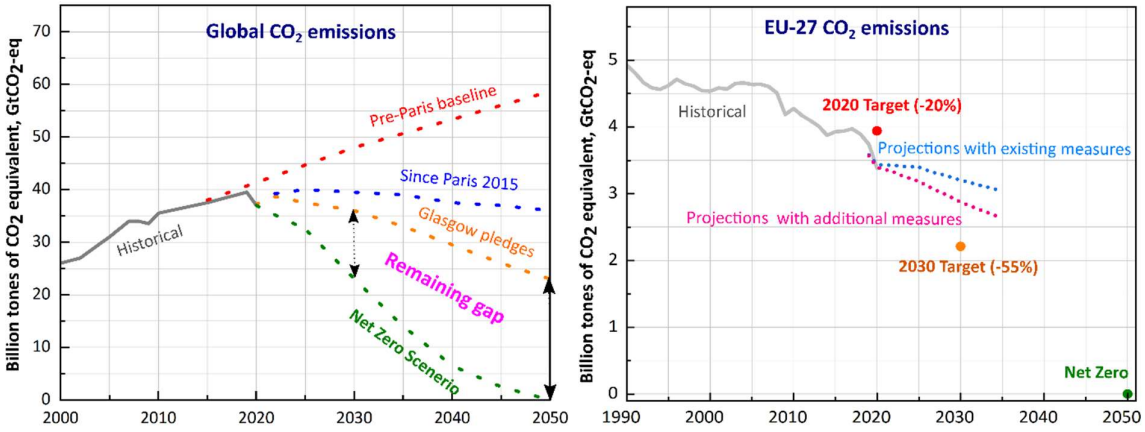

Fig.1 Global and EU GHG emissions trend and scenario adapted from IEA energy outlook [2] and EU trends/projections [3].

Among others, the transport sector contributes to ~25% of the overall GHG emissions mainly due to the combustion of fossil-derived fuels in the road, aviation, and maritime transport. One of the UN sustainable development goals is to increase the renewable energy share to achieve carbon neutrality. Such energy sources include resources like wind, solar, geothermal, biomass, and biofuels, etc. The liquid biofuel derived from biomass can propel the transport sector where electromobility seems impractical especially for heavy-duty vehicles, aviation, and maritime transport [4]. Advanced liquid biofuels can play a significant role in this regard

as predicted in the different scenarios illustrated in **Fig.2.** The net-zero emission scenario predicts that 90% of the total biofuel will be dominated by an advanced type of biofuel.

Conventional liquid biofuels are mainly derived from food-grade biomass like sugarcane, corn, or edible vegetable oil. In the long run, they are not sustainable and risk food security. Typical upgrading processes of these feedstocks are fermentation, transesterification, extraction, and distillation, etc. Fermentation (to ethanol) is a slow but enzyme-specific process that is challenging to scale up, but product yield/selectivity is rather high [5]. Transesterification yields so-called FAME type biodiesel which consists of fatty acid methyl esters. EU limits the maximum blending of FAME in Petro-diesel fuel to 7% (v/v), due to its high content of oxygenates that cause poor cold flow properties and incompatibilities with the fossil fuel and engines [6].

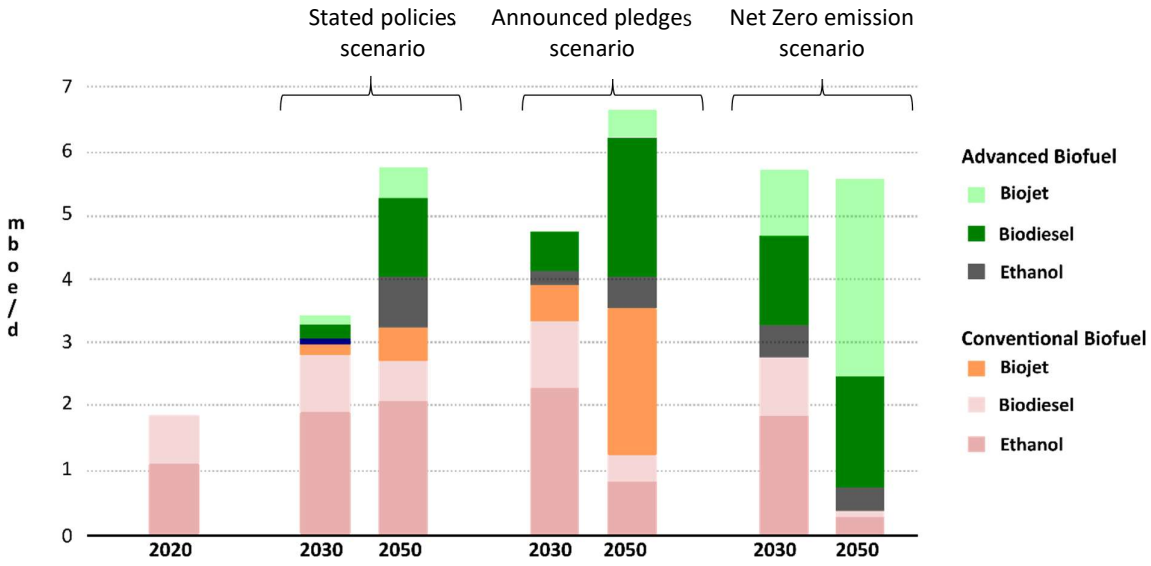

Fig.2 Liquid biofuel demand and trends adapted from IEA energy outlook [2].

On other hand, advanced liquid biofuels can be derived from lignocellulosic biomass, agricultural and forest residue, non-edible oil, waste cooking oil, animal fat, and algal biomass, etc. Typical upgrading processes involve pyrolysis, hydropyrolysis, hydrothermal/reductive/ liquefaction, gasification, and hydroprocessing, etc. Thermochemical processes such as fast pyrolysis yield bio-oil in a very short residence time but with a higher oxygen content which makes it unstable even during storage. Hence further upgrading is inevitable. Gasification of biomass to syngas is another alternative, where subsequent Fisher-Tropsch synthesis produces synthetic diesel or bio-methanol/bio-DME (dimethyl ether) [7]. Hydroprocessing of triglycerides yields advanced biodiesel known as hydroprocessed esters and fatty acids (HEFA) or hydrotreated vegetable oils (HVO) mainly via hydrogenation and deoxygenation. Often the process is termed hydrodeoxygenation (HDO). This is a unique catalytic process where the product meets or exceeds the quality of petro-diesel and is thus compatible with existing engines, as well as upstream (refinery) and downstream (refueling) infrastructures. The

ensuing advantages of this process include a significant reduction in GHG and sulfur emission, as well as better storage and cold flow properties.

Among the above technologies, the HEFA/HVO process has been commercialized by Neste (NEXBTL^{TM}), Diamond Green, UPM, Emerald Biofuels, Haldor Topsoe (HydroFlex^{TM}), ENI (Ecofining^{TM}), Total, and Preem around the globe as stand-alone processes or with co-processing of conventional petroleum. Fast pyrolysis bio-oil processes are under commercial trial for advanced biofuel production [8].

The biorefinery byproduct, lignin (e.g., Kraft, lignosulfonate, or organosolv) has good potential to be a source of advanced biofuel. Among the types, Kraft lignin constitutes 85% of the worldwide lignin production [9]. Also, about 98% of lignin produced worldwide is incinerated [10]. However, Kraft Lignin is highly rich in aromatics with aliphatic moieties pertinent to valorize to platform chemicals (e.g., BTX) and fuels rather than heat and energy recovery as is the practice today. In recent years, this potential feedstock has been exploited in research using different methods/catalysts, and knowledge concerning its conversion to higher-value products is growing at a rapid rate. One such process is catalytic hydrotreatment where depolymerization of Kraft lignin and upgradation can take place in a single or multi-step process [11, 12]. However, the tangible challenge is to develop a stable catalytic material capable of depolymerizing the strong interunit lignin linkages and subsequent processing steps to upgrade the fragments to target molecules. On the other hand, the high reactivity of depolymerized lignin fragments makes this transformation difficult due to their recombination to form solid residue or char which can deactivate the catalyst prematurely. On the other hand, impurities in Kraft lignin e.g., sulfur (1-3 wt.%) limit the number of catalysts suitable for its valorization. Therefore, fundamental insights correlating the physicochemical properties of catalytic materials to their activity can boost the understanding of novel catalyst design to achieve target products with higher selectivity.

1.2 Aim and scope

The objective of this work is to examine the upgrading of lignin and lignin derived bio-oil to valuable liquid fuel components via catalytic hydrotreatment and gain critical insights into the activity, selectivity, and stability of the employed catalyst.

Specifically, the focus is on sulfided NiMo catalysts and their combination with ultra-stable Y zeolites as the support materials. Since lignin is a 3D biopolymer having interunit C-C and C-O-C linkages, the reactivity of these linkages was first evaluated using model lignin dimers and sulfided catalysts with varying support acidity and textural properties (Paper II and Paper III). Later, Kraft lignin hydrotreatment was assessed using certain catalysts based on their catalytic activity for the lignin dimers (Paper IV). The role of the catalyst components was studied by comparing supported and unsupported Mo-based sulfided catalysts (Paper IV and Paper V) for Kraft lignin. It has been identified that hydrotreatment yields bio-oil containing oxygenated molecules such as alkylphenols and guaiacolics (e.g., propylguaiacol). Henceforth, the hydrotreating activity of lignin derived bio-oil has further been investigated using unsupported

Mo-sulfides (Paper V). All the hydrotreatment studies were limited to a batch reactor run. In addition, detailed catalyst characterization of the catalyst was conducted to gain insight into how the physicochemical properties of the materials are related to their catalytic activity and selectivity.

1.3 Outline

In this thesis, the focus is given to valorizing Kraft lignin via catalytic hydrotreatment employing sulfided NiMo and Y zeolite-based catalysts.

Given the context described in **Chapter 1,** the thesis is organized into the following Chapters:

Chapter 2 describes the background regarding the catalytic hydrotreatment of renewable feedstocks including Kraft lignin and lignin derived bio-oils with emphasis on the use of transition metal sulfide (TMS) catalysts. The role of TMS catalysts and their deactivation pathways are also highlighted in brief.

Chapter 3 explains the experimental techniques used in this thesis. In general, N_2 physisorption for specific surface area and textural properties, temperature program desorption for acidity, X-ray diffraction for crystallinity, X-ray photoelectron spectroscopy for oxidate state, Raman, FTIR spectroscopy for characteristic structural vibration, scanning and transmission electron microscopies to understand the dispersion and morphology of the synthesized catalysts were used.

Chapter 4 discusses the key findings and includes a critical explanation of the results from the appended papers.

Chapter 5 includes the concluding remarks and outlook, respectively.

2 Catalytic Hydrotreatment

2.1 Catalytic Hydrodeoxygenation (HDO)

Hydrotreating is one of the core processes in a complex refinery to remove impurities such as S (hydrodesulfurization, HDS), N (hydrodenitrogenation, HDN), O (hydrodeoxygenation, HDO), and metals such as Ni, and V (hydrodemetallization, HDM) from fossil-based feedstocks in the presence of H_2 at high temperature and pressure. In fossil-derived feedstocks, the amount of oxygen-containing impurities is very small compared to others. As a result, hydrodeoxygenation (HDO) has also been employed to remove oxygen from bio-based feedstocks (e.g. pyrolysis oil, vegetable oil, tall oil, etc.) which are rich in oxygen (~45%) [13, 14]. The high amount of oxygenates in the bio-oil leads to undesired properties such as high viscosity, a poor heating value, corrosiveness due to a high total acid number (TAN), thermal instability, and a tendency to polymerize during storage and transportation [15, 16]. Such detrimental properties impede their direct utilization as renewable fuels.

Catalytic oxygen removal typically occurs with the formation of H_2O, CO, and CO_2 in the presence of hydrogen at elevated temperatures and pressure. Deoxygenation giving water is often termed as direct-HDO (DDO) while others such as decarbonylation (removal as CO) and decarboxylation (removal as CO_2) are collectively referred to as decarbonation [17, 18]. The process thus reduces the oxygen content and yields hydrocarbons to be used as a drop-in fuel component. Henceforth, HDO has received widespread research focus exploring the application of catalytic materials to upgrade oxygen-rich renewables to fuels and chemicals. It is important to note that the HDO reaction-chemistry and resulting products heavily depend on the catalytic material, reaction conditions, reactor type, and type of feedstocks to be upgraded. For example, a saturated fatty acid molecule can undergo direct-HDO or decarbonation routes while for phenol (C_6H_5OH), ring hydrogenation can compete with DDO without any decarboxylation/ decarbonylation reaction. Other reactions during HDO include a network of demethoxylation, demethylation, hydrogenolysis, dehydration, hydrocracking, transalkylation, ring opening, isomerization, and condensation or polymerization (i.e., coking), etc. Also, in the gas phase, the reverse water gas shift reaction and methanation can occur to a small degree.

2.2 HDO using Transition metal sulfides (TMS)

Transition metal sulfide catalysts are typically used for HDS and HDN applications. Analogous to an HDS catalyst, conventional Mo (or W)S_2 and Ni or Co-promoted MoS_2 on γ-Al_2O_3 have also been extensively studied for HDO applications [16, 19-23]. Since the catalyst also has a high HDS activity, the residual sulfur content in the products can be maintained at a very low level. The role of metal sulfides (e.g., MoS_2/WS_2), promoters, support materials, and reaction conditions play a significant role during such an upgrading process. Unsupported TMS catalysts have also been studied for such applications without any support materials, hence exclusive of the metal-support interaction, support properties (e.g., acidity), and complexity in the determination of active sites [24-26]. Eni Slurry Technology (EST) is one such example where nanosized finely dispersed MoS_2 shows high hydrogenation activity (400-500 °C, 150 bar) for heavy vacuum residue [27]. Understanding the TMS structure and resulting morphology whether supported or unsupported is thus vital to obtain mechanistic insights during HDO.

In a typical MoS_2 layer structure, Mo atomic planes are sandwiched between two S atomic planes. Such layers are anisotropic, can grow on top of each other, and are connected via weak van-der-Waals forces. The top and bottom stacks are usually called basal planes and the adjacent ends are called edges. In this way, MoS_2 can assume rhombohedral (3R), hexagonal (2H), and octahedral (IT) structures with different physical properties of which 2H-MoS_2 is common for hydrotreating catalysts [28]. Also, the growth of such a structure can be influenced by the presence of support materials giving rise to Type-I (strong-interaction with support), and Type-II sites (weak interaction with support) [29, 30]. The reactive sites of MoS_2 originate from the edge, corner Mo atoms having sulfur vacancies or coordinately unsaturated sites (CUS), and the presence of sulfhydryl groups. According to the edge decoration model, promoter atoms (Ni/Co) preferentially occupy the edge and corner sites to form the so-called active Ni/Co-promoted MoS_2 (Ni-Mo-S) phase in hexagonally shaped MoS_2 nano-sized crystals [23, 31]. It is postulated that Ni or Co promotion facilitates the formation of sulfur vacancies or CUS (**Fig.3**) via d-electron donation and weakening the Mo-S bonds [22, 32]. The higher electrophilic nature of Mo (acts as Lewis acid) thus interacts with oxygenate molecules [32, 33]. In the presence of hydrogen, metal sulfides can also form metal hydrides on the catalytic surface (**Fig.3**). The activity of the catalyst thus depends on the type/combination of sites present which can be engineered by parameters such as promoters, support, additives, and activating conditions. In addition, the size, shapes, morphologies of the resultant MoS_2 slabs are important parameters. Also, the orientation/mode of adsorption of the reactant molecules to the active sites defines the favored reaction chemistry over the catalyst.

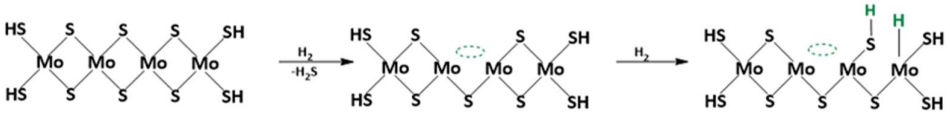

Fig.3 Formation of sulfur vacancy (green dotted circles), hydrides, and sulfhydryl groups.

2.3 HDO of lignin/lignin derived bio-oil

Lignin is the second most abundant natural polymeric material highly rich in aromatics that contributes to 15-30% of plant biomass. Chemically it is a three-dimensional cross-linked biopolymer consisting of three different propyl phenol units (monolignols), mainly coniferyl alcohol, sinapyl alcohol, and p-coumaryl alcohol linked via etheric C-O (α-O-4, β-O-4, 4-O-5, etc.) and C-C linkages (5-5', β-1, β-5, β-β, etc.) [34-36]. In a typical native lignin, β-O-4 linkages constitute 45-60% of the overall linkages [35]. Such heterogeneity in the structure makes it stiff and recalcitrant to further utilization. Typical linkages of lignin are shown in **Fig.4.**

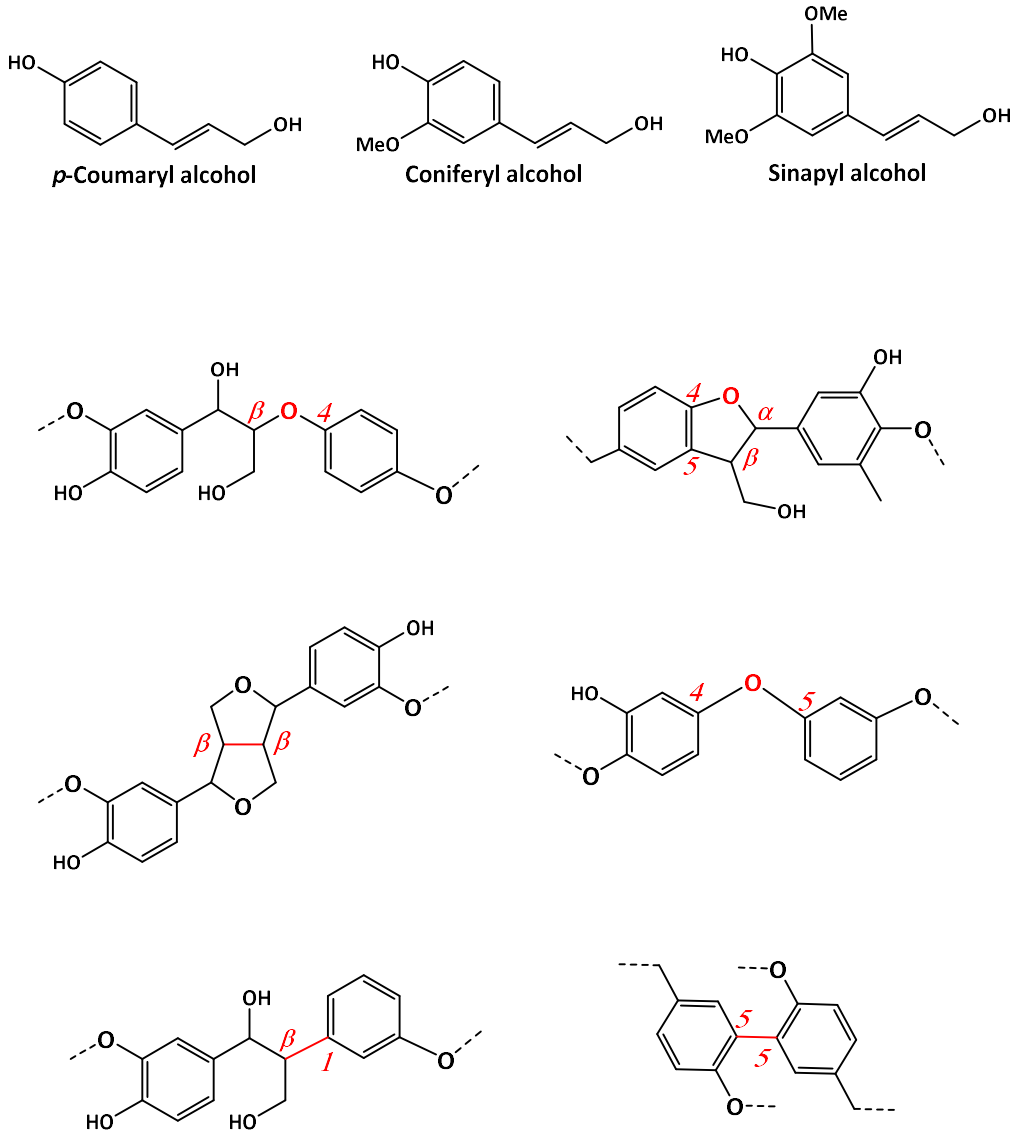

Fig.4 Building blocks of lignin and typical lignin linkages.

In the biorefinery, large amounts of lignin (e.g., Kraft/Lignosulfonate/Organosolv) can be separated chemically as a byproduct while making pulp or cellulosic ethanol. The current industrial practice is to burn this carbon-rich byproduct or part of it for heating and power generation purposes, despite its enormous potential as a renewable feedstock to derive green chemicals and biofuels. Research efforts have been explored for both native and technical lignin (lignin from biorefinery or processed native lignin) to depolymerize and upgrade it via thermal (e.g. fast pyrolysis), oxidative, solvolytic, acid/base-catalyzed, and reductive methods [36]. Efficient depolymerization requires selective cleavage of lignin linkages and suppression of undesired (repolymerization) reactions. Lignin derived bio-oils thus contain monophenols (alkyl/methoxy substituted), dimers, and phenolic oligomers. New functional groups/linkages (e.g. stilbene, thiols, carbohydrate, sulfonate, etc.) are often reported to be found in the modified or technical lignin depending on the processing conditions [37]. These add additional complications for the further upgradation process. For example, S present in Kraft lignin (1-3 wt.%) and lignosulfonate lignin (4-8 wt.%) can poison noble metal catalysts during upgrading. Hence a robust catalyst capable to depolymerize the residual linkages and promote subsequent deoxygenation is crucial to obtain stable and advanced biofuels.

Catalytic hydrotreatment (e.g., HDO), a reductive process has been examined to depolymerize lignin linkages and deoxygenate the phenolic monomers simultaneously to produce specialty chemicals and biofuels. HDO of phenols [38-44], anisole [42, 45-48], substituted phenols (cresols, guaiacols, syringols, eugenols, etc.) [21, 39, 42, 49-61] and lignin dimers [62-67] has been demonstrated via noble metals (Pt, Pd, Ru, Re, Ir, etc.),metal-sulfides, carbides, nitrides, and phosphides over various support materials (carbon, Al_2O_3, ZrO_2, TiO_2, ZrO_2-SiO_2, SiO_2-Al_2O_3, zeolites, mesoporous silicates, etc.). Typical products are bioarenes (e.g. benzene, toluene, xylene, ethylbenzene, etc.) [46, 53] and cycloalkanes (e.g. C6-C9) in the gasoline range [39, 68]. Bio-arenes for e.g. alkylbenzene can be blended as fuel additives [69]. However, the complete range of products and selectivity solely depends upon the favored chemistry over the catalyst-support combination i.e., physiochemical properties and reaction conditions. Besides, understanding the influence of support acidity, metal-support interaction, pore accessibility, and stability of the catalysts are tangible challenges in defining the catalytic activity and selectivity [41, 70, 71]. For example noble metal-based catalysts (e.g. Pd/C and HZSM-5) usually lead to phenolic ring hydrogenation and preferentially yield cycloalkanes via acid induced dehydration [39].

Transition metals Co or Ni promoted Mo/WS_2 (supported or unsupported) typically favor both DDO-HYD and yield a mixture of alicyclics and aromatics from lignin derived phenolics (e.g., alkylphenols) [24, 26, 38, 72-77]. In a typical catalytic cycle for DDO (shown in **Fig.5**), oxygenate molecules (e.g., phenol) bind to vacant sulfur sites. Proton donation from the sulfhydryl groups (or metal hydride groups) creates a carbocation in the ortho position of the phenyl group. Stabilization of the carbocation via benzene formation and water removal completes the catalytic cycle.

Sulfided catalysts have also been found active for hydrogenolysis of C-O-C and C-C lignin linkages [63, 78-81]. The strength of lignin etheric linkages (sp^3 hybridized) based on bond dissociation energies are in the order: 4-O-5 (ca. 330 KJ mol^{-1})>β-O-4 (ca. 289 KJ mol^{-1}) >α-O-4 (ca. 218 KJ mol^{-1}) while for a C-C linkage it is much higher (e.g. ca. 490 KJ mol^{-1} for 5-5' linkage) [37, 82, 83]. Many catalysts have been reported to be capable of breaking down etheric linkages, while very few can break C-C linkages in lignin [64, 65]. Shuai et al [78] claimed the successful C-C cleavage of a model dimer, dimethylguaiacylmethane to phenolic monomers. $NiMoS_2$/C has been reported to cleave both C-O and C-C linkages in Kraft lignin to yield both monomeric and dimeric phenols [84]. Zeolites (H-BEA, HZSM-5, H-USY) have also been explored for hydrocracking reactions (C-C cleavage) and biomass fast pyrolysis [85-87]. A combination of modified/mesoporous zeolites and NiMo sulfide catalyst has been reported to cause C-C breakdown via hydrogenation, ring opening reactions of heavy vacuum gas oil (HVGO), light cycle oil (LCO), and related studies [88-95]. Advantages with zeolites are their tunable acidity, shape-selective pore sizes, and thermal and hydrothermal stability [86, 96]. However, the major challenges for complex feedstocks are their textural properties, diffusion limitations, and deactivation via coking [41, 70]. Morphologies of the NiMoS phases and proximity of the active sites (e.g. acid sites and sulfur vacancy) can play a vital role in governing the activity of the catalyst [97]. Therefore, a robust catalyst with the ability to cleave both etheric and C-C linkages would be ideal to valorize lignin/lignin derived bio-oil.

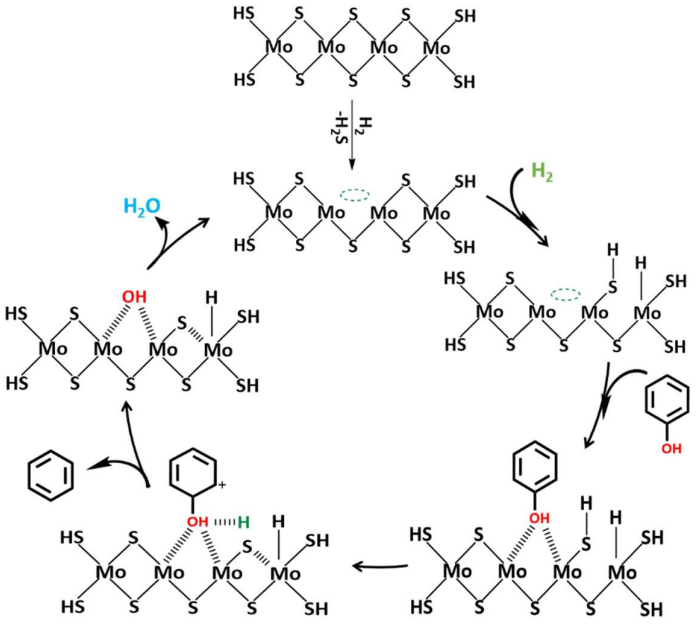

Fig.5 Phenol DDO over Ni promoted MoS_2 adapted from ref [22].

The sulfide catalysts have also been evaluated for the hydrotreatment of lignin. Pine Kraft lignin has been investigated over sulfided $CoMo/Al_2O_3$ at 380 °C and 69 bar of H_2 in a batch reactor and reported to yield ~21 wt. % of monomer with ~9 wt. % phenol after 1h of

hydrotreatment. Horácek et al. [98] investigated hydrolysis (organosolv) /lignosulfonate lignin over sulfided NiMoP/γ-Al_2O_3 in a semi-continuous reactor and hydrotreatment (380 °C, 40 bar H_2) resulted in the formation of aromatic hydrocarbons and naphthenes having a solid residue of ~20 wt.% at the end of 4h. Sulfided CoMo/Al_2O_3 has also been assessed using a modified semi-continuous setup with a reflux condenser allowing the release of volatiles and reaction water to drive the reaction and avoid catalyst deactivation [99]. A solvent-free approach under high temperature and pressure using sulfided NiMo, and CoMo over aluminosilicate and Cr_2O_3/Al_2O_3, ZSM-5, activated carbon, MgO-La_2O_3 has a variable yield of depolymerized product (14-26.4 wt.%) with low solid residues [100-102]. Oasmaa et al. [100] compares the hydrotreatment (395-400 °C, 100 bar of initial H_2 pressure, 0.3-0.6h) of five technical lignin (pine Kraft, birch Kraft, and organocell) using sulfided NiMo/aluminosilicate and 20 wt.% Cr_2O_3/Al_2O_3. The yield of liquefied bio-oil follows in the order of organocell>pine Kraft> birch Kraft lignin could be attributed due to their structural variation. Hydrogen-donor solvents (e.g., methanol) have also shown promising monomer yields (15-35 wt.%) over sulfided NiW/AC with traces of char but with DCM and DMSO soluble solids having high molecular weights (2725 g/mol) [103]. Unsupported Ni, Co, Ag, and Mo sulfides have also been explored using alkali lignin in ethanol and the results showed high yields of bio-oil (~85%) with low solid residues (~9 wt.%). Reductive liquefaction of lignosulfonate lignin over oxidic NiMo/Al_2O_3 in supercritical ethanol (310 °C, 26 bar H_2, 3h) shows high oil yield (88 wt.%) and a char yield of about 15 wt.% [104]. The above studies infer that lignin valorization is largely affected by many factors such as type/source of lignin, presence of impurities (S, Na, K, etc.), the chosen metal sulfides, support properties, type of reactors, solvent, and operating conditions chosen during the hydrotreatment.

2.4 Deactivation of HDO catalysts

Possible pathways for catalyst deactivations are poisoning, fouling or physical blockage, leaching or vapor formation, sintering, attrition, and vapor-solid/solid-solid interactions [105-107]. Transition metal sulfides during HDO deactivate mainly due to loss in sulfidity of the catalyst, poisoning via impurities present in the renewables, presence of a large amount of water which may cause oxidation of sulfide phase, and coking.

The activity of the Ni or Co-promoted MoS_2 (supported/unsupported) depends on the labile nature of the sulfur vacancies which are prone to accept oxygenate molecules during HDO. Strongly bound oxygenates can convert the sulfided catalyst to thermodynamically stable oxides or oxysulfide's which are less active. A continuous supply of sulfiding agents (e.g., dimethyl disulfide, H_2S) has been found to restore the activity of the catalysts for aliphatic esters and phenol [108-110]. However, the addition of sulfur contaminates the product. Since the catalyst has high HDS activity, the final product usually only contains trace amounts of sulfur. The addition of DMDS or H_2S also changes the product selectivity e.g., via the decarboxylation route while upgrading esters and fatty acids [18, 21, 108].

Bio-oil/Kraft lignin impurities, including alkali, alkaline-earth metals (Na, Ca, Mg, K), phosphorus, phospholipid, chlorine, and Fe have been explored as possible poisons for HDO.

Severe irreversible K deactivation due to the occupation of vacant sites near edges of MoS_2 has been reported to occur for $NiMoS_2/ZrO_2$ while for the same catalyst chlorine (Cl) deactivation was reversible [110]. Fe reportedly preferentially deactivates the Ni promotion of MoS_2 over γ-Al_2O_3 while upgrading fatty acids [17]. Trap grease phospholipid (acidic due to less alkali metals) was shown to cause severe deactivation of a commercial CoMoS/γ-Al_2O_3 catalyst and eventual failure of the experiment due to coking and plugging of the reactor while upgrading rapeseed oil [105]. Nitrogen-containing compounds such as amines, pyridines, and their derivatives, quinolines have been reported as catalyst poisons [38]. Laurent and Delmon [21] showed the severe deactivation of Co/NiMoS- γ-Al_2O_3 by a diamine.

Bio-oil is highly rich in oxygenates. Also, lignin can have ~30 wt.% oxygen in its structure. Therefore, water generated during hydrotreatment may have a negative impact on the activity and stability of the sulfide phase and support materials. A combined experimental and DFT study shows that Co-promoted MoS_2 has better water stability which prevents partial oxidation of the active phase to sulfate/oxidized layers via sulfur-oxygen exchange [111]. However, partial oxidation of Ni phases has been reported to be the main cause of the NiMoS deactivation over γ-alumina [112]. Also, γ-alumina reportedly crystallizes to a hydrated boehmite phase in the presence of water. Coumans and Hensen et al. [18] showed that in-situ generated water (up to ~33000 ppm) has little effect on sulfided NiMo/γ-Al_2O_3 during HDO of methyl oleate owing to indemnifying effect of H_2S.

One of the major challenges in catalysis is the coking of the HDO catalysts. It has been demonstrated that the coking on the catalyst surface results from undesired side reactions (e.g., cracking, aromatization, dehydrogenation, cyclization, and condensation, etc.) of the chemisorbed species. Physiochemical properties of the catalyst (e.g. acidity), type of precursor molecule (e.g. alkenes, aromatics, oxygenates) and the reaction conditions affect the coke formation [113]. The carbonaceous deposits at low temperature (<200 °C) usually form via condensation and rearrangement reactions and strongly depend on the type of feeds/reactants, while at high temperature (>350 °C) they are polyaromatics formed via additional dehydrogenation and hydrogen transfer reactions [114]. Coke formation ends up blocking the active sites and plugging the pores when deactivate the catalyst.

Apart from this, separation of the promoter, sintering of the active phase (both supported/unsupported catalysts), support acidity, or basicity can further influence the catalyst deactivation [115-117]. During lignin depolymerization, reactive oxygenate fragments often undergo coupling reactions forming solid residue/char that can deactivate the catalyst employed for hydrotreatment.

3 Experimental

3.1 Catalyst Preparation

Supported catalysts containing Ni and Mo were prepared by a wet impregnation process using calcined γ-Al_2O_3 (PURALOX®, Sasol) and ultra-stable Y zeolite with various SiO_2/Al_2O_3 ratios (Zeolyst International) [118-120]. Aqueous solutions of $(NH_4)_6Mo_7O_{24}.4H_2O$ (99%, Sigma-Aldrich) and $Ni(NO_3)_2.6H_2O$ (98%, Sigma-Aldrich) were used as the precursors for the metals. Mo solution was first added dropwise to an aqueous mixture of the support (γ-Al_2O_3 or ultra-stable Y zeolite or a physical mixture of both) under stirring followed by drying and calcination in air at 450 °C reached with a ramp of 5°C min^{-1} for 4 h. In the second step, Ni solution was added similarly to the Mo impregnated supports. Again, after drying, the material was calcined. This protocol was followed for Papers II and III while for Paper IV, co-impregnation of the Mo and Ni precursor solution was used instead followed by drying and calcination as mentioned above.

Unsupported MoS_2 (Paper V) and Ni-promoted MoS_2 (Paper IV) were prepared via a modified hydrothermal method. A required amount of ammonium heptamolybdate tetrahydrate (>99%, Sigma Aldrich), $Ni(NO_3)_2.6H_2O$ (for $NiMoS_2$ only), and thiourea were dissolved in ultra-pure water for the synthesis. The pH of the resultant solution was modified via HCl (35 wt.%, VWR) to 0.8 and transferred to 70-ml or 300-ml Teflon-liners. The liner was then placed in an autoclave reactor and heated in an oven at 200 °C for 12 h or 24 h. The pH unmodified solution also went through these steps to examine the effect of the acid modification. As-synthesized MoS_2 or NiMoS were separated by filtration, washed thoroughly with absolute ethanol, and dried under vacuum at 50 °C overnight. In addition, dried MoS_2 was further annealed at 400 °C for 2 h under a nitrogen atmosphere to examine the influence of morphological changes caused by the annealing (Paper V). Following terminology was used for the above synthesized catalysts,

3.2 Feedstocks

Benzyl phenyl ether (98%, Sigma Aldrich), 2-phenethyl phenyl ether (98%, Frinton Laboratories Inc.), 2,2'-biphenol (99%, Sigma Aldrich), 4,4'-dihydroxydiphenylmethane, 2-phenylphenol were used to mimic etheric and carbon-carbon linkages of native/technical lignin's shown in **Fig.6** (paper II and III). In paper IV, Kraft lignin (Sigma Aldrich) was used as the starting material. In paper V, 4-propyl guaiacol and Kraft lignin were used as the feeds to outline the catalytic transformation.

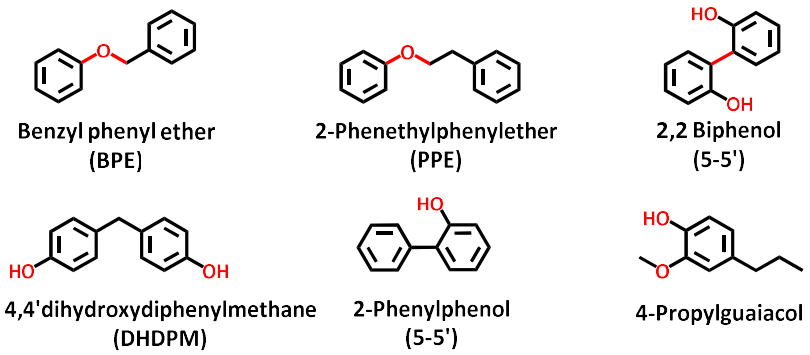

Fig.6 Model compounds used to mimic ether and C-C linkages and lignin derived bio-oil

3.3 Catalytic Activity Measurements

The activity experiments were carried out in a 300 ml batch reactor (300 ml, Parr Instruments). The reactor consists of a magnetically driven internal stirrer, inlets for H_2/N_2 gas, a gas outlet with scrubber, and a liquid sampling line to collect a small volume of reaction samples (0.5- 2 ml). Before the activity experiment, calcined supported catalyst (0.5-0.75 g) was sulfided in the reactor using dimethyl disulfide ((0.5-0.75 ml, ≥99.5%, Sigma-Aldrich) and 20 bar of H_2 (99.9%, AGA) at 613 K for 4 h. Solvent (Dodecane or hexadecane) was added immediately after the sulfidation to avoid air exposure. The reactor, after loading with the reactants (models compounds/Kraft lignin) was flushed three times with N_2 followed by three times with H_2 before pressurizing it to 0.1-40 bar (based on the feed) using H_2 at room temperature. The stirring was maintained low (50 rpm) for model compound studies to dissipate the heat and minimize reaction during the heating while for Kraft lignin it was set to 1000 rpm from the beginning to prevent lignin sedimentation at the reactor bottom and sintering during heating.

For model compound studies, the final reactor condition was maintained at 50 bar, 300-320°C, 1000 rpm of stirring for 5 or 6 h. For Kraft lignin, the reactor reached a pressure of 72-80 bar when heated to 340-400 °C (35-40 bar at 25°C) without any further pressure adjustment. For model studies, multiple samples (0.5-2 ml) were collected at different time intervals which caused a temporary pressure to drop of ca. 1-2 bar, which was compensated by repressurizing to 50 bar following each sample withdrawal. No samples were withdrawn for Kraft lignin experiments. After 5 or 6 h, the reaction was stopped by rapid cooling to room temperature.

At this point, the gas sample was collected in a stainless-steel gas cylinder before depressurizing the reactor. The reactor was finally purged with N_2 before collecting the reaction products, catalysts, and residual solids. For model studies, the recovered catalyst (via filtration) was washed with volatile solvents (diethyl ether/acetone), dried, and used for further characterization. For Kraft lignin studies, the bio-oil phase, rich in hexadecane, was recovered via vacuum filtration. The residual solids/catalysts in the reactor and from filtration were then thoroughly washed with acetone and the derived fraction is termed as the aqueous phase, rich in acetone. The residue was then dried, washed with dimethyl sulfoxide (≥99.9%, VWR) to remove any unconverted lignin, and finally washed with acetone before drying for further characterization. The workup procedure is shown in **Fig.7**

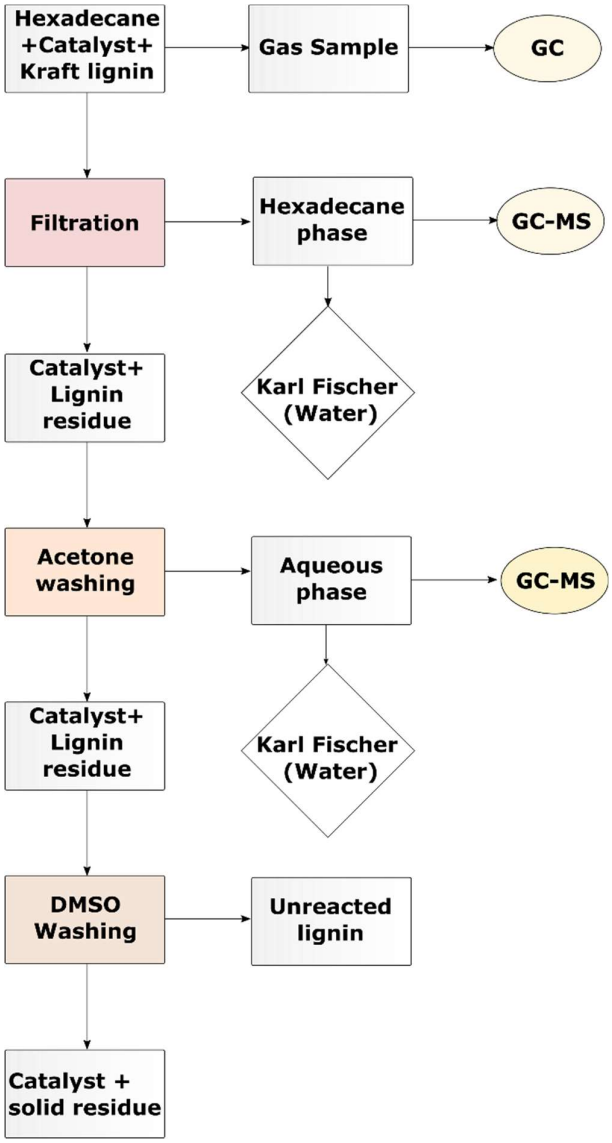

Fig. 7 Kraft lignin hydrotreatment workup procedure.

3.4 Product analysis

The reaction samples (paper II and V) collected from each experiment were analyzed by a gas chromatograph-mass spectrometer, GC-MS (Agilent 7890–5977A, Agilent). The GC has a non-polar HP-5 column (30 m x 250µm x 0.25 µm) equipped with flame ionization detector, FID (set point: 335 °C) and mass spectrometer (5977A, Agilent) for species identification via the NIST library. In a typical method, the initial oven temperature was kept at 100 °C for 1 min which is then heated at 10 °C/min to 190 °C followed by ramping at 30 °C/min to 300 °C and held there for 1.3 min for a total analysis time of 15 min/sample. At the GC inlet, the injector temperature was maintained at 325 °C. Liquid samples (paper III) were also analyzed by a modified GC-MS column, DB-5 (30 m × 250 µm × 0.25 µm), and BPX-50 column (2.5 m × 100 µm × 0.1 µm) with similar settings (oven temperature: 70°C for 1 min, 15 °C/min to 300°C for 5 min). Quantification is based on the standard calibration of reactants, intermediates, and products identified by GC-MS. Following equations were used for model compound studies (paper II, III, and V) to account for the conversion (X), yield, and product selectivity:

$$\text{Conversion, X (\%)} = \left(1 - \frac{moles\ of\ reactant\ left}{Initial\ moles\ of\ reactant}\right) \times 100$$

$$\text{Yield (\%)} = \frac{moles\ of\ product}{moles\ of\ reactant\ in\ feed} \times 100$$

$$\text{Selectivity (\%)} = \frac{(moles\ of\ product)i}{\sum_i^n (moles\ of\ product)i} \times 100$$

$$\text{Initial rate of reaction} = \frac{mmol\ of\ ethylbenzene\ and\ phenol\ formed\ at\ 35\ min}{Time\ (h).mass\ of\ catalyst}$$

$$\text{Initial rate of transalkylation} = \frac{mmol\ of\ total\ phenolic\ dimers\ formed\ at\ 35\ min}{Time\ (h).mass\ of\ catalyst}$$

$$\text{Turn over frequency (TOF)} = \frac{Initial\ rate\ of\ reaction\ at\ 35\ min}{Total\ acidity\ of\ the\ catalyst}$$

The liquid samples obtained from the Kraft lignin hydrotreatment (paper IV and V) were analyzed using a 2D GC × GC-MS-FID (Agilent 7890B–5977A, Agilent) consisting of a long mid-polar column VF-1701MS (30 m × 250 µm × 0.25 µm), a short non-polar column DB-5MS (1.2 m × 150 µm × 0.15 µm) and a thermal modulator with a hot and cold jet of nitrogen. The GC oven starts at 40°C for 1 min followed by ramping to 280 °C with a rate of 2°C/min. Thermal modulations and FID were maintained at 8s and 250 °C respectively. The quantification of the products was based on the detailed analysis of the compounds evolved in the 2D GC images via GC image software. Standard calibration of phenol, alkylphenols (cresol, ethylphenol,

propylphenol, etc.), deoxygenated aromatics (benzene, toluene, xylene, ethylbenzene, propylbenzene, naphthalenes, phenanthrene, etc.), cycloalkanes (cyclohexane, methylcyclohexane, propylcycolohexane, etc.) were used using pyridine as an internal standard to quantify the products obtained from the hydrotreatment. The following equations were used to quantify the Kraft lignin hydrotreatment (paper IV and V).

$$Conversion,\ X\ (\%) = \left(1 - \frac{amount\ of\ unconverted\ lignin}{Initial\ dried\ lignin\ charged}\right) \times 100$$

$$Yield\ (wt\%) = \frac{amount\ of\ product\ (g)\ after\ 5h}{Initial\ dried\ lignin\ charged\ (g)} \times 100$$

$$Selectivity\ (wt\%) = \frac{amount\ of\ product\ (g)\ after\ 5h}{Total\ detected\ products\ (g)} \times 100$$

$$Solid\ residue\ yield\ (wt.\%) = \frac{Dried\ total\ solid\ residue - amount\ of\ catalyst\ charged}{Initial\ dried\ lignin\ charged} \times 100$$

The gas samples obtained from the hydrotreatment were analyzed using a GC (SCION 456, Bruker) with thermal conductivity and FID detectors. Water content in the hexadecane and acetone phase was measured by the volumetric titration method using a Metrohm 870 KF Titrino plus apparatus.

3.5 Catalyst, lignin, and solid residue characterization

3.5.1 N_2 Physisorption

Textural properties (specific surface area, pore size, and pore volume) of the catalysts were measured by a TriStar 3000 gas analyzer. Samples were dried in a flow of dry N_2 before being introduced into the analyzer. Alumina-based catalysts (0.2-0.3g) were degassed at 250 °C for 2 h while zeolite-based catalysts (0.1-0.2 g) were dried at least 6h (preferably overnight) before the measurement. Unsupported catalysts (0.1-0.2) were degassed overnight at 300°C. The Brunauer-Emmett-Teller (BET) method was employed to calculate the specific surface area and Barret-Joyner-Halenda (BJH) method for the pore sizes.

3.5.2 Elemental analysis

Elemental analyzers EA-1110 (CE instruments), and NA2000 (Fisions instrument) were employed to determine the cumulative quantity of C, H, N, and S elements in the recovered catalysts collected after each experiment. During the analysis, the sample was combusted at high temperature and combustion products separated by GC were detected via a thermal conductivity detector (TCD). The measurement was based on the TCD calibration of combustion products. These measurements (paper II and III) were done by Elemental Microanalysis, UK. Metal loading in the fresh and spent catalysts was determined via inductively coupled plasma and sector field mass spectroscopy (ICP-MS) by ALS Scandinavia AB, Luleå, Sweden.

3.5.3 X-ray photoelectron spectroscopy (XPS)

X-ray photoelectron spectroscopy is a surface-sensitive technique used to identify the chemical state of the elements. During the measurement, the sample surface is irradiated with a high-energy focused beam of X-rays (*hv,* eV) during the analysis. As a result, photoelectrons are emitted from the valence bond of the element, the energy ($E_{kin,}$ eV) of which can be analyzed by an energy analyzer considering the work function as well. The difference between the incident and ejected photoelectron energy is thus a measure of binding energy ($E_b = hv-E_{kin}$) and the oxidation state of the elements.

Freshly sulfided and recovered catalysts were analyzed by X-ray Photoelectron Spectroscopy via Perkin Elmer PHI 5000C and Perkin Elmer PHI 5000 VersaProbe III Scanning XPS microprobes. In both cases, irradiation of the sample was performed in an ultra-high vacuum chamber (less than 2×10^{-8} torr) with a monochromatic Al-Kα source having a binding energy of 1486.6 eV. A spherical energy analyzer was used to detect the emitted photoelectrons. High resolution core level spectra of Ni, Mo, C, O, and S were recorded with a step of 0.1 eV or 0.125 eV. MultiPak and CasaXPS were used to analyze/deconvolute the obtained spectra. During the analysis, the C1s binding energy of 284.6 eV (or 284.8 eV) was used as the reference with a Shirley background.

3.5.4 X-ray powder diffraction (XRD)

X-ray diffraction, a non-destructive technique was employed to identify the crystalline structure/planes of synthesized catalysts. The XRD patterns were measured using Siemens, D5000, and Bruker AXSD8 X-ray powder diffractometers with CuKα radiation (λ=1.542A°) operating at 40 kV and 40 mA. Two-theta scanning parameters were recorded from 5 to 80 ° with a scan mode of 0.03° per second.

3.5.5 Raman Spectroscopy

Raman spectroscopy is also a non-destructive light scattering technique that uses high-intensity laser light sources to interact with the materials and give Raman-active molecular vibrations. The energy difference between the incident light and Raman scattered light (inelastic) is used as a measure of Raman shift (wavenumbers) and representative of a specific bond vibration in the materials. Raman spectra were recorded using WITec alpha300 R Confocal Raman microscope having a thermoelectrically cooled EMCCD (Electron Multiplying Charge-Coupled Device) detector, and a 532 nm CW (continuous wave) diode laser to illustrate the characteristic Mo-O and Mo-S vibration for the synthesized catalyst (Paper II and V).

3.5.6 Temperature Program desorption (TPD) and reduction (TPR)

Ammonia and ethylamine TPD measurements (paper II, III, and IV) were performed in a setup consisting of a manifold of mass flow controllers (MFC), a quartz tube with catalyst sample (~25 mg), a temperature-controlled oven (Setaram Sensys differential scanning calorimeter)

and a mass spectrometer (Hiden HPR-20 QUI) to analyze the products in the outlet carrier gas. The total flow rate through the tube was maintained at 20 NmL/min.

During ethylamine TPD, the samples were first degassed (110°C for 1 h and at 250 °C for 3 h) in a flow of Ar. Then the samples were reduced at 600°C by 13% H_2 for 2 h followed by cooling to 100°C. At this temperature, the sample was exposed to 543 ppm of ethylamine for 3 h to complete the adsorption. The sample was then flushed with Ar for 2 h to remove the loosely bound ethylamine. Finally, the temperature was ramped to 600°C at a rate of 5°C/min to desorb the ethylamine. Quantification of the Brønsted acidity is based on the evolved signal of ethylene, C_2H_4 (formed from the decomposition), and measured calibrations for C_2H_4 and ethylamine in the mass spectrometer.

For NH_3-TPD, the sample was degassed at 300 °C for 0.5 h followed by NH_3 adsorption (1000 ppm) at 100 °C for 1.5 h. After that flushing with Ar was continued for 1 h to remove the physically adsorbed NH_3. The sample was then heated to 700 °C with a ramp of 10 °C min^{-1}. The time evolution of the NH_3 desorption peak was used to quantify the total acidity of the catalyst using a standard calibration for NH_3. A similar procedure was used for ethylamine-TPD measurements in paper IV.

TPR was performed for supported and unsupported catalyst (Paper IV) using the same setup as TPD. A small amount of sample (10-20 mg) was degassed at 300 °C for 0.5 h under Ar flow. The temperature of the sample was then cooled to 25 °C. Afterward, 1 vol% of H_2 in Ar has flowed through the sample followed by a temperature increase to 800 °C at a rate of 10 °C/min. The H_2 peak in the MS was followed to compare H_2 uptake profiles.

3.5.7 Scanning and Transmission electron microscopy (SEM and TEM)

TEM analysis was performed to understand the dispersion of the Ni-promoted MoS_2 crystallites on the employed supports. In the first step, samples were loaded onto a carbon coated copper grid. The analysis was conducted with an FEI Titan 80-300 TEM (FEI, Inc.) operating at 300 kV. A high angle annular dark field (HAADF) detector was used to acquire the scanning TEM (STEM) images and an Oxford X-sight detector was used to perform energy dispersive X-ray (EDX) analysis. TEM imaging and analysis (TIA) software was used for the spectrum acquisition and data analysis. ImageJ software was used to measure the Ni-promoted MoS_2 slab length and stacking degree. At least 300 slabs were considered to determine the average slab length and stacking degree shown in the equations below:

$$\text{Average slab length} = \frac{\sum_i^n n_i l_i}{\sum_i^n n_i}, \quad \text{Average stack number} = \frac{\sum_i^n n_i N_i}{\sum_i^n n_i}$$

Where n_i is the number of slabs with length l_i and N_i is the number of layers in slab i. Additionally, considering MoS_2 slabs to have a perfect hexagon shape, the following equation can be used to determine its dispersion, referred to as, f_{Mo}

$$f_{Mo} = \frac{Mo_{edge}}{Mo_{total}} = \frac{\sum_i^m 6(n_i - 1)}{\sum_i^m (3n_i^2 - 3n_i + 1)}$$

where Mo_{edge} is the Mo atoms at the edges of MoS_2 slabs, Mo_{total} denotes the total number of Mo atoms and n_i the Mo atoms in the edge of one MoS_2 slab that can be determined from its length, L=3.2(2n_i-1) Å, and m is the total number of slabs.

Morphology of the catalysts was further evaluated using SEM with a JEOL 7800F Prime instrument. High resolution SEM images were used to measure the dispersion of the particles and their average particle sizes (via ImageJ software) using ~200 particles.

3.5.8 Lignin and solid residue characterization

Fourier transform infrared spectroscopy (FTIR) was performed using a Bruker Vertex 70v spectrometer on Kraft lignin and the lignin derived solid residue was obtained after the hydrotreatment. The instrument was operated at room temperature in the frequency range of 400-4000 cm^{-1} having 4 cm^{-1} resolution with 64 scans. The background was subtracted to eliminate the air contribution. In addition, solid-state cross-polarization (CP) 13C NMR was performed on them employing a setup having a 4 mm MAS BB/1H probe and a Bruker Advance III 500 MHz spectrometer. During a typical run, the rotor spinning was set to 10 kHz and the CP time to 1.5 ms. Furthermore, thermogravimetric analysis (TGA) was performed on Kraft lignin and solid residues containing catalyst using a Mettler Toledo TGA/DSC 3+ instrument. The sample was heated to 800 °C at a rate of 10°C min^{-1} in the presence of air and argon respectively.

4 Results and Discussion

This chapter summarizes the work based on the papers appended (I, II, III, IV, and V) in this thesis work. Each of these studies involved Mo-based transition metal sulfided catalysts.

In Paper I, a comprehensive literature review has been addressed for the sulfided catalysts in upgrading renewable feedstocks which will not be discussed further here. Primarily, the activity of transition metal sulfided catalysts (both in supported and unsupported form), their roles, and reaction mechanisms were explained in detail while upgrading renewable feedstocks based on triglycerides, pyrolysis oil, and lignin. In addition, reaction kinetics and catalysts deactivation aspects are included. Furthermore, the major challenges and potential areas to focus on for future studies are addressed. In Paper II, typical lignin linkages present in native/technical lignin (etheric, α-O-4, β-O-4, and carbon-carbon, 5-5') have been explored using sulfided NiMo over supports with varying acidities. γ-Al_2O_3 and ultrastable-Y zeolites (USY or Y used synonymously) were used as the support materials. It has been observed that NiMoS over the USY shows high hydrogenolysis activity for both etheric C-O-C and C-C bonds present in the model dimers and evolved intermediates that result in high yields of monoaromatics including BTX, alkylphenols, and cycloalkanes. These results further led us to investigate the effect of the silica/alumina ratio of USY zeolites as supports for NiMoS in the hydrotreatment of lignin dimers (Paper III). The catalytic activity and characterization results revealed that a moderate silica/alumina ratio of 30 showed a high degree of hydrogenolysis, hydrocracking and HDO reactions owing to the balanced acidic and deoxygenation sites. In Paper IV, NiMoS with a silica/alumina ratio of 30 has been exploited for one-pot hydrotreatment of Kraft lignin in a batch reactor. In addition, dealuminated and desilicated zeolites were included in this study. To gain further insights, unsupported NiMoS (UNiMoS) without zeolite was investigated to elucidate the role of zeolites and metal sulfides in valorizing lignin. In Paper V, lignin and lignin derived bio-oil model compound was studied further with a highly active MoS_2 synthesized via a simple hydrothermal method followed by a thermal annealing treatment.

The results from these papers demonstrate that physicochemical properties of the transition metal sulfides can be tailored using various supports or varying the synthesis method without support to obtain catalysts that are highly active for hydrogenolysis, hydrocracking, and deoxygenation reactions and yield biofuel (rich in cycloalkanes and alkylbenzenes) from lignin

and lignin derived bio-oil. The following sections discuss the result in detail from each appended paper excluding Paper I.

4.1 The role of support acidity on hydrotreating lignin dimers

4.1.1 HDO of benzyl phenyl ether (α-O-4 linkage)

Fig.8 and **Scheme 1** show the conversion of BPE and the evolution of the intermediates and products respectively. Hydrogenolysis, hydrolysis of the $C_{aliphatic}$-O bond, and transalkylation (transfer of benzyl group to ortho, para position) primarily lead to the cleavage of BPE to toluene, phenol, and benzyl phenols [82]. However, the possible hydrolysis product benzyl alcohol (see **Scheme 1**)) was not detected indicating either its rapid disappearance or that it is an unfavorable route at the employed conditions. With Y-based catalysts, the rapid cleavage of the aliphatic ether bond leads to faster conversion of BPE. This is likely due to enhanced rates of transalkylation over NiMoY (NiMo over USY)/NiMoAY (NiMo over equal amounts of γ-alumina and USY-zeolite) than NiMoA (NiMo over γ-Al_2O_3) based on their differences in acidities [45].

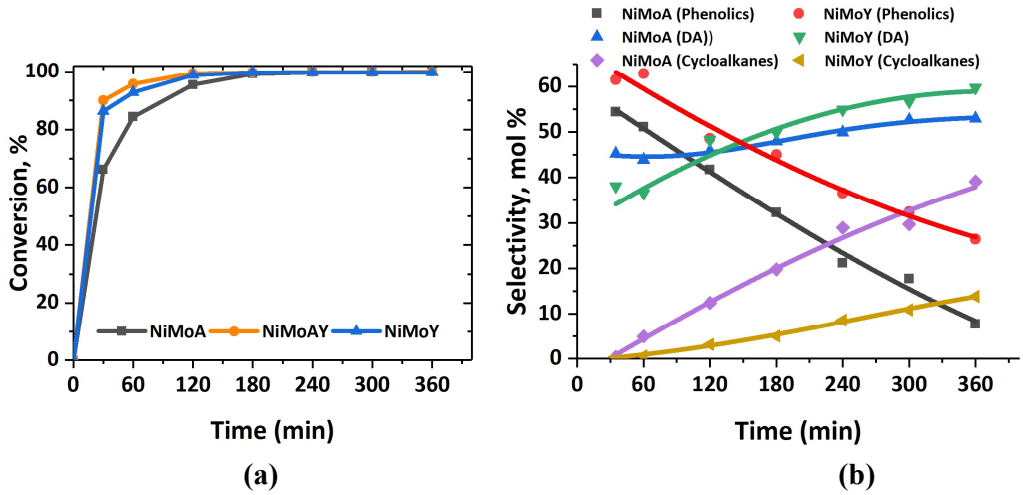

Fig.8 (a) BPE Conversion and (b) product selectivity during HDO of BPE in the autoclave at 593 K, 5 MPa, and 1000 rpm, DA=deoxygenated aromatics.

Scheme 1 Proposed reaction pathways for HDO of BPE.

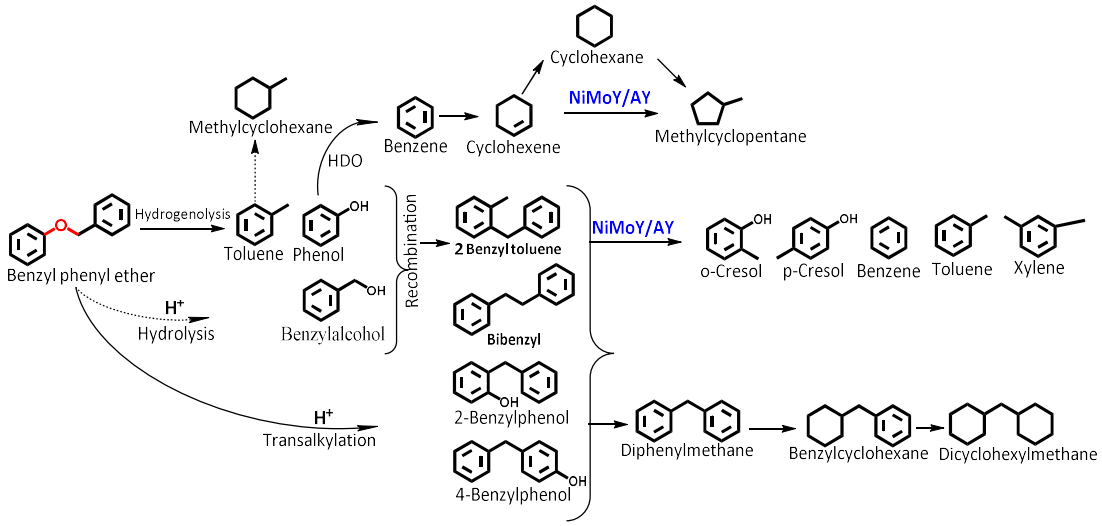

To follow the reaction profiles, products/ intermediates are grouped into phenolics (having OH groups on a benzene ring), deoxygenated aromatics (DA), and cycloalkanes (fully saturated benzene ring) for simplicity. **Table 1** presents the selectivity of major compounds in each of these groups.

As shown in **Scheme 1** phenol undergoes HDO to form benzene, cyclohexane, and methylcyclopentane. Methylcyclopentane is formed due to higher isomerization activity over NiMoY/AY [121]. On the other hand, methylene/ethylene linked (C-C linked) benzyl phenols undergo HDO over NiMoA to form deoxygenated dimers with partial or full hydrogenation of the benzene rings while over NiMoY/AY hydrocracking leads to form monoaromatics including BTX (benzene toluene and xylene). Benzene and toluene are the dominant DA over NiMoY while for NiMoA they are toluene and deoxygenated dimers. It is evident from **Fig.8** (b) that DA is higher for NiMoY than NiMoA after 360 min which is due to high benzene selectivity. However, slower HDO over NiMoY/AY shows higher phenolics (monoaromatics) at the end of 360 min of reaction. Also, lower cycloalkanes over Y-based catalysts indicate slower hydrogenation activity. These led to an overall aromatics selectivity of 85% (monoaromatics) over NiMoY compared to ~60% (monoaromatics and dimers) over NiMoA.

Table 1 Product selectivities from HDO of BPE after 6 h reaction at 50 bar and 320 °C.

Catalyst	X_{BPE}* (%)	Carbon balance (%)	Selectivity (%)									
			Cycloalkanes			Deoxygenated aromatics (DA)				Phenolics		
			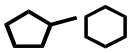		Others	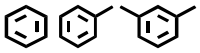			Dimers		Cresols	Dimers
NiMoA	>99	94	<1	38	1	-	43	-	9	7	-	2
NiMoAY	>99	92	2.7	28	3.5	-	44	0.5	5	13	2	0.7
NiMoY	>99	87	9.3	<1	4.5	35	22	2	-	18	8	0.4

*X_{BPE} refers to BPE conversion.

4.1.2 HDO of PPE (β-O-4 linkage)

Fig.9 presents conversion and reaction profiles during HDO of PPE. Scission of the sp^3 C-O bond in β-O-4 linkages, via three possible pathways (shown in **Scheme 2**), was found to be favored in the order NiMoAY>NiMoA>NiMoY (**Fig.9a**). These pathways produce phenol, ethylbenzene, and phenethylphenols. Like BPE, transalkylation of the phenethyl group in PPE was found to be preferred in the order NiMoY>NiMoAY>NiMoA. As a result, initially high amounts of phenolic dimers, mainly phenethylphenols were formed over NiMoY as shown in **Fig.9b**. These dimers now contain stable, recalcitrant β-1 linkages (C-C linkage) as is more common in technical rather than native lignin [122]. However, as the reaction progresses, these dimers become cleaved over NiMoY to yield ethylphenol isomers while over NiMoA they become deoxygenated. Based on the products and intermediates evolution a reaction pathway in **Scheme 2** is presented. It has been observed that over sulfided NiMoY, the enhanced transalkylation step reduces the amount of alkylbenzene (ethylbenzene) but increases the benzene formation due to cracking of the transalkylation product (**Table 2**). This phenomenon

yields similar overall DA selectivity for NiMoA and NiMoY at the end of 360 min of reaction. Like for BPE, overall monoaromatics selectivity remains higher (81% vs 49%) over NiMoY compared to NiMoA.

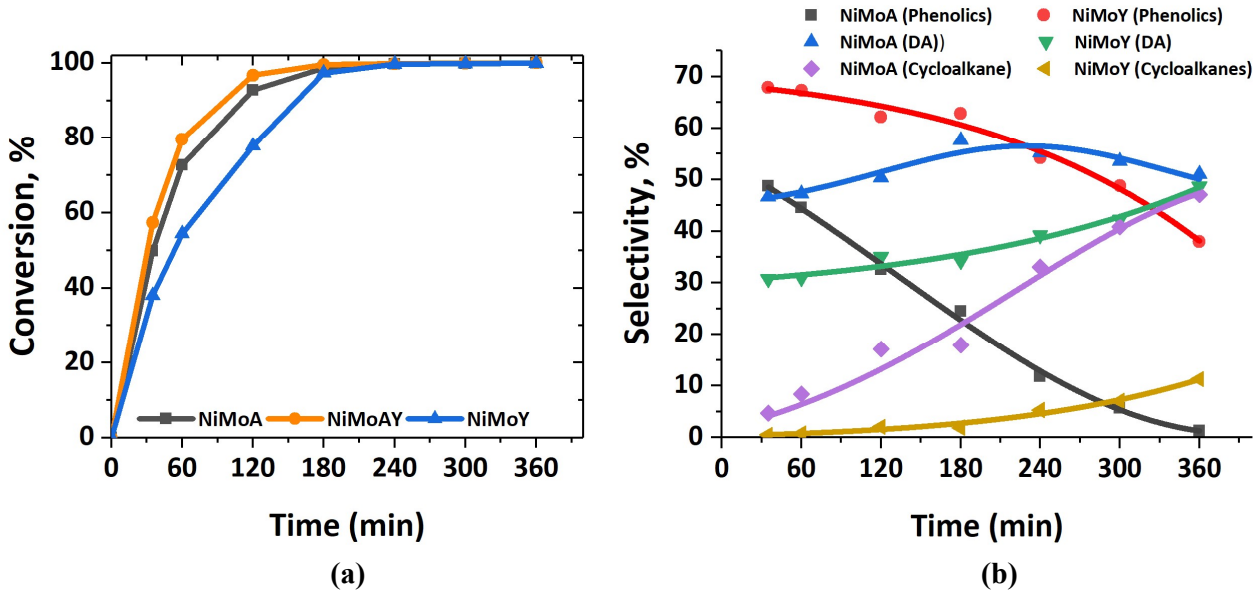

Fig.9 (a) PPE conversion and (b) product selectivity during HDO of PPE in the autoclave at 593 K, 5 MPa, and 1000 rpm. DA=deoxygenated aromatics.

Scheme 2 Proposed reaction pathways for HDO of PPE.

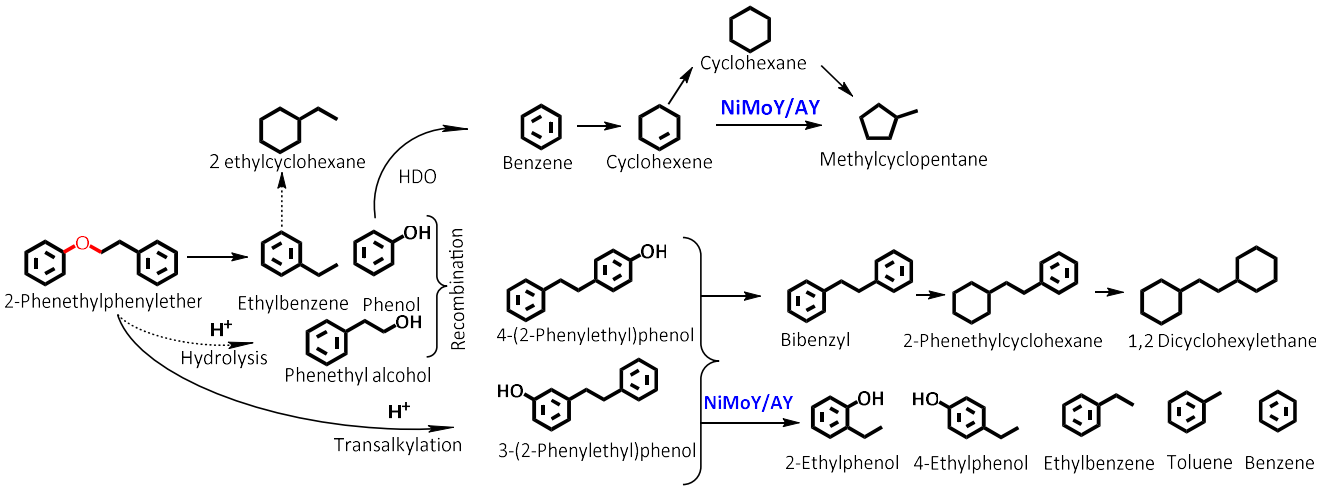

Table 2 Product selectivities from HDO of PPE after 6 h reaction at 50 bar and 320 °C.

Catalyst	X_{PPE}* (%)	Carbon balance (%)	Selectivity (%)									
			Cycloalkanes			Deoxygenated aromatics (DA)				Phenolics		
			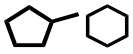		Others	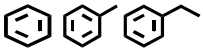		Dimers		Ethyl-phenols	Dimers
NiMoA	>99	95	-	45	3	-	-	48	3	1	-	1
NiMoAY	>99	93	17	16	3	-	-	48	3	12.5		3
NiMoY	>99	84	10	-	1.5	14	1	32.5	2	31	4	4

*X_{PPE} refers to PPE conversion.

4.1.3 HDO of 2,2'Biphenol

Fig.10 shows the product selectivities during HDO of 2,2' biphenol over sulfided NiMo catalysts. It is important to note that for NiMoA, the mass balance was poor for the samples taken before 180 min of reaction. This might be due to residual reactant remaining in the sampling line or low solubility of the reactant in dodecane at room temperature. For later samples, the mass balance was found >90%. **Scheme 3** shows possible reaction pathways with products/intermediates. **Fig.10** illustrates that acid catalyzed dehydration dominates and yields a higher fraction of dibenzofuran (DBF) primarily via intramolecular nucleophilic attack of the hydroxyl groups in 2,2' biphenol [64]. For NiMoA this reaction competes with direct HDO to form o-phenylphenol (OPP). However, further DBF/OPP hydrogenation and C-O cleavage of tetrahydro-dibenzofuran (THDBF) produce 2-cyclohexylphenol (CHPOH). A small amount of biphenyl (BP) has been observed indicating DDO of OPP. Further hydrogenation of BP can yield cyclohexylbenzene (CHB). However, CHPOH a dominant intermediate undergoes HDO, hydrocracking, and HYD routes to yield CHB, cyclohexane, phenol, and several C-C dimers (36%) including bicyclohexane (BCH) and cyclopentyl-cyclohexylmethane (CPMCH) as the final products (**Table 3**). This observation is consistent with previous studies of dibenzofuran HDO over sulfided NiMoA [123]. Analogous products have been reported for DBF HDO over Pt-based acid-base catalysts [124-127].

As shown in **Fig.10**, for NiMoY conversion of 2,2' Biphenol to DBF is very fast and favored over DDO. However, further conversion of DBF seems low and relatively faster over NiMoY than NiMoAY. As the C-O bond in DBF is cleaved, intermediates formed undergo acid induced rapid cracking to yield phenol and cyclohexane. Isomerization of cyclohexane produces methylcyclopentane as the final product. Interestingly, no other C-C dimers were detected.

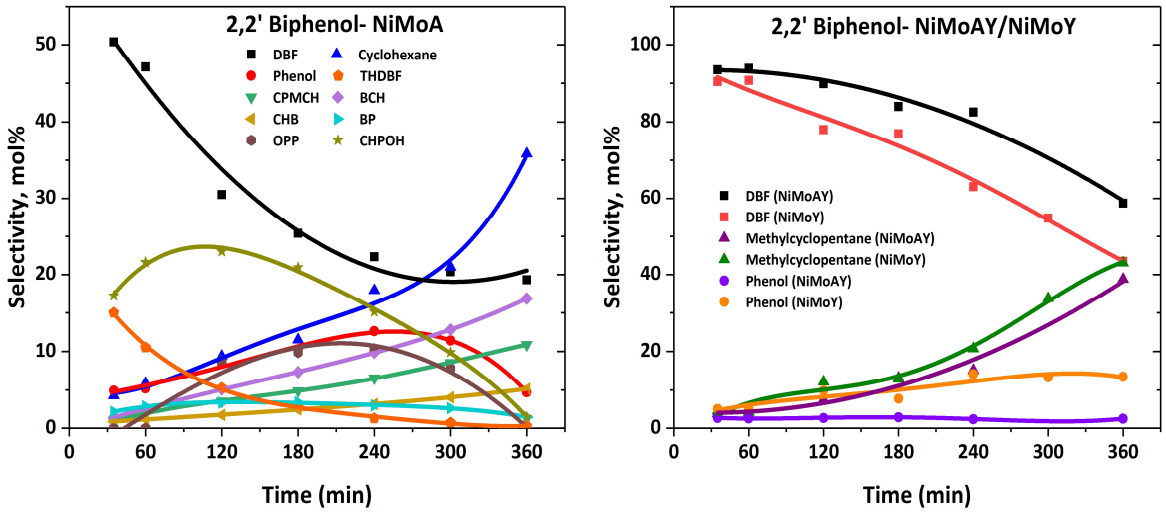

Fig.10 Product selectivities during HDO of 2,2' Biphenol over NiMoA, NiMoAY, and NiMoY.

Scheme 3 Proposed reaction pathways during HDO of 2,2' biphenol.

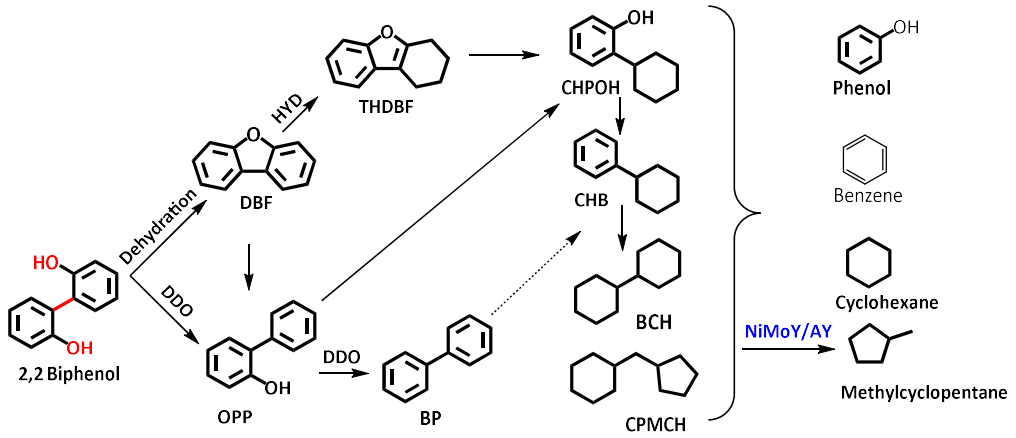

Table 3 Product selectivities from HDO of 2,2' biphenol after 6 h of reaction at 5 MPa and 593 K.

Catalyst	$X_{5\text{-}5'}$* (%)	C-balance (%)	Selectivity (%)				
			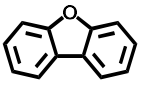	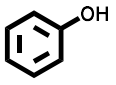			Dimers
NiMoA	91	95	23	4	36	<1	36
NiMoAY	>99	94	59	2	-	39	-
NiMoY	>99	96	44	13	-	43	-

*$X_{5\text{-}5'}$ refers to 2,2' biphenol conversion.

4.1.4 Catalyst Characterization

Metal loadings on the synthesized and spent catalyst verified by ICP-MS are shown in **Table 4**. Leaching of Ni and Mo after the activity test can be ruled out as the Ni/(Ni+Mo) ratio was found to be consistent.

Table 4 ICP data-metal contents on synthesized and spent catalysts.

Catalyst	As-synthesized				After BPE test		After PPE test		After 5–5' test	
	Mo (wt.%)	Ni (wt.%)	Si/Al	Ni/ (Ni+Mo)	Si/Al	Ni/ (Ni+Mo)	Si/Al	Ni/ (Ni+Mo)	Si/Al	Ni/ (Ni+Mo)
Y	-	-	15.0*	-	-	-	-	-	-	-
NiMoA	13.3	4.6	--	0.26	--	0.28	--	0.26	--	0.24
NiMoAY	12.3	4.4	0.6	0.27	0.71	0.27	0.65	0.27	0.62	0.26
NiMoY	13.2	4.8	16.5	0.27	13.5	0.27	13.3	0.28	16.4	0.28

*From Zeolyst international

Ethylamine TPD results are shown in **Fig.11** and **Table 5**. Adsorption of ethylamine on a Brønsted acid site forms an ethylammonium ion. The Hoffman elimination reaction of this complex during desorption produces ethylene and NH_3. The ethylene concentration was followed to measure the Brønsted acidity of the catalyst and desorbed ethylamine to quantify the Lewis acidity of the catalyst [128]. **Fig.11** shows a strong desorption peak of ethylene at about 502 °C for NiMoY/NiMoAY while for NiMoA it is observed at about 430 °C. This discrepancy can be due to the strength of the Brønsted acidity present in them or due to diffusion limitations [129]**.** As shown in **Table 5** Brønsted acidity was found to increase with an increasing fraction of Y zeolite. Also, differences in Lewis acidity among the three catalysts are smaller and contribute to 5-10% of the total acidity of the catalysts.

Table 5. The acidity of the synthesized catalysts.

Catalyst	Brønsted acidity ($\mu mol\ g^{-1}$)	Lewis acidity ($\mu mol\ g^{-1}$)
NiMoY	401	22
NiMoAY	370	25
NiMoA	258	30

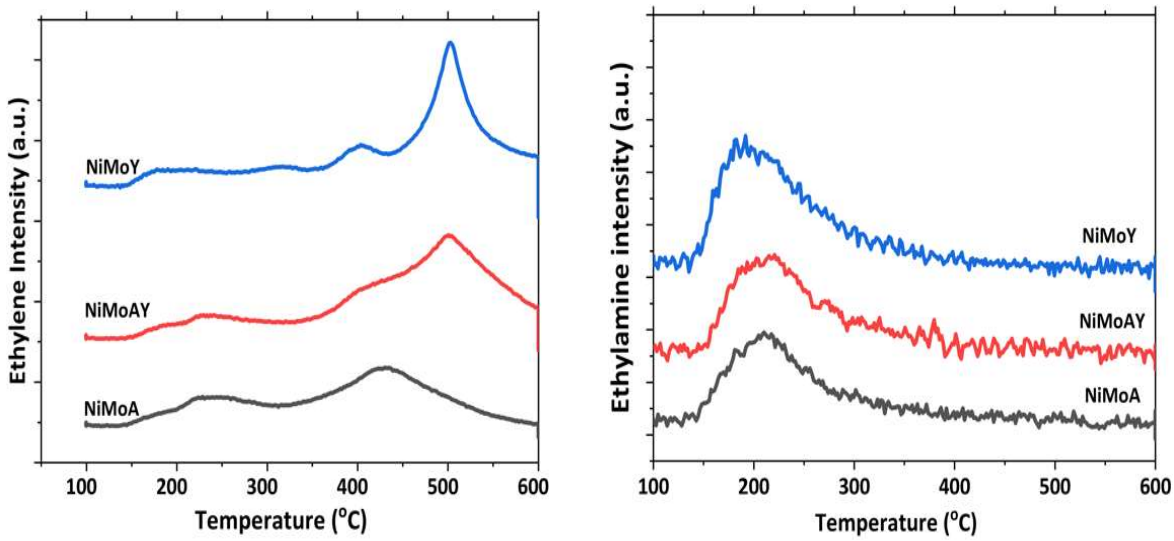

Fig.11 The relative intensity of ethylene and ethylamine during desorption of ethylamine-TPD.

The XRD patterns in **Fig.12** show well dispersed Ni and Mo over the catalysts since no distinct diffraction peak of NiO or MoO_3 crystallites were observed. Nevertheless, peak shifting (inset in the right corner) to lower diffraction angles for NiMoY indicate compressive strain development due to pore blockage or a change in the composition in the structure [130]. In addition, the lower intensity of the impregnated catalyst represents a lower crystallinity of the zeolite framework [131].

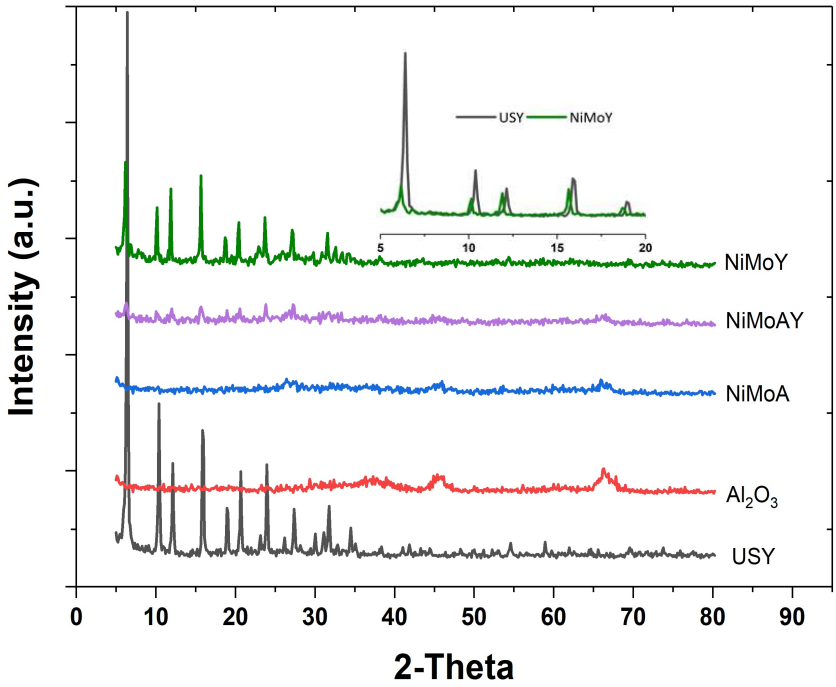

Fig.12 XRD pattern of synthesized catalysts, parent USY, and γ-Al_2O_3.

N_2 physisorption data in **Table 6** shows the pore blocking after impregnation of the metal Ni and Mo. Average pore sizes (pore volume and pore diameter) and surface area of the recovered catalysts reduced to a significant degree indicating extraneous deposition on the catalytic surfaces. For example, a 30-45 % reduction in the surface areas was observed for the recovered NiMoY/NiMoAY tested with lignin dimers whereas it is only around 8-20% for recovered NiMoA.

Table 6 N_2 Physisorption data for fresh and spent catalysts.

Catalyst	As synthesized			After BPE test			After PPE test			After 5–5' test		
	S_a	v_p	d_p	S_a	v_p	d_p	S_a	v_p	d_p	S_a	v_p	d_p
γ-Al_2O_3	199	0.48	97.6									
USY	763	0.25	63.3									
NiMoA	139	0.31	87.6	111	0.18	84.9	119	0.20	79.1	128	0.26	78
NiMoAY	270	0.26	71.9	163	0.18	43.8	148	0.19	51.8	175	0.23	51,9
NiMoY	412	0.20	53.1	291	0.20	27.6	246	0.20	31.9	-	-	-

S_a =BET surface area (m^2/g), V_p = Pore volume (cm^3/g), d_p = Average pore sizes for mesopores (Å)

Elemental analysis (**Table 7**) revealed higher carbon deposition on NiMoY and NiMoAY surfaces compared to NiMoA. This contributes to the catalyst deactivation by reducing the number of active sites. This can be due to the higher concentration of Brønsted acidic sites over NiMoY/AY which leads to undesirable reactions (e.g., condensation, polymerization, etc.) of adsorbed coke precursors (e.g., phenolics/aromatics) formed during the reaction. C contents are slightly higher for PPE-treated NiMoY/AY. This might be due to higher diffusion resistance of larger PPE than other model compounds leading to the formation of a large surface phenolics pool resulting in coking reactions. Changes in H content for all catalysts are negligible while for S there is a minor decrease in the recovered catalysts.

Table 7 Elemental contents of carbon, hydrogen, and sulfur on the freshly sulfided and spent catalysts.

Catalyst	Freshly Sulfided			After BPE test			After PPE test			After 5–5' test		
	C	H	S	C*	H	S	C*	H	S	C*	H	S
NiMoA	0.4	1.3	8.8	0.98	0.8	7.7	2.1	0.7	8.2	2.7	0.5	8.3
NiMoAY	--	--	8.3	2.1	1.5	6.2	4.0	0.6	7.8	3.7	0.4	7.0
NiMoY	1,0	0.9	9.8	6.5	1.6	7.1	7.9	0.5	8.9	6.7	0.5	7.0

*C values for catalysts after reactions tests are in (g carbon)/(g catalyst)/(mol of feed converted to deoxygenated products). All other values are in wt. % including C in sulfide catalyst.

Raman spectra for the synthesized catalysts are shown in **Fig.13**. The characteristic peak appearing at 953 cm^{-1} indicates the symmetric stretching vibration of Mo=O in octahedrally coordinated Mo oxide species that are reported to interact weakly with the support and enhance reducibility and activity of the catalyst [132]. Other characteristic peaks at 995 cm^{-1}, 900 $cm^{-1,}$ and 825 cm^{-1} signify the presence of bulk MoO_3 phases, less active or inactive

tetrahedrally coordinated Mo oxide species, and Mo-O-Mo vibration (presence of polymerized Mo oxides). It is apparent from **Fig.13** that more active Mo oxide species shall be accessible for the case of NiMoY/AY due to the less bulk MoO_3.

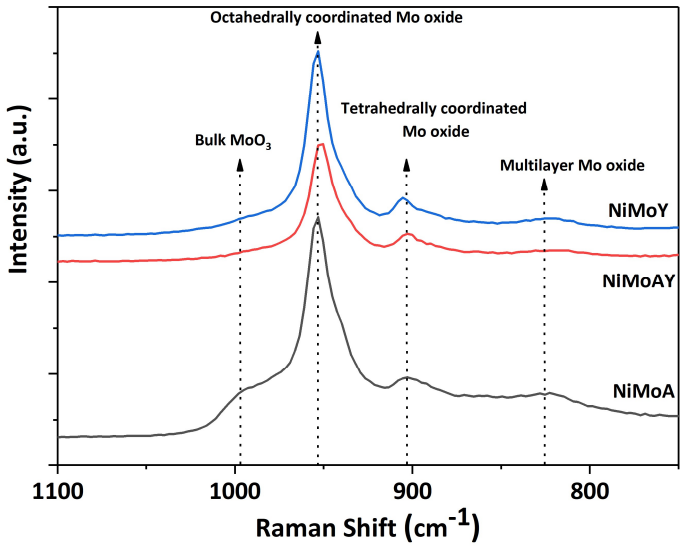

Fig.13 Raman spectra of the synthesized catalyst.

Ni2p and Mo3d core level XPS spectra are shown in **Fig.14**. Deconvolution based on C1s revealed Mo 3d fitting values are Mo^{+4} : 228.7±0.1 eV for Mo $3d_{5/2}$ and 231.9±0.1 eV for $Mo3d_{1/2}$ and Mo^{+6} : 232.2±0.1 eV for Mo $3d_{5/2}$ and 235.4±0.1 eV for $Mo3d_{1/2}$. Similarly, Ni2p values of 852.8±0.1, 854.3±0.1, and 856±0.2 eV portray the presence of NiSx, NiMoS, and Ni^{+2} species. The relative contribution of phases in **Table 8** (for NiMoY and NiMoA) shows that Mo sulfidation seems similar on both catalysts but for NiMoY, MoS_2 slabs are surrounded by more Ni atoms representing the active NiMoS phase to a slightly better extent [133].

Table 8. XPS and TEM characterization of the metal sulfides.

Catalyst	Mo Sulfidation (%)	Ni Sulfidation (%)			Slab length (nm)	Stacking	f_{Mo}
	Mo^{4+}	NiS_x	NiMoS	Ni^{2+}			
NiMoA	84	16	54	30	4.7	3.8	0.22
NiMoY	82	8	61	31	4.1	4.2	0.27

The morphologies of the Ni-promoted MoS_2 play a key role in defining activity and selectivity. Based on 300 MoS_2 crystallites, analysis of several HRTEM images (one shown in **Fig.15**) reveals slightly shorter slab length and higher stacking (**Table 8**) of MoS_2 slabs. This difference increases the dispersion (f_{Mo}) of the NiMoS phase over NiMoY which implies more edge and corner sites of Mo atoms would be accessible for the incoming reactants/ intermediates.

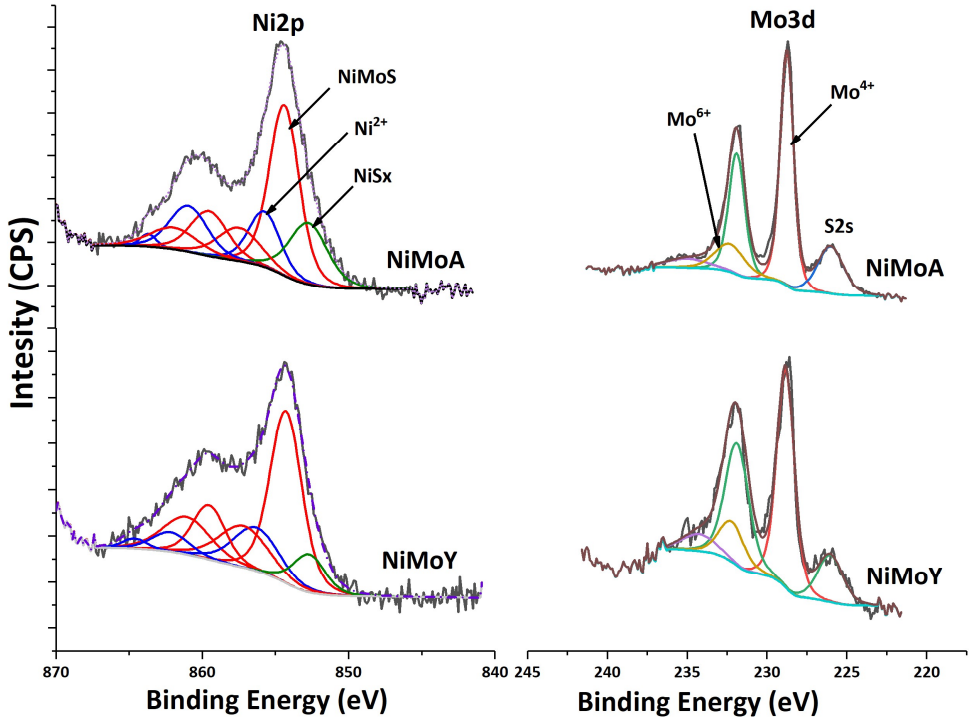

Fig.14 Core level XPS spectra of Ni2p and Mo3d for NiMoA and NiMoY.

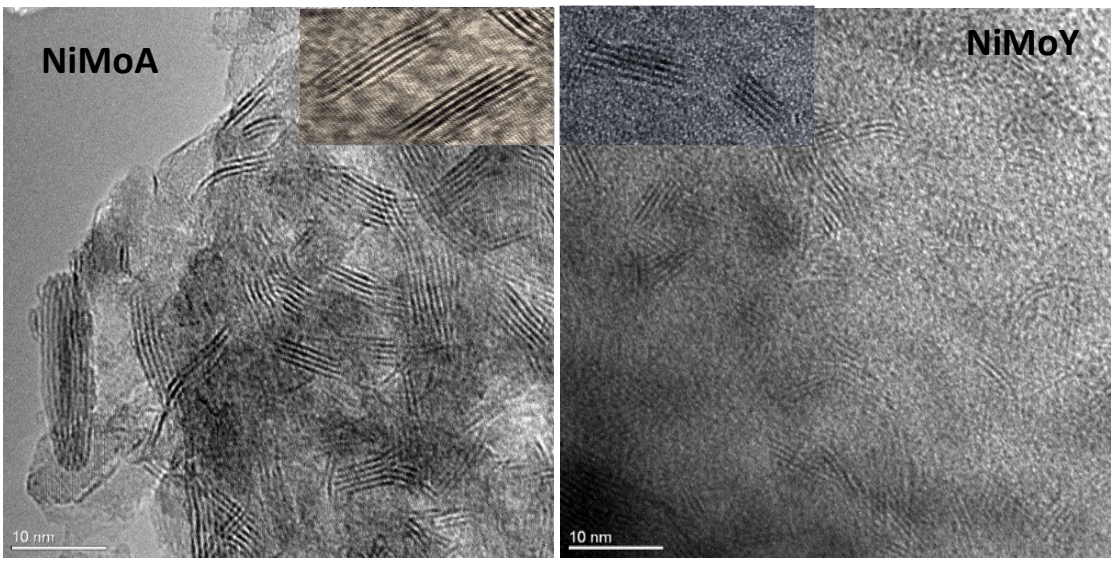

Fig.15 Characteristic HRTEM images of NiMoA and NiMoY: insets showing the differences in slab distribution

4.1.5 Catalytic properties related to the activity

The catalyst characterization results via TEM, Raman, and XPS discussed above suggest enhanced dispersion and a more active NiMoS phase over NiMoY. Together with a higher concentration of Brønsted acidity, NiMoY showed improved scission of the aliphatic C-O

linkage in BPE. With moderate Brønsted acidity, NiMoAY showed faster hydrogenolysis of C-O in both BPE and PPE (**Fig.8(a) and Fig.9(a)**). This is mainly due to the dominant acid catalyzed transalkylation reaction in BPE and PPE leading to the formation of recalcitrant methylene/ethylene (i.e., C-C) linked phenolic dimers (**Fig.8 (c) and Fig.9(c)**). The acid catalyzed dehydration is also dominant over NiMoY/AY for 2,2'-biphenol to DBF. However, the proximity of the active phase and Bronsted acidity over NiMoY was found to be able to break the intermediate C-C dimers effectively. BPE, PPE, and 2,2'-biphenol derived C-C dimers undergo substantial cracking over NiMoY mainly to yield monoaromatics. In addition, methyl cyclopentane was preferred over NiMoY for all the feeds which implies its higher isomerization activity. Furthermore, low hydrogenation/deoxygenation activity over Y based supports yields more phenolics at the end of the 6 h reaction period which could arise due to 1) stronger adsorption of oxygenates and phenolics on the zeolite surface creating a surface pool of these species, (2) inaccessibility of acidic sites in smaller micropores, (3) the longer diffusion distance between the metallic and acidic sites, i.e. poorer proximity of the active sites especially for the micropores of the zeolite, (4) different morphologies of metal sulfides inside the zeolite micropores [92, 134].

Fig.16 shows the comparison of intermediate dimers formed and consumed via transalkylation/HDO/hydrogenation/hydrocracking for BPE and PPE feed over NiMoA/NiMoY surfaces.

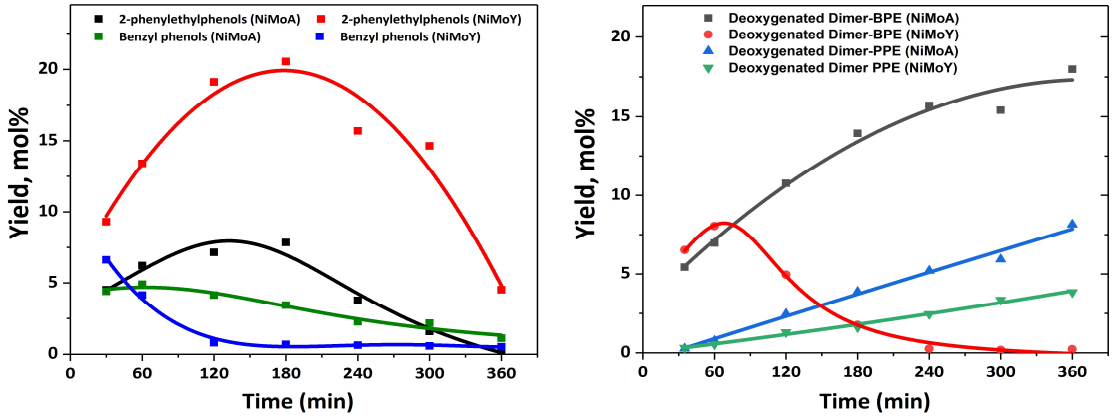

(a) **(b)**

Fig.16 (a) The yield of the intermediate phenolic dimers, benzyl phenols, from BPE and 2-phenylehtylphenols from PPE (b) deoxygenated dimers from BPE and PPE

The formation of BPE-derived benzyl phenols and PPE-derived 2-phenylethylphenol dimers over NiMoY displays the plausible diffusion limitation mostly for the latter compound. Benzyl phenols are initially higher and are cracked/deoxygenated rapidly whereas 2-phenylethylphenol gives a maximum yield after 3 h (NiMoY) of reaction before being cracked/ deoxygenated. Low conversion of such intermediate phenolics can impose pore mouth

blockage and the build-up of a surface phenolics pool favoring undesirable side reactions for coking. It is evident from **Fig.16(b)** that deoxygenated dimers increase rapidly for both BPE and PPE over NiMoA while for NiMoY there is a remarkable difference. For BPE dimers cracking starts rapidly after 60 min of reaction time while for PPE it continues to increase but at a lower rate than NiMoA implying hydrocracking. This again infers the influence of diffusion limitations.

It is clear from the above discussion that NiMoY can efficiently cleave both C-O and recombined C-C linkages during HDO of lignin dimers (BPE and PPE) whereas for NiMoA the yield of C-C dimers increases with time. In addition, the cleavage of recalcitrant 5,5' linkages show the potential of NiMoY for the upgrading of technical lignin (e.g., Kraft lignin). Indeed, a tradeoff between the Brønsted acid sites (BAS), deoxygenation sites, and pore accessibility are inevitably needed to augment catalytic performance.

4.2 Effect of silica/alumina ratio on the hydrotreatment of lignin dimers over NiMoS-USY

In this study, NiMo sulfide over a series of ultra-stable Y zeolite (USY) with varying silica/alumina (SAR) ratios (12, 30, and 80) has been investigated further to elucidate their role on lignin dimer hydrotreatment. 2-phenylethyl phenyl ether (PPE), 4,4' dihydroxy diphenylmethane (DHDPM), and 2-phenyl phenol (2PP) has been used as the model lignin dimers. The resulting catalysts are acronym as NiMoY12, NiMoY30, and NiMoY80 where YXX represents the corresponding SAR of USY.

4.2.1 HDO of 2-phenylethyl phenyl ether (PPE)

As can be seen in **Fig.17 (a),** PPE conversion reaches ~100% for NiMoY30 in 120 min while for NiMo on the other Y zeolites it takes 180 min. Without the sulfided NiMo catalyst, Y30 gives only 85% of PPE conversion after 360 min of hydrotreatment yielding ~51% of the phenolic dimer (not shown). In all cases, hydrogenolysis of PPE primarily yields phenol, ethylbenzene, and phenolic dimers (see **Scheme 1**) [45, 135]. Based on the initial rate of reaction measured in **Table 9**, it is evident that the rate of transalkylation dominates over Y30 while for NiMo based catalysts direct C-O cleavage to phenol and ethylbenzene prevails. The turnover frequency based on the total acidic sites at 35 minutes for NiMo impregnated catalysts reaches a value, five times higher than Y30. Increasing the overall acidity of the catalyst with decreasing silica/alumina ratio was found to increase the initial rate of direct C-O cleavage. The initial transalkylation rate is higher for NiMoY12/NiMoY30 than NiMoY80 giving rise to a higher initial phenolic dimer yield as can be seen in **Fig.17(b).**

Fig.17 (b) shows the yield of phenolic dimers decreases as the reaction progresses. This is due to the cleavage of β-1, C-C linkages between the phenolic dimers leading to the formation of alkylphenols. The cleavage is higher for NiMoY30. Alkylphenols thus formed via C-O hydrogenolysis and C-C hydrocracking undergoes hydrodeoxygenation/hydrogenation reactions to yield deoxygenated aromatics and cycloalkanes. It is worth mentioning that some phenolic dimers can undergo HDO reactions to yield bibenzyl (<5%).

From **Fig.17,** it is clear that benzene (B), toluene (T) and ethylbenzene (EB), and cycloalkane yields increase faster over NiMoY30 especially when PPE is fully converted. This is mainly due to higher C-O and C-C cleavage owing to its moderate acidity, better pore accessibility of the reactants/intermediates, and a higher dispersion of Ni-promoted MoS_2 slabs (described in section 4.2.4). It is also evident that the highly acidic catalyst with the highest Brønsted acidic site (BAS) density, NiMoY12 influences only the initial rate of reactions. Slower hydrocracking of phenolic dimers and lower deoxygenation over NiMo12 can be attributed to diffusion limitations (due to smaller pore sizes) and relatively lower dispersion of the active phases. On the other hand, NiMoY80 being the least acidic catalyst shows even lower hydrocracking ability for PPE-derived dimers but yields HDO products analogous to NiMoY12 which demonstrates the importance of pore accessibility and external surface area to access the deoxygenation sites. Based on these results, it is apparent that a suitable balance between

acidic sites and deoxygenation sites and their accessibility is crucial to harmonize the cleavage of etheric and C-C bonds in PPE and PPE derived dimers.

Table 9 Initial rate of reaction, TOF, and transalkylation rate measured at 35 minutes for 2-phenethyl phenyl ether (PPE).

Catalyst	Initial rate of ($C_{\beta\text{-}O\text{-}4}$) cleavage in PPE, mmol g^{-1} h^{-1}	TOF35 (h^{-1})	Initial rate of trans-alkylation, mmol g^{-1} h^{-1}
Y30	8.4	20	15
NiMoY12	78	114	24
NiMoY30	61	106	26
NiMoY80	50	104	14

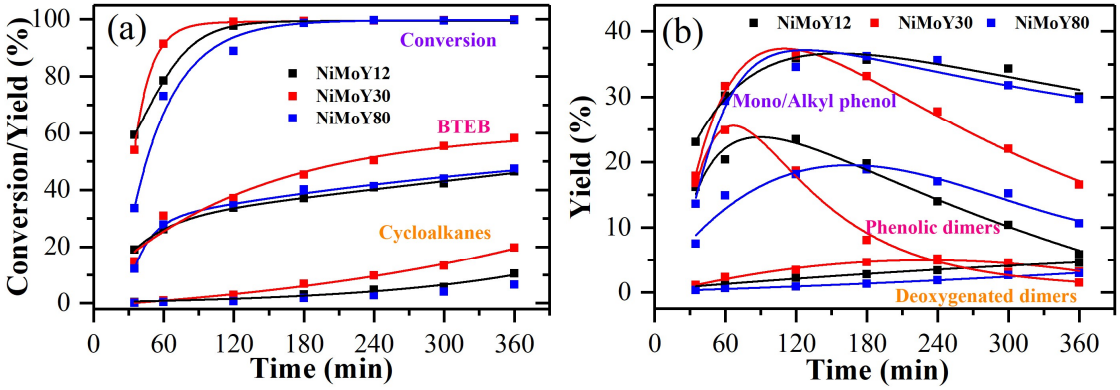

Fig.17 Effect of SAR on the cleavage of PPE over NiMoS-USY zeolites. The time- profile of PPE conversion and yields of product groups at 345 °C, 50 bar, and 1000 rpm are shown.

4.2.2 HDO of 4,4 Dihydroxy diphenylmethane (DHDPM)

To further understand the effect of SAR, a methylene-linked phenolic dimer, 4,4-dihydroxy diphenylmethane (DHDPM) has been investigated using the high SAR catalysts, NiMoY30 and NiMoY80. The results are shown in **Fig.18** with a simplified reaction **Scheme 4** based on the evolution of products and intermediates. It is evident from the GC-MS spectra (**Fig.19**) that the cleavage of Csp_3-C_{sp2} bonds in DHDPM was completed in about 35 minutes over NiMoY30. The primary cleavage products consist of phenols and cresols with a very high yield (>90%) as can be seen in **Fig.18**. Suai et al. [78] observed similar products while investigating cleavage of -CH_2- linked C-C model dimers over CoS_2. A small variation in the initial conversion over NiMoY30 and NiMoY80 signifies that differences in their acid site densities and strengths have little influence on the cleavage of DHDPM however, discrepancies in the final HDO products prevail. Mono/alkylphenol undergoes deoxygenation/hydrogenation reactions to yield a mixture of cycloalkanes and BTX. The higher yield of monocyclics is due to early cleavage of DHDPM and prolonged reaction time for the intermediates to facilitate the hydrogenation of the deoxygenated aromatics under the reaction conditions.

Scheme 4 A proposed reaction scheme during HDO of DHDPM over NiMoS-USY zeolites.

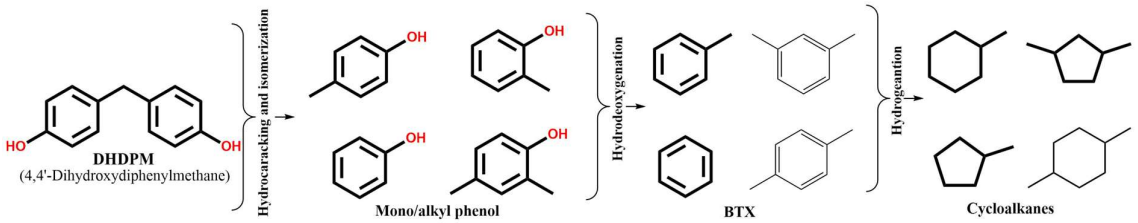

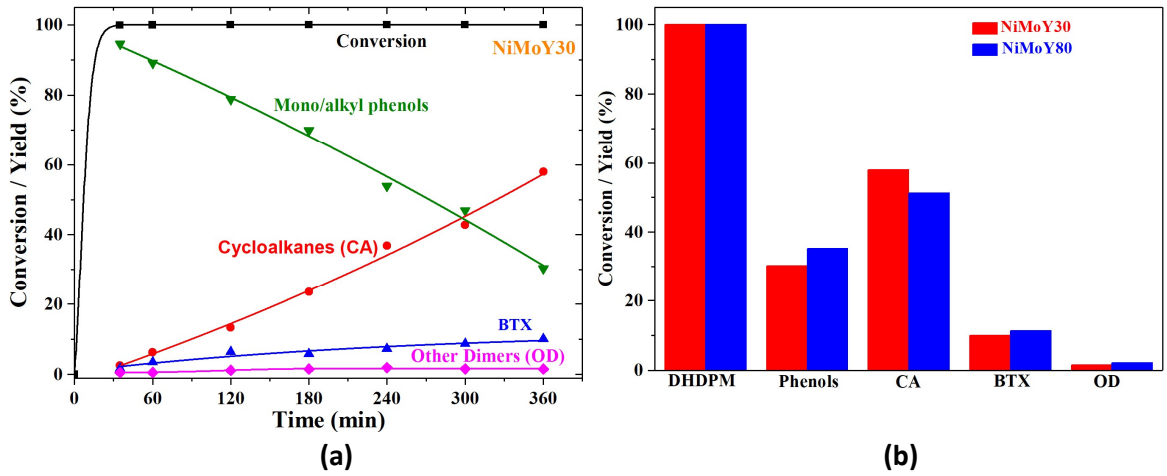

Fig.18 (a) NiMoY30 conversion and yield of products and intermediates during HDO of DHDPM in an autoclave at 345 °C, 50 bar, and 1000 rpm, (b) comparison between NiMoY30 and NiMoY80 final conversion and yield of products.

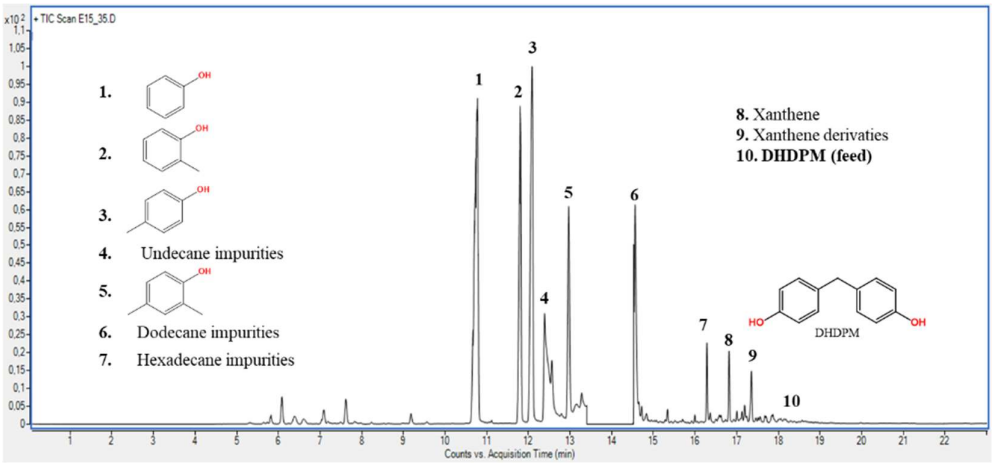

Fig.19 Observed phenol and cresols after 35 min of hydrotreatment of DHDPM at 345 °C, 50 bar, and 1000 rpm over NiMoY30.

4.2.3 HDO of 2-phenylphenol (2PP)

The catalysts were further evaluated with 2PP having recalcitrant 5-5' linkages as present in lignin. **Fig.20** illustrates the conversion of 2PP and the evolution of reaction intermediates and products. Based on the identified products/intermediates via GC-MS spectra (shown in **Fig.21**)

a proposed reaction **scheme 5** is also shown. The conversion of 2PP is slow, reaching a value of ~90% over NiMoY30 after 360 min. At the beginning of the reaction, 2PP isomerizes to form 3-phenylphenol (3PP) and 4-phenylphenol (4PP) which deoxygenates to form biphenyl (BP) as the reaction progresses. The subsequent hydrogenation of BP yields phenylcyclohexene (CHEB), cyclohexylbenzene (CHB), cyclopentylmethylbenzene (CPMB). CHEB and CHB were present in low quantities indicating their faster conversion to CPMB. Finally, CPMB decomposes to yield benzene (B) and methylcyclopentane (MCP). The product spectrum obtained is consistent with previous studies over Pt and NiMo containing catalysts [63, 124-126]. However, the difference is the formation of a higher yield of benzene and MCP (shown in **Fig.21**). Like the other feedstocks, NiMo with SAR of 30 shows higher conversion and higher yield of deoxygenated fractions. NiMoY12, on the other hand, shows the least conversion, HDO, and hydrocracking reactions. The intermediate results for NiMoY80 infer that apart from high surface acid site density, proximity and accessibility of the acid and deoxygenation sites are also important to aid the desired reactions. With its high surface acid site density, NiMoY12 was found to isomerize 2PP to 3PP hastily, while for NiMoY80, having more mesopores and external surface and slightly better NiMoS dispersion, conversion of phenylphenols progresses faster. These results demonstrate that a direct cleave of 5-5' linkages is unfavored, but it rather proceeds through a cascade of HDO, hydrogenation, and C-C hydrogenolysis reactions.

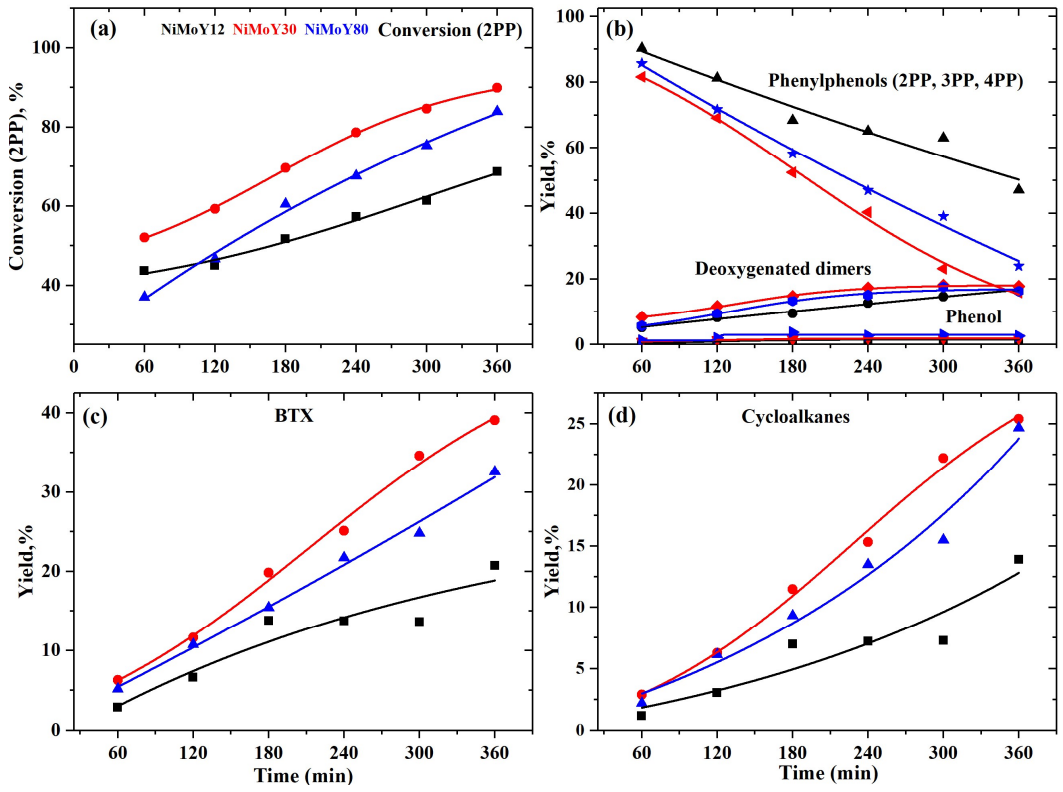

Fig.20 Effect of SAR on the cleavage of 2PP over NiMoS-USY. Reaction conditions: 345 °C, 50 bar, and 1000rpm.

Scheme 5 A proposed reaction scheme for the cleavage of 2PP over NiMoS-USY zeolites**.**

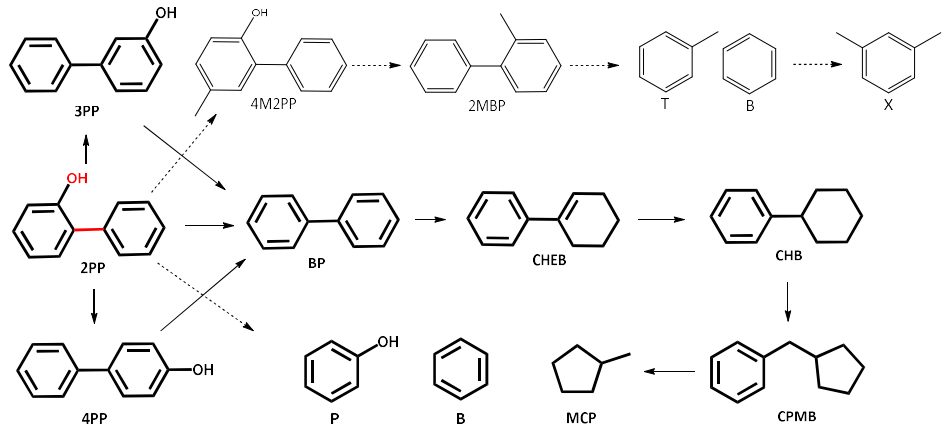

PP: Phenylphenol, BP: Biphenyl, CHEB:Phenylcyclohexene, CHB: Cyclohexylbenzene, CPMB: Cyclopentylmethylbenzene, P: Phenol, B: Benzene, MCP: Methylcyclopentane, 4M2PP:4-methyl-2-PP, 2MBP:2-methyl-BP

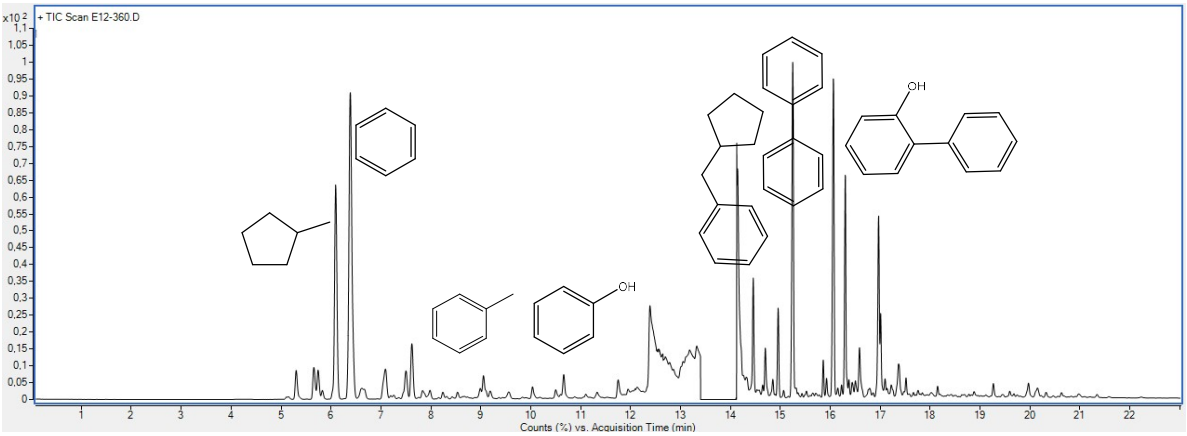

Fig.21 GC-MS spectra showing products/intermediates after 360 min of hydrotreatment of 2PP over NiMoY30**.**

4.2.4 Catalyst Characterization

The nitrogen physisorption data of the synthesized/sulfided catalysts are shown in **Fig.22** and **Table 10**. As the SAR ratio increases, an increase in the total/external BET surface area and mesopore volume of the zeolite materials was observed. Variable pore blockage has been noticed for all the supports due to the impregnation of Ni and Mo. Total acidity and Brønsted acidity of the synthesized catalyst were measured via NH_3 and ethylamine-TPD respectively. As expected, both acidities decrease with increasing SAR ratio due to dealumination. Based on the deconvolution (**Fig.23**) of NH_3 desorption peaks, it is evident that Y30 shows a higher fraction (55%) of stronger acid sites, desorbing NH_3 above 400 °C, than Y12 (40%) and Y80 (37%). Impregnation of NiMo shows a significant reduction of these stronger acidic sites and a corresponding increase of the moderate strength acid sites (54-61%) in the desorption temperature region of 250-400 °C. As can be seen in **Table 11**, impregnated catalysts show lower BAS site densities probably due to metal-acid exchange.

Table 10 Textural properties of the synthesized and sulfided catalysts, where the elemental composition is measured by ICP-SFMS and elemental analysis.

Catalyst	Elemental composition, wt. %				N_2 physisorption			
					$S_{a,\ total}$	$S_{a,external}$	$V_{p,total}$ ($V_{p,meso}$)	d_p
	SiO_2/Al_2O_3[b]	Mo	Ni	S	m^2/g	m^2/g	cm^3/g	Å
Y12	12	-	-	-	670	136	0.46 (0.20)	47.7
NiMoY12	-	12.8	4.9	8.6	291	87	0.26 (0.16)	37.3
Y30	30	-	-	-	808	244	0.53 (0.27)	46.9
NiMoY30	-	12.4	4.6	9.8	435	96	0.33 (0.18)	44.3
Y80	80	-	-	-	815	298	0.54 (0.30)	41.0
NiMoY80	-	13.4	4.5	9.8	462	164	0.33 (0.20)	38.6

S_a=BET surface area, V_p = Pore volume, d_p = Average pore sizes for mesopores, b= given by Zeolyst international.

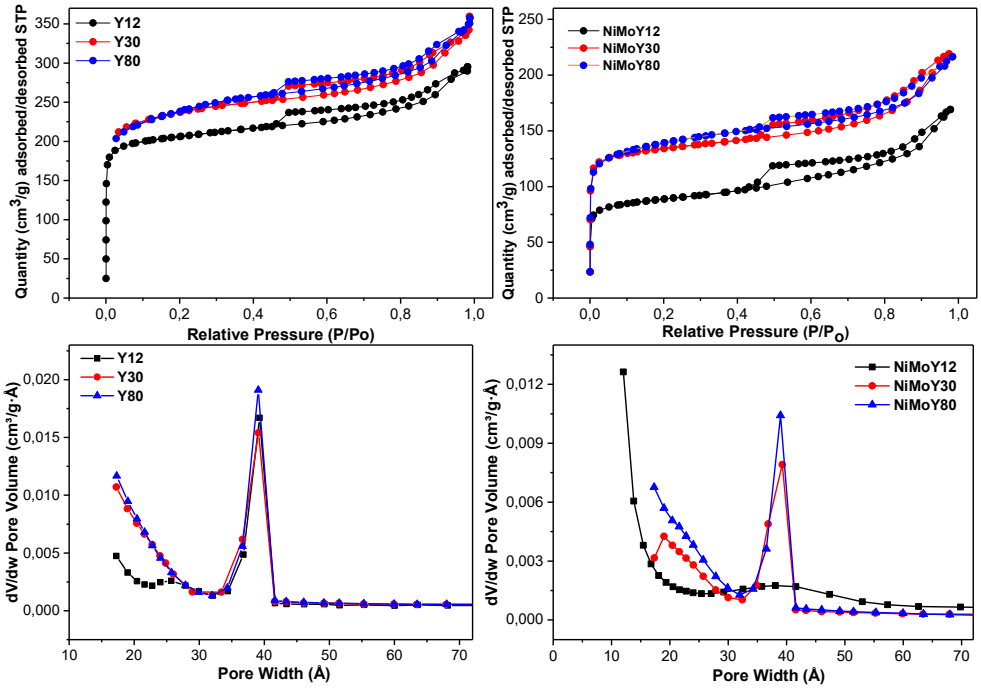

Fig.22 N_2 physisorption data of the Y zeolites and NiMo impregnated Y zeolites.

Sulfided catalysts were analyzed via XPS to illustrate their oxidation state. Analysis of the Mo3d, Ni2p and S2p core level spectra (shown in **Fig.24a-c**) demonstrates the presence of metal sulfide species Deconvoltuion reveals the existence of Mo as Mo^{4+} (228.6 ± 0.1 eV, MoS_2), Mo^{+5} (229.7 ± 0.1 eV, Mo-oxysulfides), and Mo^{6+} (232.2 ± 0.1 eV) species, Ni as NiS_x (852.8 ± 0.1 eV), NiMoS (854.3 ± 0.1 eV), and Ni^{2+} (856 ± 0.2 eV) [1]. Sulfur exists as elemental sulfur (S2s peak in Mo3d) and as metal sulfides (characteristic doublet at 161.5 ± 0.2 and 162.7 ± 0.2 eV). Overall Mo is mostly present as Mo^{4+} with little variation among the catalysts (**Table 12**). TEM analysis (**Fig. 24d**) revealed the presence of Ni-promoted MoS_2 slabs with 0.62 nm of interlayer distance [110]. Shorter average slab length and analogous stacking of promoted MoS_2 slabs led to the formation of slightly higher Mo dispersion over NiMoY30.

Table 11 Distribution of acid sites measured from the desorption of NH_3-TPD. The Brønsted acidity was measured using $C_2H_5NH_2$-TPD.

Catalyst	Total acidity (NH_3-TPD)	Relative acidity (%) *			Brønsted acidity ($C_2H_5NH_2$-TPD)
	(μmol g^{-1})	≤250 ° C	250–400 °C	>400 °C	(μmol g^{-1})
Y12	684	23	37	40	549
NiMoY12	686	38	54	8	368
Y30	415	18	27	55	386
NiMoY30	571	34	61	5	324
Y80	242	27	36	37	221
NiMoY80	477	38	59	3	202

***** Relative acidities are based on the total acidity of each catalyst.

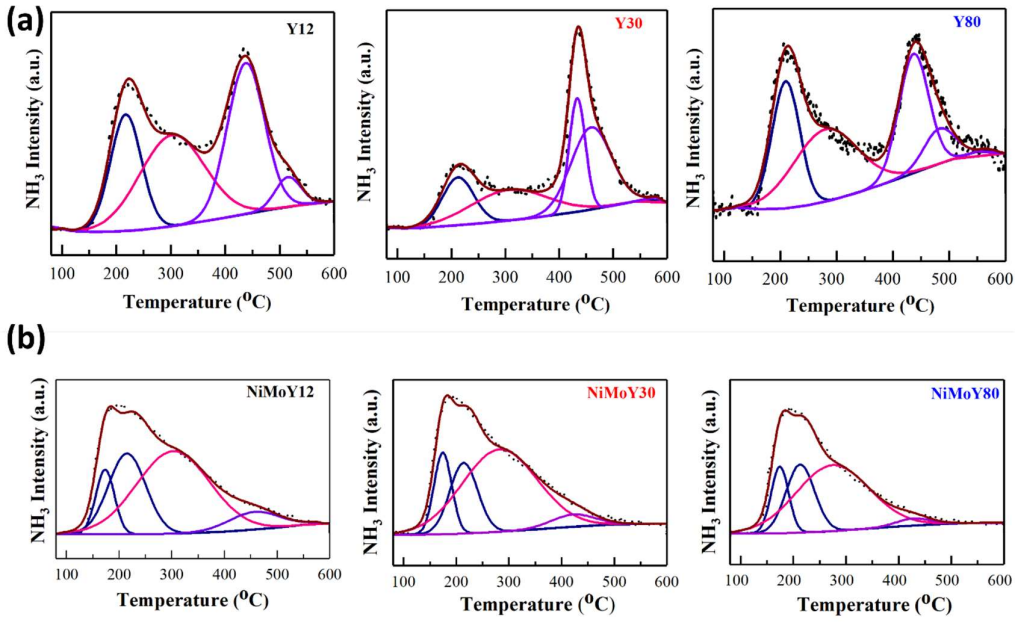

Fig.23 Deconvolution of NH_3 desorption observed during TPD experiments, (a) USY zeolites (b) NiMo-impregnated USY.

Table 12 XPS and TEM characterization of the metal sulfides.

Catalyst	Mo Sulfidation (%)			Average Slab length (nm)	Average Stack number	MoS_2 dispersion(f_{Mo})
	Mo^{4+}	Mo^{5+}	Mo^{6+}			
NiMoY12	82	11	7	4.8	4.0	0.23
NiMoY30	75	14	11	4.2	4.0	0.26
NiMoY80	77	11	12	4.6	3.8	0.24

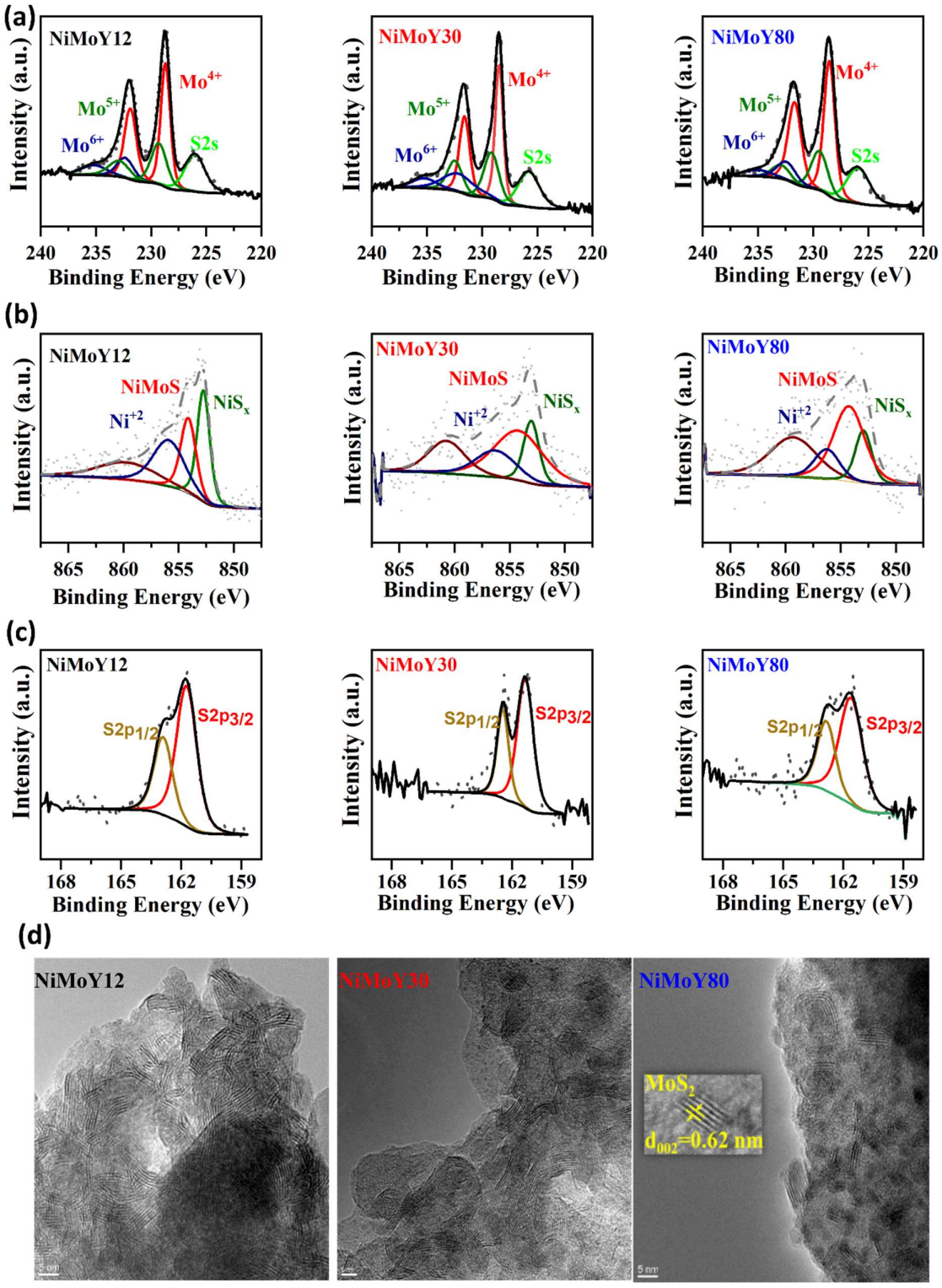

Fig.24 Deconvolution of XPS core level (a) Mo3d, (b) Ni2P, (c) S2P spectra for NiMoY12, NiMoY30, and NiMoY80, (d) HR-TEM images of Ni promoted MoS_2 over ultra-stable Y zeolites.

4.3 Elucidating the role of NiMoS-USY during the hydrotreatment of Kraft lignin

It has been demonstrated that NiMo sulfides over Y zeolites show enhanced cleavage of C-O-C and C-C in lignin dimers. As discussed in the above sections it is due to the interaction effect of sulfide phases and acidic sites of the resulting catalyst. With this information, the focus of this study is to elucidate their role while upgrading a more complex feedstock, Kraft lignin by a one-pot hydrotreatment process. To examine their role, additional experiments were performed using unsupported metal sulfides and Y zeolites as a physical mixture containing the same amount of metallic sites and acidic sites as in impregnated catalyst. Furthermore, the effect of dealumination and desilication of Y zeolites have been investigated for NiMo impregnated catalysts in valorizing lignin.

4.3.1 Hydrotreatment using impregnated NiMoS over ultra-stable Y zeolites

Fig.25 shows the yield of liquid-phase products and solid residue after the hydrotreatment of Kraft lignin in a batch reactor at 400 °C, 35 bar of H_2 (25 °C), 1000 rpm for 5h. Without a catalyst (blank), thermal depolymerization under the hydrogen atmosphere occurs, where repolymerization/coupling reactions dominate leading to the formation of a high solid residue yield after 5 h of hydrotreatment with a low liquid yield (~18 wt.%). The introduction of Y zeolites reduces these undesirable reactions slightly with Y80, whereas for Y30 solid residue yield is reduced by 20%, giving rise to a liquid yield of ~21 wt.%. For sulfided NiMo impregnated zeolites (either dealuminated or desilicated), the repolymerization reactions were suppressed significantly. NiMoY30 shows a notable liquid yield of 30.5 wt.% with the lowest solid residue yield compared to the other impregnated catalysts in **Fig.25**. It is important to mention that NiMoY150 and NiMoY200 were obtained via dealumination of Y80 and subsequent impregnation of metals. To elucidate the effect of diffusion limitations, Y80 was also desilicated (see Section 3.1*j* producing catalyst NiMoDY80. For the dealuminated catalysts (**Fig.25**) liquid yield drops, while solids residue yields increase slightly due to the loss of acidity. For desilicated NiMoDY80 (NiMo impregnated over desilicated Y80) there is only a small variation in the liquid and solid residue yields. These results directed us to investigate further the role of NiMoS when impregnated over Y zeolites, especially Y30. To enable this, unsupported UNiMoS was synthesized hydrothermally and used as a stand-alone catalyst and in combination with Y30 as a physical mixture.

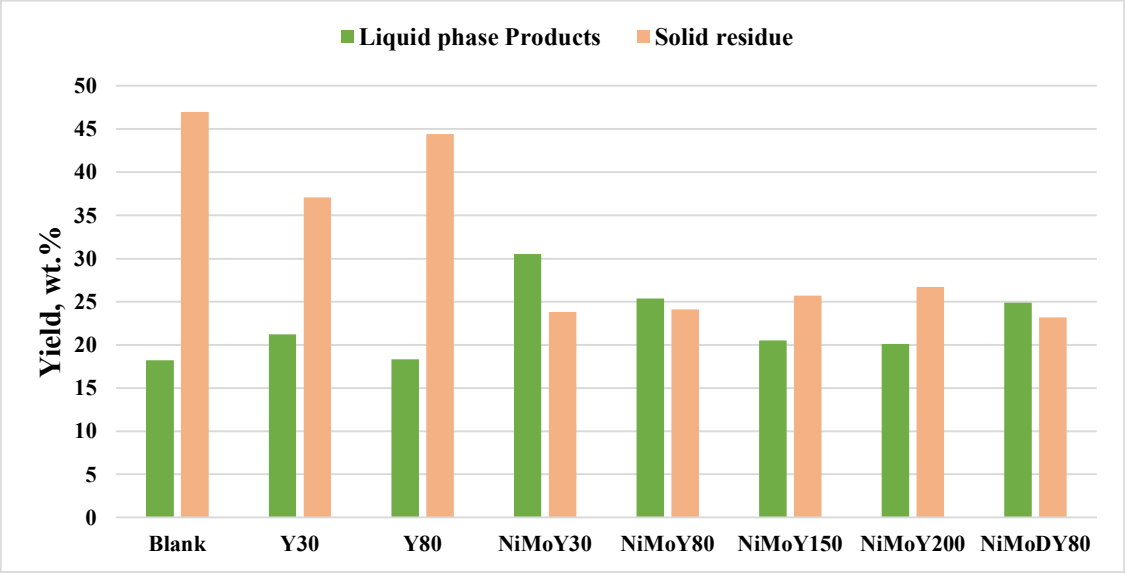

Fig.25 The yield of liquid-phase products and solid residue after the hydrotreatment of Kraft lignin over sulfided NiMo, Y zeolites and in absence of catalyst (blank) at 400 °C, 35 bar H_2 (@25°C), and 1000 rpm for 5h.

4.3.2 Role of NiMoS and Y30 in Kraft lignin hydrotreatment

Fig.26 shows an example of a 2D GC x GC-MS image used to identify and quantify the groups of products from the hydrotreatment of Kraft lignin. Deoxygenated products include cycloalkanes, alkylbenzenes, Indans/Naphthalenes/Biphenyls, and polycyclic aromatics (mainly three or higher ring hydrocarbons). Oxygenated products are grouped as 'phenols' and 'other oxygenates' and include primarily aldehydes, ketones, and alcohols.

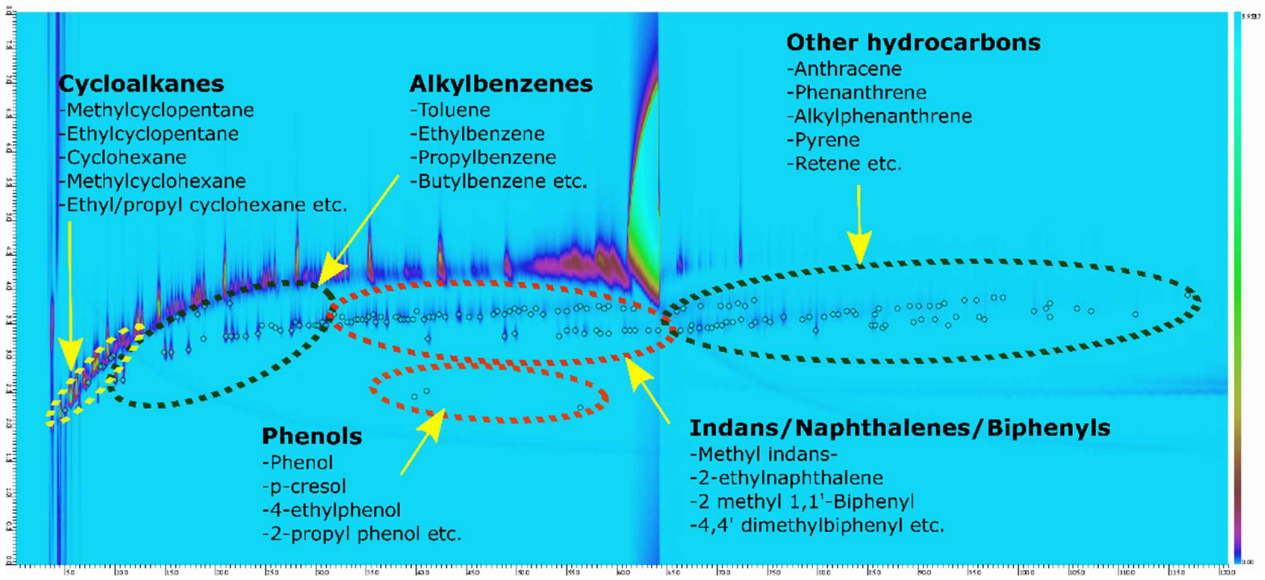

Fig.26 GC x GC 2D chromatogram of the liquid phase products evolved from the hydrotreatment of Kraft lignin.

Table 13 and **Fig.27** show the yield and selectivity of liquid products after 5h hydrotreatment of Kraft lignin in an autoclave reactor. As can be seen, an equivalent amount of UNiMoS as in sulfided NiMoY30 gives a liquid yield of 23.5%, which is lower than NiMoY30 while for the physical mixture, UNiMoS+Y30 the yield is close to that of NiMoY30. However, the yield of solid residue for the UNiMoS reached 25.2 wt.% whereas for the physical mixture it drops to a low value of 16.7 wt.% after 5 h. Lower solid residue for the physical mixture implies that more active sites are accessible by the lignin fragments/radicals (e.g., phenoxyl, methoxy, methyl, etc.) to undergo stabilization [136]. It also infers that acidic sites of the zeolite and hydrogenation/ deoxygenation sites of NiMo are a good combination to stabilize fragments and/or to convert them and their initial products to other products than solid residue. Furthermore, it also indicates that when impregnated active sites (NiMoS) and acidic sites are less accessible, it results in a higher solid residue for the impregnated NiMoY30. It is noteworthy to mention that NiMoY30 (impregnated) and UNiMoS+Y30 (physical mixture) have the same amount of metals and acidic sites despite their differences in morphology and dispersion (discussed in section 4.3.3)

Table 13 Yield and selectivity of products from the hydrotreatment of Kraft lignin over sulfided NiMo and USY zeolite at 400 °C, 35 bar H_2 (@25°C), and 1000 rpm for 5h.

Catalyst	**Liquid Yield. wt. %**	**Liquid product selectivity. %**					**Solid residue. wt. %**
		Cycloalkanes/ Alkylbenzenes	Phenols	Indans/Napthalenes/ Biphenyls	Polycyclic aromatics	Other oxygenates	
Blank	18.2	10	60	5	13	13	47
Y80	18.2	10	60	5	13	13	44.4
Y30	21.2	29	47	10	10	4	37.1
NiMoY30	30.5	61	1	27	9	2	23.8
UNiMoS	23.5	42	25	8	24	2	25.2
UNiMoS +Y30	29.1	30	27	20	21	2	16.7
NiMoY30*	38.9	79	0	14.5	4.9	1.5	16.4

*extending residence time to 8 h and decreasing lignin catalyst ratio from 3:1 to 2:1.

These experiments with unsupported catalysts reinstate that acidity of the support can also play a key role in fragment stabilization and further upgrading steps. However, high liquid yield with NiMoY30 compared to others in **Table 13** can be ascribed to the surface proximity of Ni-promoted MoS_2 and acidic sites when impregnated. This lowers the diffusion distance for the stabilized fragments for further deoxygenation, isomerization, and hydrocracking reactions.

Thermal depolymerization without catalyst shows high selectivity for the formation of alkylphenols. With Y30, an increase in the cycloalkane and alkylbenzene selectivity has been noticed. Impregnated NiMoY30 shows a noteworthy, 61% selectivity for the cycloalkane and alkylbenzene fraction. UNiMoS and the physical mixture show a clear drop in the selectivity for this fraction, however at the expense of higher selectivity for phenols compared to NiMoY30. An extended 8h reaction with higher catalyst loading for NiMoY30 showed a remarkable monocyclic and alkylbenzene selectivity of 79% with an overall liquid yield of 38.9

wt.% and a solid residue yield of 16.4 wt.%. Interestingly, the formation of polycyclic aromatics is lower over NiMoY30 than the physical mixture showing further the importance of the proximity of actives sites. This could also be due to the hydrocracking reaction facilitated by the Brønsted acidic sites [137].

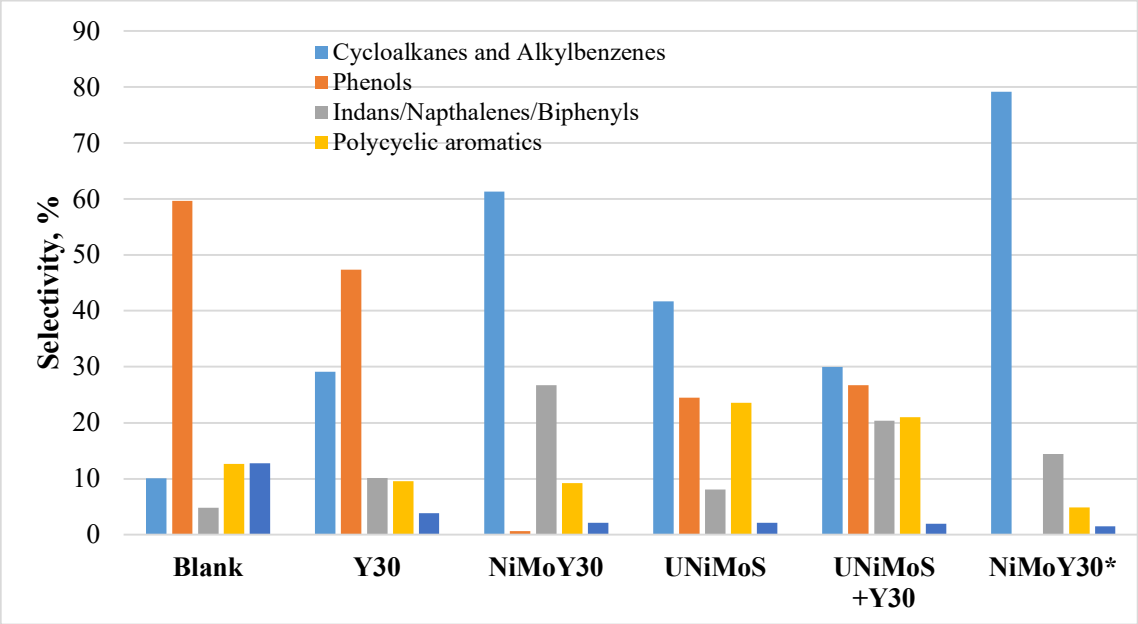

Fig.27 Liquid phase product selectivity for the hydrotreatment of Kraft lignin in absence of catalyst (Blank) and over NiMo and Y-zeolite catalysts at 400 °C, 35 bar of H_2 (@25°C), and 1000 rpm.

4.3.3 Catalyst characterization

The N_2 physisorption data are shown in **Table 14**. Dealumination of Y80 via oxalic acid and desilication via PDA-assisted NaOH shows a corresponding increase in the mesopore sizes, their volumes, and external surface areas. Such an increment can aid large lignin fragments to reach active sites. Indeed, a small decrease in the polycyclic aromatic product selectivity was observed for NiMo impregnated over dealuminated/desilicated USY with a corresponding increase in the phenols/cycloalkane/alkylbenzene selectivity (**Table 13**). NiMoY30 showed a high BET surface area with an average mesopore size of 4.4 nm. Hydrothermally synthesized UNiMoS shows a low BET surface area with larger average mesopores of 11.5 nm. ICP-MS analysis shows Mo and Ni loading remains in the range of 12-13 wt.% and 3.7-4.5 wt.% respectively giving rise to a Ni/(Ni+Mo) molar ratio of 0.33-0.37. For unsupported catalysts, this ratio was maintained at 0.5.

The acidity of the catalysts is shown in **Table 15**. NiMo impregnated Y zeolites showed a higher acidic fraction than the parent Y zeolites. Deconvolution of the NH_3 desorption peak shows that the total acidity fraction above 250 °C decreases with increasing SAR while the acidity fraction below 250 °C follows the opposite trend. This implies that high SAR catalysts are composed of fewer stronger acidic sites in addition to their low total acidity. As can be seen

from **Fig.28a** a good correlation between the overall/Brønsted acidities and liquid product yield can be observed.

Table 14 Composition and textural properties of the synthesized and sulfided catalysts.

Catalyst	Elemental composition. wt. %				N_2 physisorption			
					$S_{a.\,total}$	$S_{a.\,external}$	$V_{p.total}$ ($V_{p.meso}$)	d_p
	SiO_2/Al_2O_3[b]	Mo	Ni	Atomic ratio Ni/(Ni+Mo)	m^2/g	m^2/g	cm^3/g	Å
Y30	25	-	-	-	801	234	0.54 (0.26)	40.9
NiMoY30	-	12.7	4.5	0.37	514	126	0.33 (0.14)	44.3
Y80	88	-	-	-	808	243	0.56 (0.29)	39.3
NiMoY80	-	13.0	4.4	0.36	500	165	0.33 (0.17)	37.8
Y150	146	-	-	-	792	279	0.57 (0.32)	41.3
NiMoY150	-	12.8	4.4	0.36	398	175	0.33 (0.20)	41.6
Y200	212	-	-	-	737	268	0.57 (0.34)	43.8
NiMoY200	-	12.6	4.4	0.36	423	148	0.32 (0.19)	43.8
DY80	69	-	-	-	662	353	0.68(0.53)	49.3
NiMoDY80	-	12.4	3.7	0.33	344	213	0.40(0.34)	50.3
UNiMoS	-	-	-	0.50	49	49	0.22	115.2

S_a=BET surface area. V_p = Pore volume. d_p = Average pore sizes for mesopores. b= measured by ICP-SFMS.

Table 15 Total acidity and Brønsted acidity of the synthesized catalysts measured by NH_3 and ethylamine temperature-programmed desorption.

Catalyst	Total acidity(NH_3-TPD)	Relative acidity (%) *		Brønsted acidity ($C_2H_5NH_2$-TPD)
	($\mu mol\ g^{-1}$)	≤ 250 ° C	> 250 °C	($\mu mol\ g^{-1}$)
Y30	478	-	-	386
NiMoY30	608	52	48	300
Y80	248	-	-	221
NiMoY80	424	59	41	217
NiMoY150	397	77	23	123
NiMoY200	348	-	-	102
NiMoYDY80	515	64	36	222
UNiMoS	158	-	-	-

*Relative acidities are based on the total acidity of each catalyst.

Based on the product spectrum in **Fig.27** it is evident that greater quantities of acidic sites promote lignin depolymerization, isomerization/transalkylation, hydrocracking, and dehydration reactions that combinedly increase the yield of alkylbenzene and monocyclic and lower the yield of polycyclic. The solid residue yield does not correlate well to the differences in the acidities of the catalysts (**Fig.28b**). However, a strong correlation has been observed for the liquid product yield and the meso/micro pore volume ratio of NiMo impregnated dealuminated USY zeolites (**Fig.28c**).

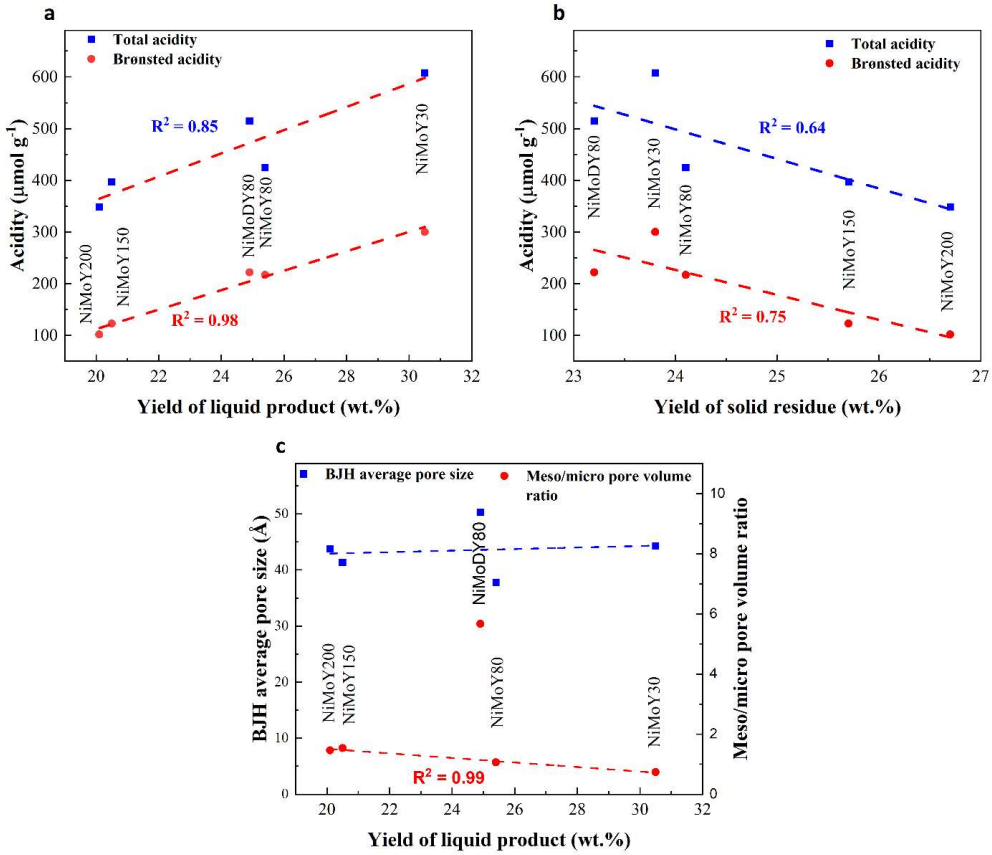

Fig.28 Correlation of the total and Brønsted acidity of the catalyst to the (a) yield of liquid product and (b) yield of solid residue and (c) correlation of the textural properties of the catalyst to the yield of liquid products after the hydrotreatment of Kraft lignin over NiMo impregnated Y zeolites. Dashed lines indicate linear correlations along with their coefficients of determination (R^2-values).

The XRD pattern of the sulfided NiMoS over the zeolites (**Fig.29a**) primarily showed reflections from the parent zeolite demonstrating that the NiMo phases are well dispersed, or the phases are of low crystallinity. Unsupported UNiMoS shows weak reflections at 2θ values of 14°, 49.5°, and 59° indicating the presence of (002), (105), and (103) planes of hexagonal MoS_2 (**Fig.29b**). Additional peaks at 27.3°, 31.5°, 35.3°, 38.7°, 45.3°, 53,6°, 58.7° shows the characteristic (111), (200), (210), (211), (220) and (311) and (230) planes of NiS_2 [25, 138-140]. This demonstrates unsupported UNiMoS is composed of both NiSx and MoS_2 phases.

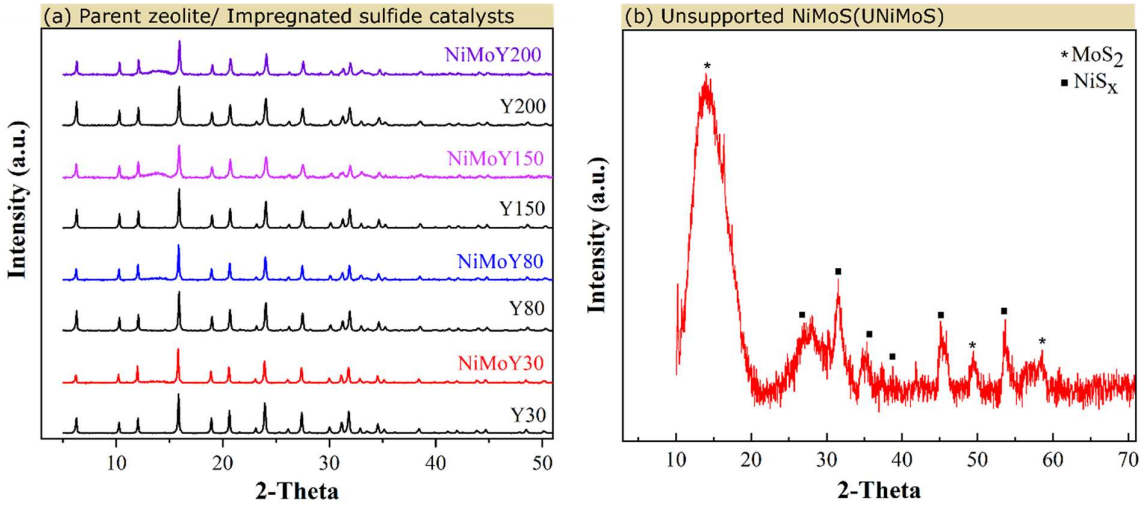

Fig. 29 X-ray diffraction patterns of (a) parent zeolites and zeolites impregnated NiMo sulfides, (b) Unsupported NiMoS (UNiMoS).

H_2-TPR results are shown in **Fig.30** for NiMoY30 and UNiMoS. As-synthesized NiMoY30 required a very high temperature (~580 °C) to be reduced. Conversely, sulfided NiMoY30 starts uptake of H_2 at a lower temperature than UNiMoS which could be related to the existence of non-stoichiometric or weakly bonded sulfur on the support [141]. Also, sulfided NiMoY30 shows a peak at ~330 °C and UNiMoS at~415 °C representing the presence of strongly bonded sulfur. Furthermore, H_2 uptake for NiMoY30 was completed at a temperature lower than UNiMoS indicating the labile nature of Mo-S_2 bonds. The H_2 uptake profiles for the sulfided catalysts occurred simultaneously with the release of a small amount of hydrogen sulfide indicating the formation of sulfur vacancies responsible for deoxygenation/ hydrogenolysis reactions [17]. For NiMoY30, a delayed H_2S release shows either the high-temperature requirement for the creation of more sulfur vacancies or partial diffusion resistance of H_2S out through the Y30 at the experimental conditions. Deoxygenation activities of the impregnated sulfided NiMoY30 and UNiMoS thus can differ during the hydrotreatment of Kraft lignin. Indeed, higher overall deoxygenation can be observed for the impregnated NiMoY30 (**Table 13**). UNiMoS and UNiMoS+Y30 show lower deoxygenation, on the other hand, but can stabilize more lignin fragments leading to the lower solid residue for the latter. Since the lignin degradation temperature is lower than the H_2 uptake temperatures of both NiMoY3O and UNiMoS, it can be expected that at low temperatures thermally driven repolymerization/ coupling reaction will dominate before the catalysts are activated. To emulate the H_2 uptake characteristics, an experiment with sulfided NiMoY30 was conducted until the temperature reached 400 °C followed by rapid cooling of the reactor. This gave a solid residue yield of 35 wt.% indicating the dominance of these coupling reactions, especially at low temperatures where the NiMoS is less active, or the number of active sites is limited. Increasing the number of catalytic active sites can then play a crucial role [98]. Indeed, an increase in the catalyst loading of NiMoY30 (**Table 13**) showed a remarkable increase in the liquid/bio-oil yield producing mostly alkylbenzene and monocyclics (~79% selectivity).

XPS results on the sulfided NiMoY30 (impregnated) and UNiMoS (unsupported) are shown in **Table 16**. The analysis shows the presence of metal sulfides as MoS_2 (228.6 ± 0.1 eV), NiS_x (852.8 ± 0.1), and NiMoS (854.2±0.2). A Mo-oxysulfide phase (Mo^{5+}) has also been observed for both catalysts, however a little higher over UNiMoS. Also, a higher fraction of NiS_x has been observed for NiMoY30. Surprisingly, the surface Ni/(Ni+Mo) ratio was found to be much lower for UNiMoS than NiMoY30 demonstrating that Ni remains mostly in the bulk. TEM analysis showed (**Fig.31**) a uniform distribution of Ni, Mo, and S over a representative area. HRTEM images depict the typical fringes/layered structure of MoS_2. The average slab length for UNiMoS was found to be higher than for NiMoY30 and vice versa for the average stacking shown in **Table 16**. This leads to high dispersion of edge and corner Mo atoms compared to total Mo in the NiMoY30 catalyst. On the other hand, UNiMoS showed more edge Mo atoms than the corner sites. Due to this difference, more hydrogenolysis activity can be observed over UNiMoS. Moreover, the features of the MoS_2 morphology over both catalysts are different: a more rounded or curved MoS_2 layer can be observed for NiMoY30 due to the influence of the support while for UNiMoS it is sharper or bent and porous in nature.

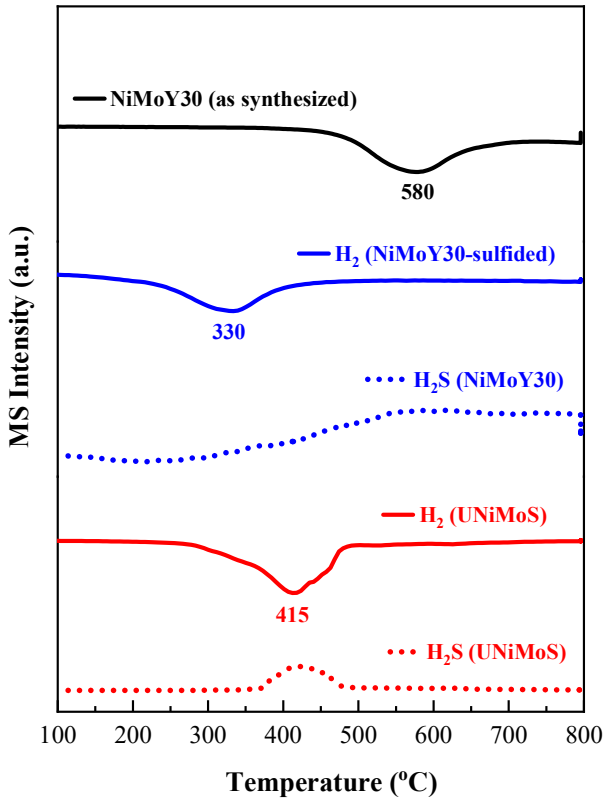

Fig.30 H_2 uptake characteristics of UNiMoS, sulfided and as-synthesized NiMoY30 during H_2 temperature-programmed reduction.

Table 16 Data from the XPS and TEM analysis of the supported/unsupported sulfided catalysts.

Catalyst	Mo Sulfidation (%)	Ni Sulfidation (%)			Ni/(Ni+Mo) atomic ratio	Average Slab length (nm)	Average Stacking	MoS_2 dispersion, f_{Mo}	Edge to corner ratio
	Mo^{4+}/Mo^{5+}	NiS_x	NiMoS	Ni^{2+}					
UNiMoS	68/20	7	72	21	0.05	6.3	2.9	0.156	8.4
NiMoY30	75/13	24	66	10	0.22	4.3	3.8	0.254	5.2

XPS and TEM analysis showed that sulfided NiMoY30 and UNiMoS contain NiSx and MoS_2 phases. This is also consistent with the XRD measurements for UNiMoS. It is reported that the presence of NiSx can increase the hydrogenation activity of MoS_2 [142]. Also, the synergetic effect of NiS_2 and MoS_2 has been found to increase the rate of hydrogenation and HDO of bio-oil oxygenates [24]. However, excess NiS_x was found to hinder access to MoS_2, thus lowering the activity [143]. H_2-TPR shows that Ni integration lowers the hydrogen uptake temperature more for NiMoY30 than UNiMoS. NiMoY30 reactivity during hydrotreatment can largely be related to its ability to facilitate hydrogen activation. In addition, higher dispersion of MoS_2 gives rise to a larger amount of edge Mo atoms rather than corners, which enhances the hydrogenolysis and hydrogenation reaction. Furthermore, the acidity of NiMoY30 contributes to isomerization, hydrocracking and dehydration reactions.

4.3.4 Regeneration of catalyst and characterization of solid residue

TGA analysis was performed on the recovered NiMoY30 containing solid residue and the result is shown in **Fig.32(a)**. As shown 45% weight loss can be seen upon heating the sample to 500 °C. Based on this profile, recovered NiMoY30 was calcined in air at 450 °C for 3 h. XRD patterns in **Fig.32(b)** confirm the regeneration of the recovered NiMoY30. This transformation however slightly increased the particle size of MoO_3 as can be seen by an intensified peak at $2\theta=26.7°$. This also shows that the zeolite structure remained stable during these thermal cycles of calcination, sulfidation, and regeneration. To understand the nature of the solid residue solid-state-cross-polarization (CP) ^{13}C NMR was conducted and the results are shown in **Fig.33** with comparison to the Kraft lignin analysis. The characteristic methoxy groups in Kraft lignin can be identified by a peak around 57 ppm. Reductive thermal and catalytic depolymerization of Kraft lignin shows significant demethoxylation and the liquid phase shows the existence of demethoxylated products e.g., alkylphenols. Aliphatic carbon-hydrogen moiety and aromatic carbons (C-C, C-H, and C-O) can be observed via a shoulder below 50 ppm and in the range of 100-160 ppm. Kraft lignin shows a sharp peak around ~149 ppm indicating the presence of C-O groups. Thus, the resulting solid residue is more carbonaceous in nature than Kraft lignin and scarcely contains methoxy groups and much fewer C-O groups.

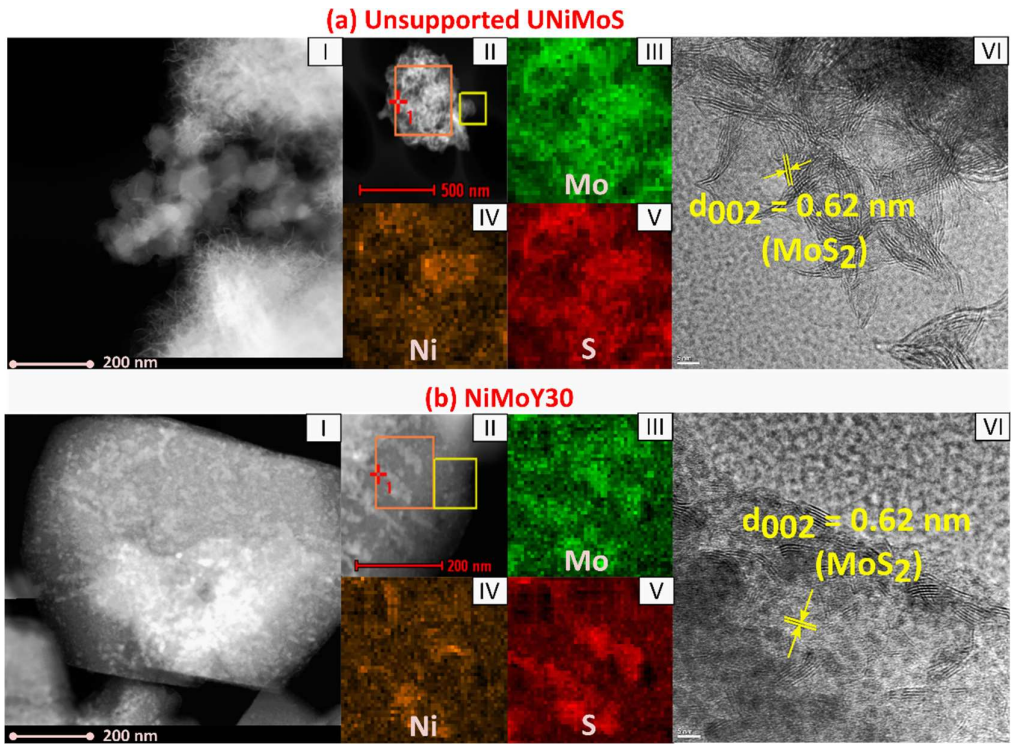

Fig.31. HAADF-STEM/HRTEM imaging and EDX mapping of (a) Unsupported NiMoS and (b) NiMoY30. Sub images: (I) overview of the materials, (II) overview of the analysis area (orange box), (III) Molybdenum, (IV) Nickel, (V) Sulfur EDX elemental mapping, and (VI) BF-TEM micrograph.

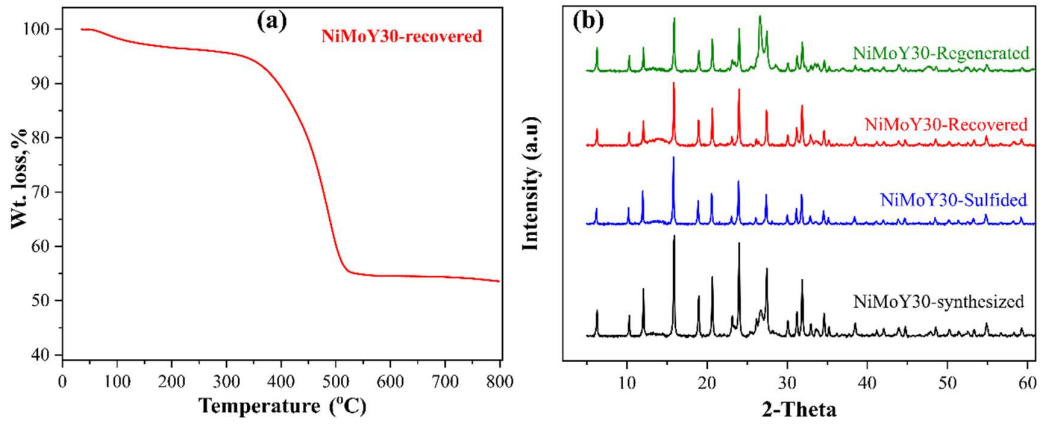

Fig.32 (a) Thermogravimetric analysis of the solids recovered from reactor following NiMoY30 hydrotreatment and (b) XRD pattern of the NiMoY30 following different stages.

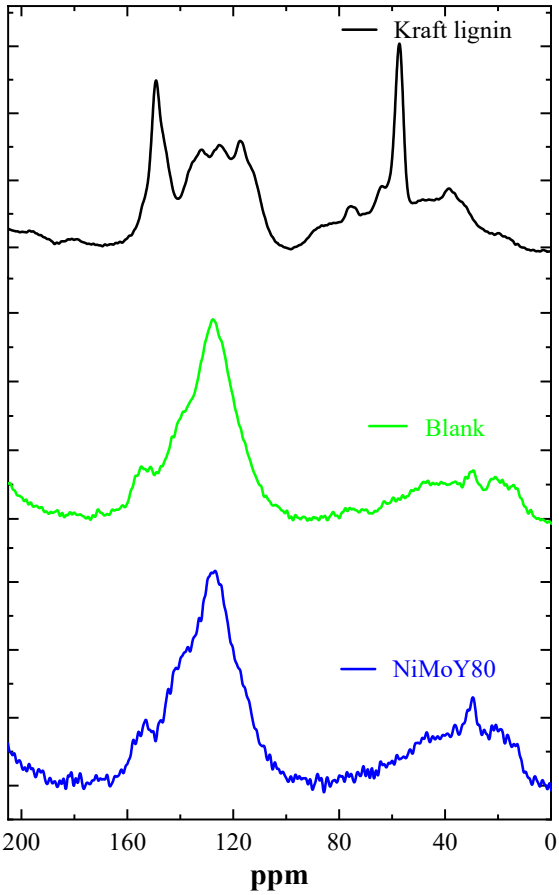

Fig.33 Solid-state-cross-polarization (CP) ^{13}C NMR of Kraft lignin and the solid residue obtained from the hydrotreatment.

4.4 Thermal annealing effects on hydrothermally synthesized unsupported MoS_2 for enhanced deoxygenation of propylguaiacol and Kraft lignin

As described in Section 4.3 Kraft lignin hydrotreatment typically generates alkylphenolics, guaiacolics (e.g., guaiacol, propyl guaiacol) in addition to deoxygenated aromatics and cycloalkanes depending on the reaction conditions and employed catalyst. Deoxygenation activity of such fractions is vital to upgrade them to value added fuel components. Thus, in this study deoxygenation activity of a bio-oil model compound, propylguaiacol has been explored extensively using unsupported MoS_2. In addition, diffusion resistance was observed for complex feed, Kraft lignin over supported catalysts. Hence, Kraft lignin hydrotreatment was also studied using unsupported MoS_2.

4.4.1 Catalyst characterization

Textural properties of the unsupported MoS_2 prepared in this work and bulk MoS_2 (Sigma-Aldrich) are shown in **Table 17**. Bulk MoS_2 has the lowest specific surface area while annealed samples (MoS_2-12a, MoS_2-24a) show higher values. As-synthesized MoS_2 without thermal treatment (MoS_2-12 and MoS_2-24) shows similar specific surface areas indicating the influence of the extended synthesis time. Interestingly, MoS_2-12a shows the highest pore volume and the smallest pore sizes.

Table 17 Physical properties (surface area, pore-volume, and pore size) and HRTEM analysis of the synthesized unsupported MoS_2 catalysts and bulk MoS_2.

Catalysts	Surface area (m^2/g)	Pore volume (cm^3/g)	Pore size (Å)	Average MoS_2 slab length (ΔL)	Average stacking number (Δn)	MoS_2 dispersion (f_{mo})	Edge-to-corner ratio of MoS_2 slabs
MoS_2-12	15.4	0.34	108	5.07	4.01	0.150	6.42
MoS_2-12a	27.8	0.60	83.8	8.41	2.72	0.103	11.6
MoS_2-24	16.2	0.13	317	6.58	3.26	0.130	8.78
MoS_2-24a	37.1	0.11	105	8.71	3.85	0.105	12.1
Bulk MoS_2	4.70	0.03	177	-	-	-	-

As shown in **Fig.34 (a),** as-synthesized MoS_2 (MoS_2-12 and MoS_2-24) shows a weak diffraction peak at 2θ = 14° representing the hexagonal plane (002) of crystalline/bulk MoS_2. It also indicates that the resulting unsupported materials are low in crystallinity. With the annealed MoS_2 (MoS_2-12a, MoS_2-24a), distinct diffraction peaks appeared at 2θ = 14°, 33°, 39°, and 59° corresponding to (002), (100), (103) and (110) planes of MoS_2, illustrating the evolution of crystalline MoS_2 [144]. The Raman spectrum for annealed MoS_2-24a (**Fig.33(b)**) shows characteristic peaks at 379 cm^{-1} (E^1_{2g}), 404 cm^{-1} (A1g), 283 cm^{-1} (E1g), and 454 cm^{-1} (E1g) which corresponds to the existence of 2H-MoS_2 (hexagonal symmetry, trigonal prismatic coordination of metal atom). Other low-intensity peaks at 219 cm^{-1} and 335 cm^{-1}, can be ascribed to the presence of a 1T MoS_2 phase (trigonal antiprismatic or octahedral coordination

of metal atom). The as-synthesized MoS_2-24 shows low-intensity peaks due to low crystallinity.

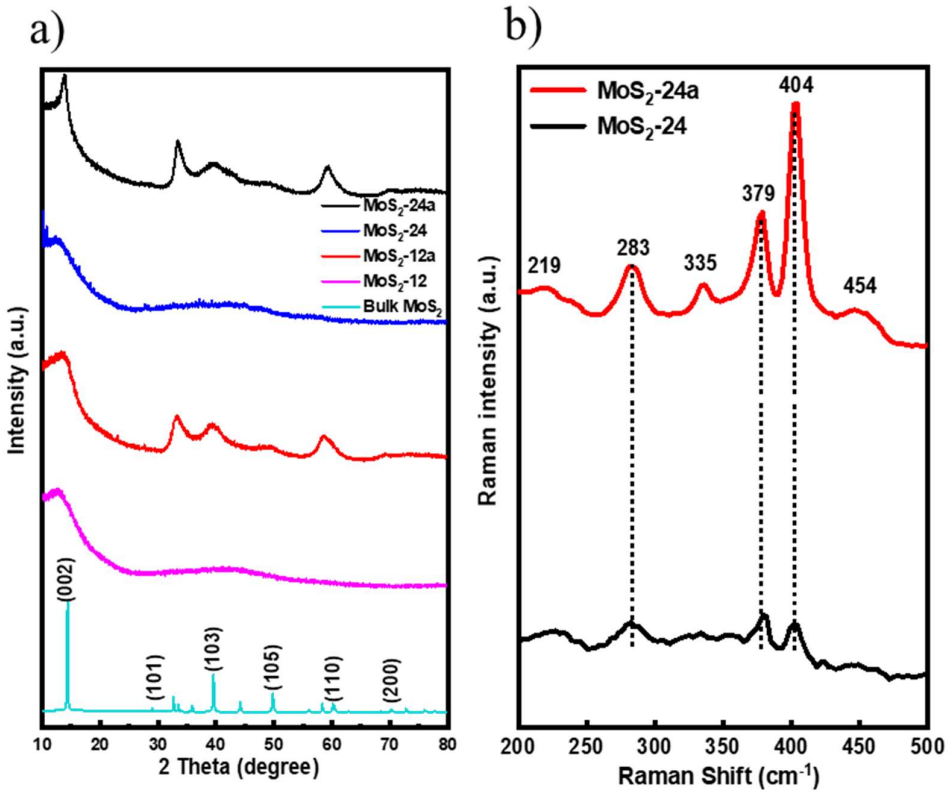

Fig.34 a) XRD patterns for MoS_2-12, MoS_2-12a, MoS_2-24, MoS_2-24a and bulk MoS_2 and b) Raman spectra for MoS_2-24 and MoS_2-24a catalysts.

The deconvolution of the core level Mo3d XPS spectra (**Fig.35** and **Table 18**) illustrates that the Mo^{4+} oxidation state (MoS_2 species), is the dominant fraction in all the as-synthesized and annealed samples. Moreover, the Mo^{5+} oxidation state indicates the presence of oxysulfide species (MoO_xS_y) also present in the as-synthesized samples. The Mo^{6+} oxidation state associated with MoO_3 species can be identified in all samples. Interestingly, the thermally treated sample showed a higher fraction of Mo^{4+} (doublet at 229.3 eV and 235.5 eV), no Mo^{5+} (230 eV), and lower Mo^{6+} (233.4 eV) fractions [145-147]]. A low oxysulfide fraction (Mo^{5+}, MoO_xS_y) in the annealed samples signifies the nearly complete conversion of it to MoS_3 which upon the thermal annealing step further facilitates the thermal decomposition of MoS_3 to MoS_2.

Table 18. Mo 3d composition for MoS_2-12, MoS_2-12a, MoS_2-24, and MoS_2-24a.

Catalyst	Mo 3d composition (area %)		
	Mo^{4+}	Mo^{5+}	Mo^{6+}
MoS_2-12	62.9	22.2	14.9
MoS_2-12a	88.6	-	11.4
MoS_2-24	82.9	11.3	5.8
MoS_2-24a	93.1	-	6.9

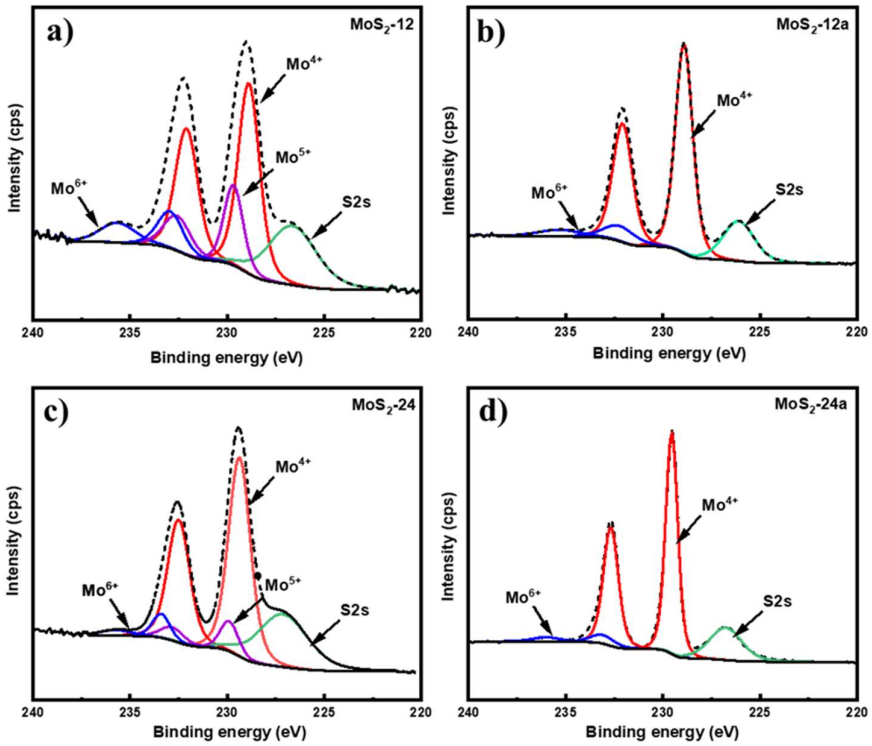

Fig.35 XPS spectra of Mo 3d for a) MoS_2-12, b) MoS_2-12a, c) MoS_2-24, and d) MoS_2-24a.

Fig.36 shows the scanning electron microscopy (SEM) images of the as-synthesized and annealed unsupported MoS_2 samples. Agglomerates of spherical particles in various particle sizes can be easily distinguished in all the SEM images which mainly attributed to the laminar growth of MoS_2 micelles during the hydrothermal synthesis. As evident **from Fig.36 (a,b, e, and f)** as-synthesized MoS_2 consists of larger and small-sized particles while for annealed MoS_2, the particles become uniformly distributed and well dispersed. For instance, the MoS_2-24a sample exhibited the lowest average particle diameter of 190 nm with a narrow particle size distribution. The differences in the morphology of the as-synthesized and annealed catalysts demonstrate the importance of the annealing pretreatment proposed in this study for the further growth and re-distribution of the MoS_2 particles. A MoS_2 sample prepared without the pH adjustment (**Fig.37**) shows an even larger average particle size (~2µm) which is close to the size of bulk commercial MoS_2 (6 µm). This also shows the importance of pH adjustment for the development of MoS_2 micelles.

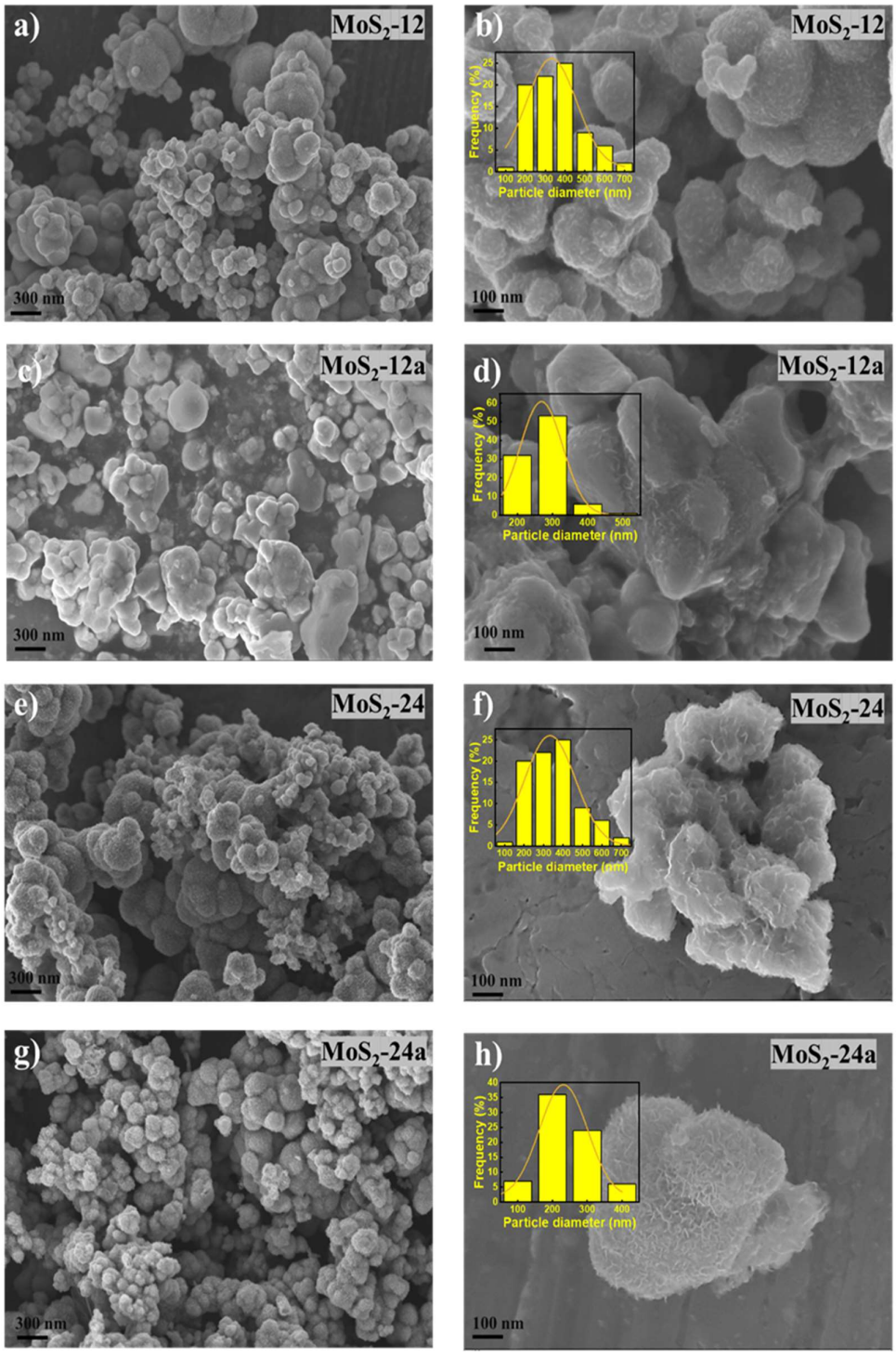

Fig.36 SEM images of a-b) MoS_2-12, c-d) MoS_2-12a, e-f) MoS_2-24, and g-h) MoS_2-24a.

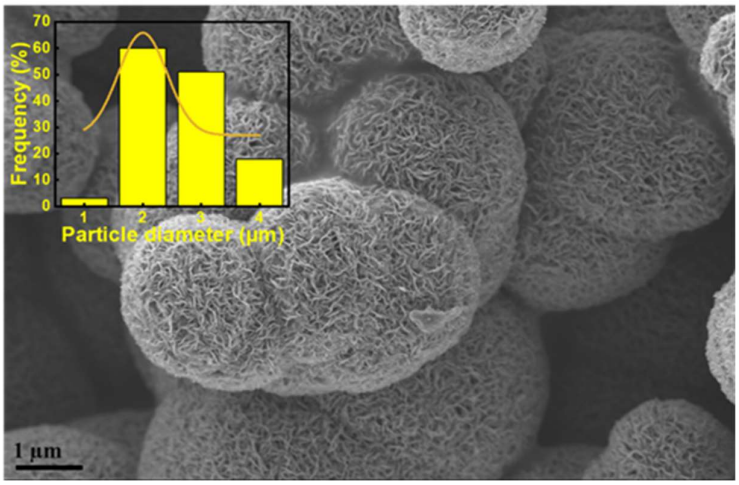

Fig.37 SEM image for MoS_2 prepared without pH adjustment.

High resolution TEM images for MoS_2 samples are shown in **Fig.38**. The entire MoS_2 sample showed the characteristic interlayer distance of 0.64 nm corresponding to the basal (002) MoS_2 planes. The observed differences in their morphologies can be easily distinguished by rounded edges, curved multi-layered fringes for the as-synthesized catalysts (marked via red arrows), and the sharp edges, randomly stacked fringes for the annealed MoS_2 (marked via yellow arrows). The sharper edges and more defect-rich sites are mainly attributed to the additional development of fine MoS_2 crystallites during the annealing treatment of the as-synthesized MoS_2. These enhancements at the edges increase the specific surface area (evident from the textural properties, **Table 17**) of the resultant catalysts and result in the exposure of more HDO active sites. 500-550 MoS_2 slabs were analyzed to obtain the quantitative comparison of the average MoS_2 slab length, stacking degree, MoS_2 dispersion, and the edge-to-corner ratio of MoS_2 slabs (**Table 17**). The annealing pretreatment contributed to an increase in the MoS_2 average slab length which in turn increased the edge to corner ratio of the MoS_2 slabs. The defect-free features and curvy multi-layered structure can be observed in both as-synthesized catalysts. While for the annealed samples, random stacks and sharp edges were observed. These distinct features that can only be observed in the annealed catalysts which corroborate with the existence of greater amounts of defect sites can be seen from its morphology in **Fig.38 (b,d)**.

It is noteworthy to mention that morphology of as-synthesized UNiMoS (**Fig.31a**) shows a similar feature as the annealed MoS_2 in **Fig.38 (b,d)**. Also, the XRD pattern of UNiMoS (**Fig.29b**) shows the characteristics peak of annealed MoS_2 (**Fig.34a**). Hence, UNiMoS was used as such after the hydrothermal synthesis.

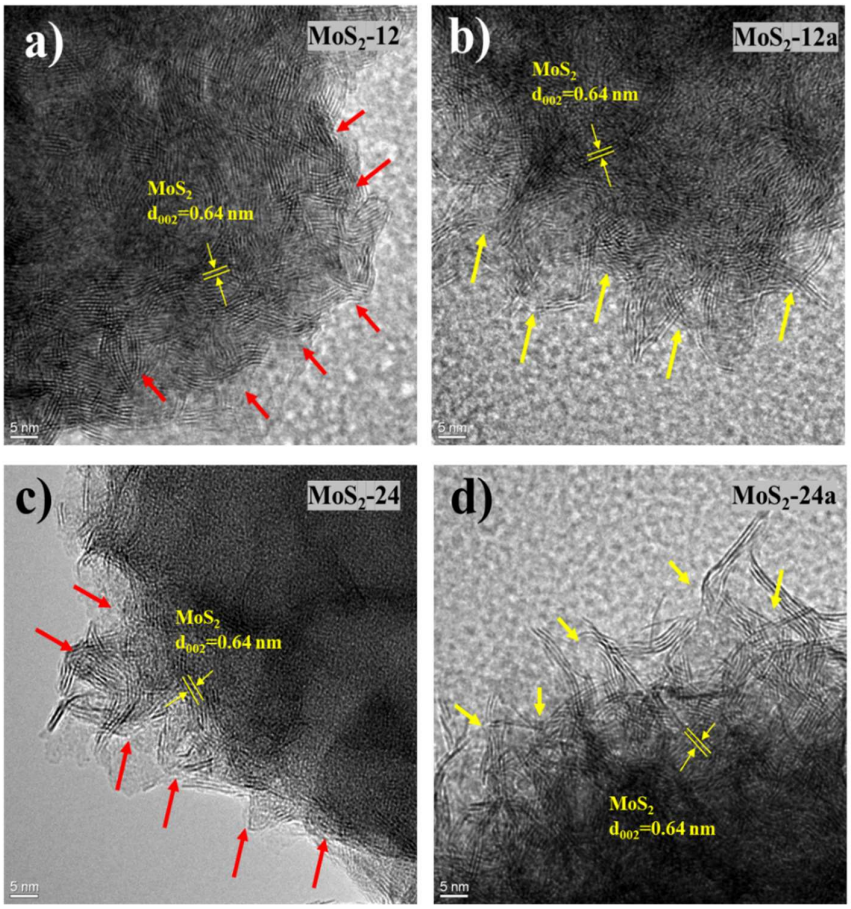

Fig.38 HRTEM images of a) MoS_2-12, b) MoS_2-12a, c) MoS_2-24, and d) MoS_2-24a, with arrows indicating differences in characteristics of particle edges.

4.4.2 HDO of 4-propylguaiacol (PG) over unsupported MoS_2 catalysts

To illustrate the catalytic activity, the as-synthesized and annealed MoS_2 samples were tested for the HDO of 4-propylguaiacol (PG) at 50 bar of total H_2 pressure, 300 °C, and 1000 rpm stirring rate. **Fig.39** shows the comparison of PG conversion and product selectivity after 4 h of hydrotreatment for all catalysts (MoS_2-12, MoS_2-24, MoS_2-12a, and MoS_2-24a). **Fig.40** shows time evolution data (up to 5h) for PG HDO over the MoS_2 catalysts. Based on the evolution of the products and intermediates a reaction network is proposed as shown in **Scheme 6**.

PG undergoes demethoxylation to form 4-propylphenol initially as a lower energy barrier is needed to cleave the methoxy group [148]. Simultaneously, a small degree of demethylation of PG leads to the formation of 4-propylcatechol (referred hereafter as '2O-compounds'). The removal of OH groups (dihydroxylation) via HDO directs these intermediates to form 4-propylbenzene ('aromatics' in **Fig.39** and **Fig.40**) which hydrogenates further to form 4-propylcyclohexene and 4-propylcyclohexane ('cycloalkanes' in **Fig.39** and **Fig.40**). A hydrogenated intermediate, 4-propylcyclohexanol has not been detected in the reaction

mixture which can be due to its rapid disappearance via dehydration to produce propylcyclohexene.

Scheme 6 Reaction scheme for HDO of PG over unsupported MoS_2 at 50 bar total H_2 pressure, 300 ˚C, and 1000 rpm.

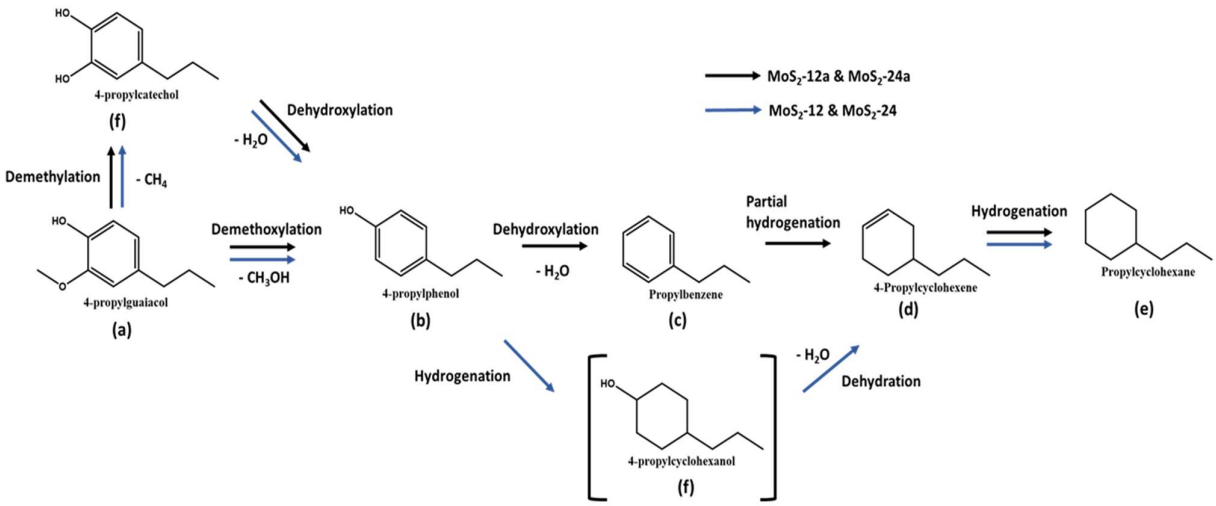

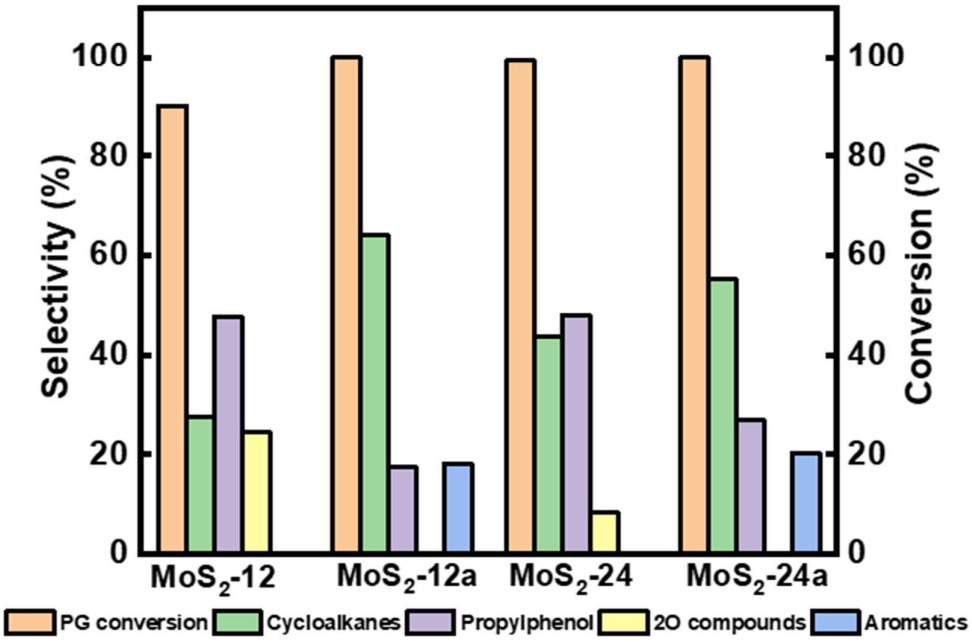

Fig.39 Reaction product selectivity and conversion at 4 h for HDO of PG over MoS_2-12, MoS_2-12a, MoS_2-24, and MoS_2-24a at 50 bar total H2 pressure, 300 ˚C, and 1000 rpm.

A positive influence in the PG conversion can be seen (**Fig.39**) when the MoS_2 synthesis time was extended from 12 (~90 % for MoS_2-12) to 24 h (~100% for MoS_2-24). Both as-synthesized samples also exhibited different selectivity for deoxygenated cycloalkanes like 4-

propylcyclohexane and 4-propylcyclohexene of 27.5 % and 43.4% for MoS_2-12 and MoS_2-24, respectively. Furthermore, the selectivity of 2O-compound was higher for MoS_2-12 (24.7%) as compared to MoS_2-24 (8.3%) after 4 h of reaction.

Both as-synthesized catalysts then underwent thermal annealing at 400 °C for 2 h under nitrogen flow and were further tested for PG HDO. As shown in **Fig.40** after 5h of reaction, deoxygenated cycloalkane selectivity increased to 76.6% and 60.5% for MoS_2-12a and MoS_2-24a respectively as compared to 40% and 49.6% for MoS_2-12 and MoS_2-24. This is due to the rapid conversion of the oxygenated intermediates 4-propylphenol and 4-propylcatechol over the annealed MoS_2 which further confirms the existence of more active sites over them. Indeed, such conversion is faster over MoS_2-12a as evident by the complete deoxygenation of 4-propylphenol, whereas its selectivity reduced to 23.8% for MoS_2-24a after 5 h. It is noteworthy to mention that with the annealed catalysts an aromatic compound, 4-propylbenzene appears after 2 h of reaction, and its selectivity increases thereafter which were mainly due to the direct HDO of 4-propylphenol. After 5 h, the yield of deoxygenated products was found to decrease in the following order: MoS_2-12a (100%) > MoS_2-24a (80.4%) > MoS_2-24 (49.6%) > MoS_2-12 (40.0%). This result demonstrates that the morphology of the synthesized MoS_2 plays a crucial role in determining the catalytic activity. Also, thermal treatment of as-synthesized MoS_2 was found beneficial for HDO reactions due to the morphological changes observed earlier (see Section 4.4.1).

It is clear that PG deoxygenation was improved with longer synthesis time, i.e., MoS_2-24 among the as-synthesized catalysts (**Fig.40(a, c)**). On the other hand, it is the shorter synthesis time one, i.e., MoS_2-12a among annealed catalysts for which PG deoxygenation increases further. This suggests that the 12 h synthesis time is sufficient to nucleate MoS_2 crystallites and the proposed thermal treatment under nitrogen atmosphere can induce morphological changes by further growth of MoS_2 crystals (**Table 17**). As observed the annealed catalysts display longer average MoS_2 slabs which contribute to higher edge to corner Mo atomic ratios. Hydrogenation reactions are thermodynamically preferred on the corner sites while edge-Mo atoms facilitate HDO reactions via sulfur vacancies. Lower edge to corner ratios of MoS_2 slabs for as-synthesized catalysts thus show fewer deoxygenation activities. The observed reactivity of PG thus well correlates to the physicochemical properties of the evolved MoS_2 whether annealed or not.

Besides, the catalytic activity of the as-synthesized and thermally treated MoS_2, the influence of the pH adjustment has been studied for the HDO of PG and the results are shown in **Fig.41**. From **Fig.41 (a, b)**, it is evident that catalytic activity is lower for both samples. Annealing of MoS_2 prepared without pH adjustment shows a negative effect on PG conversion in which 74.2% was achieved after 5 h for the annealed sample whereas 86.6% was reached for the as-synthesized sample. Other product selectivity shows a similar trend except for the high initial selectivity for 4-propyl phenol in the annealed MoS_2 (no acid treatment) (**Fig.41b**). These

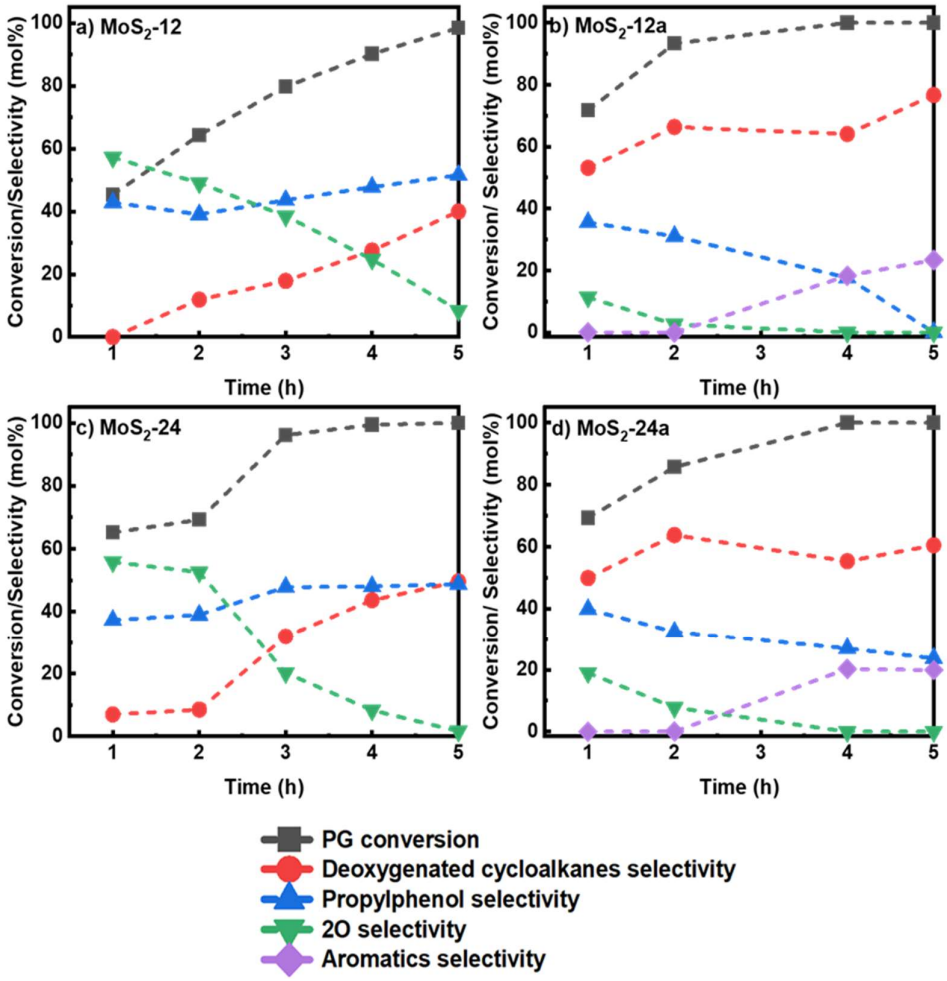

Fig.40 Reaction product distribution for HDO of PG over a) MoS_2-12 b) MoS_2-12a c) MoS_2-24 and d) MoS_2-24a at 50 bar total H_2 pressure, 300 ˚C and 1000 rpm.

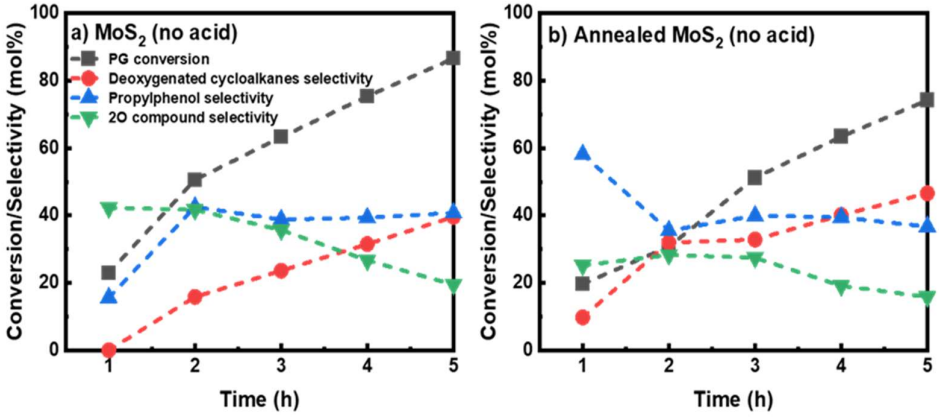

Fig.41. Reaction product distribution for HDO of PG over a) MoS_2 prepared without acid adjustment and b) annealed MoS_2 without acid adjustment at 50 bar total H_2 pressure, 300 ˚C and 1000 rpm.

variations can be attributed to the larger particle size of MoS_2 (Section 4.4.1) providing only small fractions of active sites compared to the pH-modified catalysts. This further demonstrates the importance of acid treatment and annealing to promote the growth of MoS_2 particles which is necessary for HDO activity enhancement.

Furthermore, bulk MoS_2 (Sigma Aldrich) has been studied for PG hydrotreatment and the activity results are outlined in **Fig.42 (a)**. PG conversion after 5h reach 81.3% while it reached ~100% for MoS_2-12a in 4 h. In addition, >70% oxygenated compounds (4-propylphenol and 4-propylcatechol) remained from the bulk MoS_2 after the 5 h experiment compared to a yield of fully deoxygenated cycloalkanes and aromatic compounds from MoS_2-12a. The origin of this difference lies in the textural (**Table 17**) and morphological differences outlined above.

Additionally, the activity of MoS_2/Al_2O_3 (13.2 wt.% Mo, 500 mg total) was compared with MoS_2-12a (66 mg total) using the same model reaction, where an equivalent mass of active metal was used. As can be seen in **Fig.42 (b),** PG conversion reaches ~100% after 2 h compared to 4 h for MoS_2-12a. After 5h HDO, there are only small differences in the cycloalkane selectivity (70.2 vs 76.6%). However, the major difference is the two-fold lower selectivity for deoxygenated aromatics and higher selectivity for 4-propyphenol (17.5 %) after 5h hydrotreatment. These results indicate that the supported catalyst could have higher dispersion of active sites or higher density of active sites per mass active phase (MoS_2) which is beneficial for PG conversion but not the HDO activity. The differences in the HDO activity between the supported and unsupported catalysts could be attributed to the differences in the nature of their active site, i.e., the morphology.

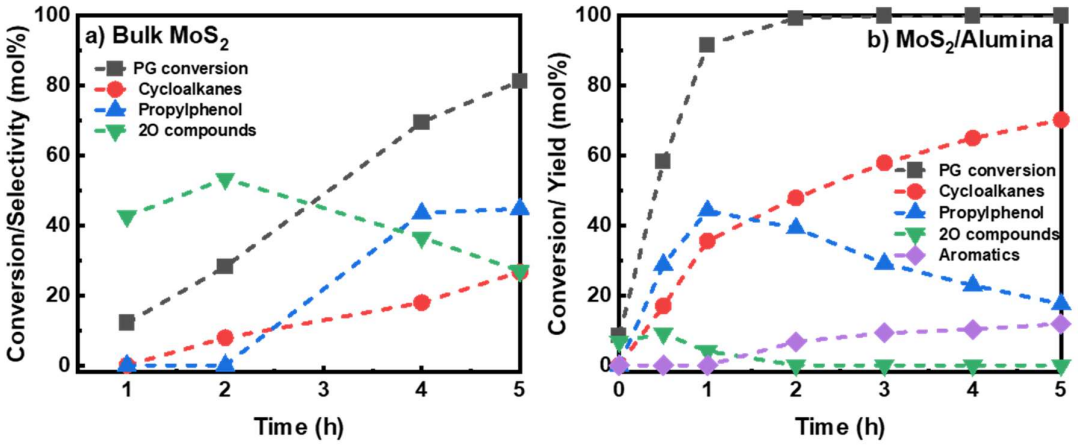

Fig.42 Reaction product distribution for HDO of PG over a) Bulk MoS_2 b) 13.2 wt% MoS_2 supported on alumina at 50 bar total H_2 pressure, 300 ˚C and 1000 rpm.

4.4.3 Hydrotreatment of Kraft lignin over an unsupported MoS_2 and bulk MoS_2

Unsupported MoS_2-12a and commercial MoS_2 were further studied for the hydrotreatment of Kraft lignin at 340 °C and 40 bar of initial H_2 in the autoclave reactor for 5 h, excluding the initial heating time. Hydrotreatment converts the solid lignin to bio-oil containing a spectrum of products mainly phenolics and deoxygenated compounds (cycloalkane and aromatics) with residual solids (termed as char). **Fig. 43** shows the selectivities for each group of products for both catalysts. Bulk MoS_2 depolymerizes the Kraft lignin mainly to phenolic compounds (~90% selectivity) comprising guaiacols and alkylphenols. It also showed a high degree of formation of repolymerized fraction, char (~43% yield). MoS_2-12a, on the other hand, showed 78.6% and 20.1% selectivity for cycloalkane products (methylcyclopentane, cyclohexane, methylcyclohexane, methyl cyclopentane, ethylcyclohexane, and propylcyclohexane, etc.) and deoxygenated aromatic products (toluene, 1,3-dimethylbenzene, and propylbenzene, etc.), respectively. These results are consistent with the model (PG) HDO results discussed above for MoS_2-12a, showing higher hydrogenation and deoxygenation activity which stabilizes more lignin fragments during the depolymerization step and contributes to forming less char (27% char yield) at the end of 5h hydrotreatment.

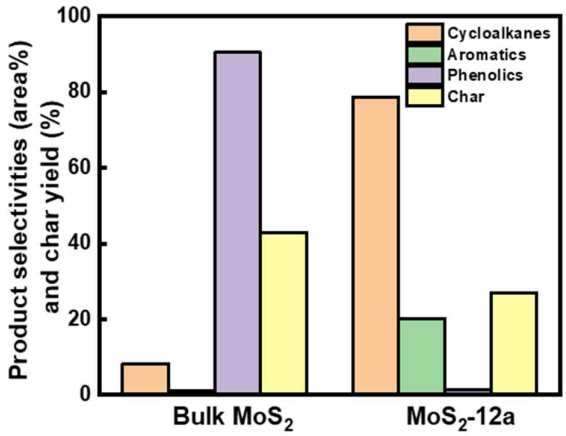

Fig.43 GCMS analysis for the comparison of product selectivities and char yield between bulk MoS_2 and MoS_2-12a for hydrotreatment of Kraft lignin. Reaction conditions: 3:1 lignin to catalyst mass ratio, 340 ˚C, 40 bar initial H2 pressure, 5 h, and 1000 rpm.

5 Concluding remarks and outlook

Valorization of complex feedstocks like Kraft lignin requires selective cleavage of interunit etheric and carbon-carbon linkages (depolymerization), stabilization of the oxygenate fragments, and upgrading (e.g., hydrodeoxygenation) to targeted products (e.g., biofuels, fine chemicals). In this regard, catalytic hydrotreatment has been investigated employing Mo-based sulfides (e.g., MoS_2, NiMoS) supported over γ-Al_2O_3 and/or ultra-stable Y-zeolites or as standalone catalysts to understand their roles. Important insights have been developed in this regard through catalyst preparation, catalyst activation, and characterizations.

Before realizing the Kraft lignin upgradation in this thesis, a detailed literature review for the sulfided catalysts in upgrading renewable feedstocks mainly triglycerides, pyrolysis oil, and lignin has been addressed (paper I). Hydrotreatment of lignin model dimers mimicking common lignin linkages has been performed using sulfided NiMo catalysts to elucidate the effect of support acidity, silica/alumina ratio to the cleavage of recalcitrant lignin dimers, and further upgradation (paper II and III). Kraft lignin hydrotreatment has been conducted in a one-pot process using optimum catalysts from the model studies (paper IV). Unsupported catalysts (MoS_2, NiMoS) have also been studied to elucidate their roles and the roles of the catalyst components in the impregnated catalysts (paper IV and V).

Studies with model lignin dimers revealed that the NiMo sulfide over γ-Al_2O_3 can cleave the etheric linkages easily whereas cleavage of C-C intermediate dimers occurred at only a very slow rate. Y-zeolite incorporation was found to enhance the cleavage of etheric linkages. Transalkylation and isomerization appeared to be a dominant route for C-O-C hydrogenolysis over catalysts with higher Brønsted acidity leading to the formation of C-C-linked stable intermediate phenolic dimers. However, the resultant acidity of the catalyst causes the intermediate phenolic dimers to cleave (C-C scission) yielding more mono-aromatics including benzene, toluene, ethylbenzene, xylene, cresols, and ethyl phenols. Significant C-C scission (>50 %) has also been observed with 5-5’ model linkages over NiMoY even though the initial favored reaction yields dibenzofuran exclusively. Additionally, NiMo sulfides over a series of ultra-stable Y zeolites revealed that Y zeolites with a moderate silica/alumina ratio of 30 (NiMoY30) can facilitate a higher degree of hydrogenolysis, hydrocracking, and deoxygenation reactions involving β-O-4, methylene linked, and 5-5’ linked phenolic dimers leading to the

formation of greater amounts of deoxygenated aromatics and cycloalkanes including BTX. The high activity of the sulfided NiMoY30 could be attributed to the better proximity of the metal sulfide phase and acidic sites, moderate acidity of the catalyst, and higher dispersion of metal sulfides.

NiMoY30 was thus studied with Kraft lignin in a one-pot hydrotreatment at elevated temperature and pressure. One of the major challenges in such a process is to prevent the rapid repolymerization reactions during the thermal degradation of lignin which begins at low temperatures where the catalyst lacks sufficient activity. In absence of catalyst, reductive depolymerization was found to yield greater amounts of repolymerized lignin derived solid residues (~47 wt.%). With NiMoY30, a significant reduction in solid residue formation (~50% reduction compared to without catalyst) was observed. This leads to an improved product yield (~30 wt.%) in the liquid phase with high selectivity to alkylbenzene and monocyclic compounds ((~61%). A comparison of the impregnated NiMoY30 and a similar counterpart of unsupported NiMoS and Y zeolites (a physical mixture), with equal amounts of metals and acid sites, showed further reduction in the solid residue formation (~16.7 wt.%) for the latter. This was due to the enhanced access to the active sites and lignin fragment stabilization compared to the impregnated catalyst. This implies, impregnated NiMoY30 has a diffusion limitation for larger lignin fragments to access the active sites. However, an increase in the active sites by increasing the catalyst loading for NiMoY30 showed reduced solid residue yield (~16.4 wt.%) with a noteworthy monomeric product yield (~39 wt.%). The final liquid also had a remarkable alkylbenzene and monocyclic yield (~31 wt.%) and selectivity (~79%). The physical mixture of unsupported UNiMoS and ultra-stable Y zeolites, on the other hand, shows two-fold lower selectivity to alkylbenzene and monocyclics than NiMoY30 but higher selectivity to mono/alkylphenols, indans/naphthalenes, and polycyclic aromatics. Catalyst characterization demonstrated that the enhanced catalytic hydrogen activation at low temperature (NiMoY30) enhances the lignin depolymerization by stabilizing the lignin fragments/radicals. Moreover, a suitable balance/proximity of deoxygenation and acidic sites for the impregnated catalyst (NiMoY30) was found beneficial for the formation of a high amount of deoxygenated monomeric products despite high solid residue formation.

It has been observed that catalysts show diffusion limitation for large lignin or recombined lignin fragments in a single-pot hydrotreatment process. To further understand the role of transition metal sulfides, lignin derived bio-oil and Kraft lignin has been studied with hydrothermally synthesized unsupported MoS_2. A unique pretreatment step, annealing of hydrothermally prepared MoS_2 under N_2 atmosphere was found beneficial for hydrotreating applications. Among the synthesized catalysts, enhanced deoxygenation and hydrogenation of the bio-oil model compound (propylguaiacol) was observed for an annealed MoS_2 obtained from 12 h of hydrothermal synthesis under pH-controlled conditions. Catalyst characterization revealed that the high activity was due to the reduced particle size, increased surface area, and defect-rich morphology of the MoS_2 leading to the formation of a higher ratio of edge to

corner Mo atoms. As a result, the deoxygenated aromatic fraction was found to increase more than its hydrogenation counterpart. Kraft lignin hydrotreatment with this highly active MoS_2 shows significant char/solid residue suppression and high selectivity for cycloalkane and deoxygenated aromatic products.

The above findings signify that physicochemical properties of the classical NiMo sulfides can be tailored to enable them to be highly active for hydrogenolysis and deoxygenation reaction to valorize lignin and lignin derived bio-oil to value added components (e.g., cycloalkanes, alkylbenzenes, alkylphenols, etc.).

The one-pot process shows promising results in terms of yield, however, a continuous mode of hydrotreatment under a constant hydrogen supply can enable more features to be studied especially the catalyst deactivation. It has been understood that Kraft lignin valorization requires an active and stable catalyst for suppressing solid residue/char formation and delivering a high yield of monomeric fractions at sufficiently low temperature and pressure. To shed more light on this, more affordable transition metal sulfides (Co, W-based sulfides) can further be explored to understand the reaction mechanism, kinetics, and deactivation pathways. Especially the understanding of char formation, mechanisms, and kinetics can help the better design of improved catalysts. Also, the impurities in the feedstock and their impact on catalysts should be a focus for future research rather than a high bio-oil yield. Furthermore, co-processing of petroleum-based feedstock and biomass derived feedstock can provide insights to utilize them from the current biorefinery setup.

6 Acknowledgements

This thesis work is performed at the Competence Centre for Catalysis (KCK) and the division of Chemical engineering at Chalmers University of Technology, Göteborg, Sweden.

I would like to express my humble gratitude to Professor Louise Olsson and Professor Derek for the opportunity to work in such a fascinating field. I acknowledge-

Professor Derek Creaser, my main thesis supervisor for his tireless guidance, discussions, and critical comments to sharpen my work. Thanks for all the informal discussions.

Professor Louise Olsson, my thesis co-supervisors for your support in all matters, inspiration, feedback, and all the fruitful discussions. I highly appreciate your steps for me.

Professor Claes Niklasson for all your motivation and support for me.

Professor Magnus Skoglundh for your feedback and discussion during KCK presentations.

Prakhar Arora, You Wayne Cheah, Hoang Phuoc Ho for your contribution to my research. I appreciate your scientific ideas, the discussions we had. Houman Ojagh for your inputs, help, and inspiration. My officemate, Elham for all the interesting discussions. Diana for all the inspiring discussion and helping with NMR. Rojin, Abdenour, Wei Di, Emma, Jieling, Tobias, Joonsoo, Dawei, Alexander, Joanna, Michael, Marcus, Aqsa, and Maulana for creating such a wonderful atmosphere in KART beyond research and teaching. Previous colleagues, Patric, Pouya, Sreetama, Joby, Poonam, Jesus, Ida, Rasmus, Xavier, Masood, Aiyong, Ximena, Oana, Kunpeng, Lidija, Nadya, Mattias, Mohammad, Soheil for your inspiration and help. Amanda and Simon for their help as bachelor and master thesis students respectively.

All members of this division, competence center for catalysis for their amiable support.

Swedish Energy Agency, and Formas for their funding in such a fascinating field.

Shahjalal University of Science and Technology, Sylhet, Bangladesh where I started my learning in Chemical Engineering.

My two daughters Mahdiya (I will meet you again!) and Mouniya. My wife Mahmuda Akter- I owe to your endless contribution. My mother (Amena Begum), elder brothers, Jafar Ahmmad Mozumdar, and Mohammad Ullah for their guidance and care for me. All my other family members, friends, and others for their support.

7 References

[1] M.A. Salam, P. Arora, H. Ojagh, Y.W. Cheah, L. Olsson, D. Creaser, NiMoS on alumina-USY zeolites for hydrotreating lignin dimers: effect of support acidity and cleavage of C–C bonds, Sustainable Energy & Fuels, 4 (2020) 149-163.
[2] World Energy Outlook 2021, 2021.
[3] Trends and projections in Europe 2021, 2021.
[4] M. Ballesteros, P. Manzanares, Liquid Biofuels, The Role of Bioenergy in the Bioeconomy2019, pp. 113-144.
[5] B.C. Saha, Hemicellulose bioconversion, J. Ind. Microbiol. Biotechnol., 30 (2003) 279-291.
[6] H.D. Hamje, H. Hass, L. Lonza, H. Maas, A. Reid, K. Rose, T. Venderbosch, EU renewable energy targets in 2020: Revised analysis of scenarios for transport fuels, Luxembourg: Publications Office of the European Union, (2014).
[7] R. Rauch, J. Hrbek, H. Hofbauer, Biomass gasification for synthesis gas production and applications of the syngas, Wiley Interdisciplinary Reviews: Energy and Environment, 3 (2014) 343-362.
[8] A.d.R. Pinho, M.B.B. de Almeida, F.L. Mendes, L.C. Casavechia, M.S. Talmadge, C.M. Kinchin, H.L. Chum, Fast pyrolysis oil from pinewood chips co-processing with vacuum gas oil in an FCC unit for second generation fuel production, Fuel, 188 (2017) 462-473.
[9] H. Chen, H. Chen, Lignocellulose biorefinery feedstock engineering, Woodhead Publishing, 2015, pp. 37-86.
[10] I.F. Demuner, J.L. Colodette, A.J. Demuner, C.M. Jardim, Biorefinery review: Wide-reaching products through kraft lignin, BioResources, 14 (2019) 7543-7581.
[11] P.J. de Wild, W.J. Huijgen, A. Kloekhorst, R.K. Chowdari, H.J. Heeres, Biobased alkylphenols from lignins via a two-step pyrolysis - Hydrodeoxygenation approach, Bioresour. Technol., 229 (2017) 160-168.
[12] L. Dong, L. Lin, X. Han, X. Si, X. Liu, Y. Guo, F. Lu, S. Rudić, S.F. Parker, S. Yang, Y. Wang, Breaking the Limit of Lignin Monomer Production via Cleavage of Interunit Carbon–Carbon Linkages, Chem, 5 (2019) 1521-1536.
[13] S. Guadix-Montero, M. Sankar, Review on Catalytic Cleavage of C–C Inter-unit Linkages in Lignin Model Compounds: Towards Lignin Depolymerisation, Top. Catal., 61 (2018) 183-198.
[14] A.V. Bridgwater, Review of fast pyrolysis of biomass and product upgrading, Biomass Bioenergy, 38 (2012) 68-94.
[15] O.İ. Şenol, T.R. Viljava, A.O.I. Krause, Hydrodeoxygenation of methyl esters on sulphided NiMo/γ-Al2O3 and CoMo/γ-Al2O3 catalysts, Catal. Today, 100 (2005) 331-335.
[16] E. Furimsky, Catalytic hydrodeoxygenation, Appl. Catal., A, 199 (2000) 147-190.
[17] P. Arora, H. Ojagh, J. Woo, E. Lind Grennfelt, L. Olsson, D. Creaser, Investigating the effect of Fe as a poison for catalytic HDO over sulfided NiMo alumina catalysts, Appl. Catal., B, 227 (2018) 240-251.

[18] A.E. Coumans, E.J.M. Hensen, A model compound (methyl oleate, oleic acid, triolein) study of triglycerides hydrodeoxygenation over alumina-supported NiMo sulfide, Appl. Catal., B, 201 (2017) 290-301.
[19] D. Kubička, L. Kaluža, Deoxygenation of vegetable oils over sulfided Ni, Mo and NiMo catalysts, Appl. Catal., A, 372 (2010) 199-208.
[20] O.İ. Şenol, T.R. Viljava, A.O.I. Krause, Hydrodeoxygenation of aliphatic esters on sulphided NiMo/γ-Al2O3 and CoMo/γ-Al2O3 catalyst: The effect of water, Catal. Today, 106 (2005) 186-189.
[21] E. Laurent, B. Delmon, Study of the hydrodeoxygenation of carbonyl, carboxylic and guaiacyl groups over sulfided CoMo/γ-Al 2 O 3 and NiMo/γ-Al 2 O 3 catalyst: II. Influence of water, ammonia and hydrogen sulfide, Appl. Catal., A, 109 (1994) 97-115.
[22] P.M. Mortensen, J.D. Grunwaldt, P.A. Jensen, K.G. Knudsen, A.D. Jensen, A review of catalytic upgrading of bio-oil to engine fuels, Appl. Catal., A, 407 (2011) 1-19.
[23] Z. He, X. Wang, Hydrodeoxygenation of model compounds and catalytic systems for pyrolysis bio-oils upgrading, Catalysis for Sustainable Energy, 1 (2012) 28-52.
[24] K. Wu, Y. Liu, W. Wang, Y. Huang, W. Li, Q. Shi, Y. Yang, Preparation of hydrophobic MoS_2, NiS_2-MoS_2 and CoS_2-MoS_2 for catalytic hydrodeoxygenation of lignin-derived phenols, Molecular Catalysis, 477 (2019).
[25] W. Wang, L. Li, K. Wu, K. Zhang, J. Jie, Y. Yang, Preparation of Ni–Mo–S catalysts by hydrothermal method and their hydrodeoxygenation properties, Appl. Catal., A, 495 (2015) 8-16.
[26] W. Wang, K. Zhang, L. Li, K. Wu, P. Liu, Y. Yang, Synthesis of Highly Active Co–Mo–S Unsupported Catalysts by a One-Step Hydrothermal Method for p-Cresol Hydrodeoxygenation, Ind. Eng. Chem. Res., 53 (2014) 19001-19009.
[27] G. Bellussi, G. Rispoli, A. Landoni, R. Millini, D. Molinari, E. Montanari, D. Moscotti, P. Pollesel, Hydroconversion of heavy residues in slurry reactors: Developments and perspectives, J. Catal., 308 (2013) 189-200.
[28] S.S. Coutinho, M.S. Tavares, C.A. Barboza, N.F. Frazão, E. Moreira, D.L. Azevedo, 3R and 2H polytypes of MoS2: DFT and DFPT calculations of structural, optoelectronic, vibrational and thermodynamic properties, J. Phys. Chem. Solids, 111 (2017) 25-33.
[29] H. Topsøe, The role of Co–Mo–S type structures in hydrotreating catalysts, Appl. Catal., A, 322 (2007) 3-8.
[30] B. Hinnemann, Jens K. Nørskov, and Henrik Topsøe, A Density Functional Study of the Chemical Differences between Type I and Type II MoS_2-Based Structures in Hydrotreating Catalysts, J. Phys. Chem. B, 109 (2005) 2245-2253.
[31] Y. Zhu, Q.M. Ramasse, M. Brorson, P.G. Moses, L.P. Hansen, H. Topsøe, C.F. Kisielowski, S. Helveg, Location of Co and Ni promoter atoms in multi-layer MoS2 nanocrystals for hydrotreating catalysis, Catal. Today, 261 (2016) 75-81.
[32] C. Dupont, R. Lemeur, A. Daudin, P. Raybaud, Hydrodeoxygenation pathways catalyzed by MoS_2 and NiMoS active phases: A DFT study, J. Catal., 279 (2011) 276-286.
[33] S. Rangarajan, M. Mavrikakis, On the Preferred Active Sites of Promoted MoS2 for Hydrodesulfurization with Minimal Organonitrogen Inhibition, ACS Catalysis, 7 (2016) 501-509.
[34] H. Wang, H. Ruan, M. Feng, Y. Qin, H. Job, L. Luo, C. Wang, M.H. Engelhard, E. Kuhn, X. Chen, M.P. Tucker, B. Yang, One-Pot Process for Hydrodeoxygenation of Lignin to Alkanes Using Ru-Based Bimetallic and Bifunctional Catalysts Supported on Zeolite Y, ChemSusChem, 10 (2017) 1846-1856.
[35] J. Zakzeski, P.C.A. Bruijnincx, A.L. Jongerius, B.M. Weckhuysen, The Catalytic Valorization of Lignin for the Production of Renewable Chemicals, Chemical Reviews, 110 (2010) 3552-3599.
[36] W. Schutyser, T. Renders, S. Van den Bosch, S.F. Koelewijn, G.T. Beckham, B.F. Sels, Chemicals from lignin: an interplay of lignocellulose fractionation, depolymerisation, and upgrading, Chem. Soc. Rev., 47 (2018) 852-908.
[37] S. Gillet, M. Aguedo, L. Petitjean, A.R.C. Morais, A.M. da Costa Lopes, R.M. Łukasik, P.T. Anastas, Lignin transformations for high value applications: towards targeted modifications using green chemistry, Green Chem., 19 (2017) 4200-4233.

[38] E.L.a.B. Delmon, Influence of Oxygen-, Nitrogen-, and Sulfur-Containing Compounds on the Hydrodeoxygenation of Phenols over Sulfided CoMo/γ-Al_20_3 and NiMo/γ-Al_20_3 Catalysts, Ind. Eng. Chem. Res., 32 (1993) 2516-2524.
[39] C. Zhao, J. He, A.A. Lemonidou, X. Li, J.A. Lercher, Aqueous-phase hydrodeoxygenation of bio-derived phenols to cycloalkanes, J. Catal., 280 (2011) 8-16.
[40] B. Yoosuk, D. Tumnantong, P. Prasassarakich, Unsupported MoS_2 and $CoMoS_2$ catalysts for hydrodeoxygenation of phenol, Chem. Eng. Sci., 79 (2012) 1-7.
[41] S. Echeandia, B. Pawelec, V.L. Barrio, P.L. Arias, J.F. Cambra, C.V. Loricera, J.L.G. Fierro, Enhancement of phenol hydrodeoxygenation over Pd catalysts supported on mixed HY zeolite and Al2O3. An approach to O-removal from bio-oils, Fuel, 117 (2014) 1061-1073.
[42] H. Shafaghat, P.S. Rezaei, W.M. Ashri Wan Daud, Effective parameters on selective catalytic hydrodeoxygenation of phenolic compounds of pyrolysis bio-oil to high-value hydrocarbons, RSC Advances, 5 (2015) 103999-104042.
[43] C. Newman, X. Zhou, B. Goundie, I.T. Ghampson, R.A. Pollock, Z. Ross, M.C. Wheeler, R.W. Meulenberg, R.N. Austin, B.G. Frederick, Effects of support identity and metal dispersion in supported ruthenium hydrodeoxygenation catalysts, Appl. Catal., A, 477 (2014) 64-74.
[44] S. Boullosa-Eiras, R. Lødeng, H. Bergem, M. Stöcker, L. Hannevold, E.A. Blekkan, Catalytic hydrodeoxygenation (HDO) of phenol over supported molybdenum carbide, nitride, phosphide and oxide catalysts, Catal. Today, 223 (2014) 44-53.
[45] X. Zhu, L.L. Lobban, R.G. Mallinson, D.E. Resasco, Bifunctional transalkylation and hydrodeoxygenation of anisole over a Pt/HBeta catalyst, J. Catal., 281 (2011) 21-29.
[46] Q. Tan, G. Wang, A. Long, A. Dinse, C. Buda, J. Shabaker, D.E. Resasco, Mechanistic analysis of the role of metal oxophilicity in the hydrodeoxygenation of anisole, J. Catal., 347 (2017) 102-115.
[47] I.T. Ghampson, G. Pecchi, J.L.G. Fierro, A. Videla, N. Escalona, Catalytic hydrodeoxygenation of anisole over Re-MoO x /TiO 2 and Re-VO x /TiO 2 catalysts, Appl. Catal., B, 208 (2017) 60-74.
[48] D. Shi, L. Arroyo-Ramírez, J.M. Vohs, The use of bimetallics to control the selectivity for the upgrading of lignin-derived oxygenates: Reaction of anisole on Pt and PtZn catalysts, J. Catal., 340 (2016) 219-226.
[49] V.N. Bui, D. Laurenti, P. Afanasiev, C. Geantet, Hydrodeoxygenation of guaiacol with CoMo catalysts. Part I: Promoting effect of cobalt on HDO selectivity and activity, Appl. Catal., B, 101 (2011) 239-245.
[50] I.D. Mora, E. Méndez, L.J. Duarte, S.A. Giraldo, Effect of support modifications for CoMo/γ-Al2O3 and CoMo/ASA catalysts in the hydrodeoxygenation of guaiacol, Appl. Catal., A, 474 (2014) 59-68.
[51] I.D. Mora-Vergara, L. Hernández Moscoso, E.M. Gaigneaux, S.A. Giraldo, V.G. Baldovino-Medrano, Hydrodeoxygenation of guaiacol using NiMo and CoMo catalysts supported on alumina modified with potassium, Catal. Today, 302 (2018) 125-135.
[52] Z. He, M. Hu, X. Wang, Highly effective hydrodeoxygenation of guaiacol on Pt/TiO2: Promoter effects, Catal. Today, 302 (2018) 136-145.
[53] Z. Luo, Z. Zheng, Y. Wang, G. Sun, H. Jiang, C. Zhao, Hydrothermally stable Ru/HZSM-5-catalyzed selective hydrogenolysis of lignin-derived substituted phenols to bio-arenes in water, Green Chem., 18 (2016) 5845-5858.
[54] X. Zhang, T. Wang, L. Ma, Q. Zhang, Y. Yu, Q. Liu, Characterization and catalytic properties of Ni and NiCu catalysts supported on ZrO2–SiO2 for guaiacol hydrodeoxygenation, Catalysis Communications, 33 (2013) 15-19.
[55] X. Lan, E.J.M. Hensen, T. Weber, Hydrodeoxygenation of guaiacol over Ni2P/SiO2–reaction mechanism and catalyst deactivation, Appl. Catal., A, 550 (2018) 57-66.
[56] H.Y. Zhao, D. Li, P. Bui, S.T. Oyama, Hydrodeoxygenation of guaiacol as model compound for pyrolysis oil on transition metal phosphide hydroprocessing catalysts, Appl. Catal., A, 391 (2011) 305-310.
[57] T.R.H. Douglas C. Elliott, Catalytic Hydroprocessing of Chemical Models for Bio-oil, Energy Fuels, 23 (2009) 631-637.

[58] M. Alda-Onggar, P. Maki-Arvela, K. Eranen, A. Aho, J. Hemming, P. Paturi, M. Peurla, M. Lindblad, I.L. Simakova, D.Y. Murzin, Hydrodeoxygenation of Isoeugenol over Alumina-Supported Ir, Pt, and Re Catalysts, ACS Sustain Chem Eng, 6 (2018) 16205-16218.
[59] X. Liu, W. Jia, G. Xu, Y. Zhang, Y. Fu, Selective Hydrodeoxygenation of Lignin-Derived Phenols to Cyclohexanols over Co-Based Catalysts, ACS Sustainable Chemistry & Engineering, 5 (2017) 8594-8601.
[60] P.E. Ruiz, B.G. Frederick, W.J. De Sisto, R.N. Austin, L.R. Radovic, K. Leiva, R. García, N. Escalona, M.C. Wheeler, Guaiacol hydrodeoxygenation on MoS2 catalysts: Influence of activated carbon supports, Catalysis Communications, 27 (2012) 44-48.
[61] X. Li, G. Chen, C. Liu, W. Ma, B. Yan, J. Zhang, Hydrodeoxygenation of lignin-derived bio-oil using molecular sieves supported metal catalysts: A critical review, Renewable and Sustainable Energy Reviews, 71 (2017) 296-308.
[62] M. Saidi, F. Samimi, D. Karimipourfard, T. Nimmanwudipong, B.C. Gates, M.R. Rahimpour, Upgrading of lignin-derived bio-oils by catalytic hydrodeoxygenation, Energy Environ. Sci., 7 (2014) 103-129.
[63] M. Koyama, Hydrocracking of lignin-related model dimers, Bioresour. Technol., 44 (1993) 209-215.
[64] A.L. Jongerius, R. Jastrzebski, P.C.A. Bruijnincx, B.M. Weckhuysen, CoMo sulfide-catalyzed hydrodeoxygenation of lignin model compounds: An extended reaction network for the conversion of monomeric and dimeric substrates, J. Catal., 285 (2012) 315-323.
[65] B. Güvenatam, O. Kurşun, E.H.J. Heeres, E.A. Pidko, E.J.M. Hensen, Hydrodeoxygenation of mono- and dimeric lignin model compounds on noble metal catalysts, Catal. Today, 233 (2014) 83-91.
[66] C. Zhao, J.A. Lercher, Upgrading pyrolysis oil over Ni/HZSM-5 by cascade reactions, Angew Chem Int Ed Engl, 51 (2012) 5935-5940.
[67] W. Zhang, J. Chen, R. Liu, S. Wang, L. Chen, K. Li, Hydrodeoxygenation of Lignin-Derived Phenolic Monomers and Dimers to Alkane Fuels over Bifunctional Zeolite-Supported Metal Catalysts, ACS Sustainable Chemistry & Engineering, 2 (2014) 683-691.
[68] Y.-K. Hong, D.-W. Lee, H.-J. Eom, K.-Y. Lee, The catalytic activity of Pd/WOx/γ-Al2O3 for hydrodeoxygenation of guaiacol, Appl. Catal., B, 150-151 (2014) 438-445.
[69] M. Talibi, P. Hellier, N. Ladommatos, Impact of increasing methyl branches in aromatic hydrocarbons on diesel engine combustion and emissions, Fuel, 216 (2018) 579-588.
[70] J. García-Martínez, M. Johnson, J. Valla, K. Li, J.Y. Ying, Mesostructured zeolite Y—high hydrothermal stability and superior FCC catalytic performance, Catalysis Science & Technology, 2 (2012).
[71] M. Williams, B. Fonfe, C. Sievers, A. Abraham, J. Vanbokhoven, A. Jentys, J. Vanveen, J. Lercher, Hydrogenation of tetralin on silica–alumina-supported Pt catalysts I. Physicochemical characterization of the catalytic materials, J. Catal., 251 (2007) 485-496.
[72] K. Wu, W. Wang, H. Guo, Y. Yang, Y. Huang, W. Li, C. Li, Engineering Co Nanoparticles Supported on Defect MoS_{2-x} for Mild Deoxygenation of Lignin-Derived Phenols to Arenes, ACS Energy Letters, 5 (2020) 1330-1336.
[73] W. Song, S. Zhou, S. Hu, W. Lai, Y. Lian, J. Wang, W. Yang, M. Wang, P. Wang, X. Jiang, Surface Engineering of CoMoS Nanosulfide for Hydrodeoxygenation of Lignin-Derived Phenols to Arenes, ACS Catalysis, 9 (2018) 259-268.
[74] J. Cao, A. Li, Y. Zhang, L. Mu, X. Huang, Y. Li, T. Yang, C. Zhang, C. Zhou, Highly efficient unsupported Co-doped nano-MoS2 catalysts for p-cresol hydrodeoxygenation, Molecular Catalysis, 505 (2021).
[75] G. Liu, A.W. Robertson, M.M.-J. Li, W.C.H. Kuo, M.T. Darby, M.H. Muhieddine, Y.-C. Lin, K. Suenaga, M. Stamatakis, J.H. Warner, S.C.E. Tsang, MoS_2 monolayer catalyst doped with isolated Co atoms for the hydrodeoxygenation reaction, Nat. Chem., (2017).
[76] X. Liu, X. Hou, Y. Zhang, H. Yuan, X. Hong, G. Liu, In Situ Formation of CoMoS Interfaces for Selective Hydrodeoxygenation of p-Cresol to Toluene, Ind. Eng. Chem. Res., 59 (2020) 15921-15928.

[77] C. García-Mendoza, C.E. Santolalla-Vargas, L.G. Woolfolk, P. del Ángel, J.A. de los Reyes, Effect of TiO2 in supported NiWS catalysts for the hydrodeoxygenation of guaiacol, Catal. Today, 377 (2021) 145-156.
[78] L. Shuai, J. Sitison, S. Sadula, J. Ding, M.C. Thies, B. Saha, Selective C–C Bond Cleavage of Methylene-Linked Lignin Models and Kraft Lignin, ACS Catalysis, 8 (2018) 6507-6512.
[79] W. Song, W. Lai, Y. Lian, X. Jiang, W. Yang, Sulfated ZrO_2 supported CoMo sulfide catalyst by surface exsolution for enhanced hydrodeoxygenation of lignin-derived ethers to aromatics, Fuel, 263 (2020).
[80] C. Zhang, J. Lu, X. Zhang, K. MacArthur, M. Heggen, H. Li, F. Wang, Cleavage of the lignin β-O-4 ether bond via a dehydroxylation–hydrogenation strategy over a NiMo sulfide catalyst, Green Chem., 18 (2016) 6545-6555.
[81] C. Zhang, H. Li, J. Lu, X. Zhang, K.E. MacArthur, M. Heggen, F. Wang, Promoting Lignin Depolymerization and Restraining the Condensation via an Oxidation−Hydrogenation Strategy, ACS Catalysis, 7 (2017) 3419-3429.
[82] J. He, L. Lu, C. Zhao, D. Mei, J.A. Lercher, Mechanisms of catalytic cleavage of benzyl phenyl ether in aqueous and apolar phases, J. Catal., 311 (2014) 41-51.
[83] Z. Luo, C. Zhao, Mechanistic insights into selective hydrodeoxygenation of lignin-derived β-O-4 linkage to aromatic hydrocarbons in water, Catal. Sci. Technol., 6 (2016) 3476-3484.
[84] S. Mukundan, L. Atanda, J. Beltramini, Thermocatalytic cleavage of C–C and C–O bonds in model compounds and kraft lignin by NiMoS2/C nanocatalysts, Sustainable Energy & Fuels, 3 (2019) 1317-1328.
[85] Z. Ma, J.A. van Bokhoven, Deactivation and Regeneration of H-USY Zeolite during Lignin Catalytic Fast Pyrolysis, ChemCatChem, 4 (2012) 2036-2044.
[86] Z. Ma, E. Troussard, J.A. van Bokhoven, Controlling the selectivity to chemicals from lignin via catalytic fast pyrolysis, Appl. Catal., A, 423-424 (2012) 130-136.
[87] A.K. Deepa, P.L. Dhepe, Solid acid catalyzed depolymerization of lignin into value added aromatic monomers, RSC Advances, 4 (2014).
[88] S.G.A. Ferraz, B.M. Santos, F.M.Z. Zotin, L.R.R. Araujo, J.L. Zotin, Influence of Support Acidity of NiMo Sulfide Catalysts for Hydrogenation and Hydrocracking of Tetralin and Its Reaction Intermediates, Ind. Eng. Chem. Res., 54 (2015) 2646-2656.
[89] S.G.A. Ferraz, F.M.Z. Zotin, L.R.R. Araujo, J.L. Zotin, Influence of support acidity of NiMoS catalysts in the activity for hydrogenation and hydrocracking of tetralin, Appl. Catal., A, 384 (2010) 51-57.
[90] J.-I. Park, J.-K. Lee, J. Miyawaki, Y.-K. Kim, S.-H. Yoon, I. Mochida, Hydro-conversion of 1-methyl naphthalene into (alkyl)benzenes over alumina-coated USY zeolite-supported NiMoS catalysts, Fuel, 90 (2011) 182-189.
[91] M.O. Kazakov, K.A. Nadeina, I.G. Danilova, P.P. Dik, O.V. Klimov, V.Y. Pereyma, E.A. Paukshtis, I.S. Golubev, I.P. Prosvirin, E.Y. Gerasimov, I.V. Dobryakova, E.E. Knyazeva, I.I. Ivanova, A.S. Noskov, Influence of USY zeolite recrystallization on physicochemical properties and catalytic performance of NiMo/USY-Al2O3 hydrocracking catalysts, Catal. Today, (2019).
[92] K. Sato, Y. Nishimura, K. Honna, N. Matsubayashi, H. Shimada, Role of HY Zeolite Mesopores in Hydrocracking of Heavy Oils, J. Catal., 200 (2001) 288-297.
[93] M.O. Kazakov, K.A. Nadeina, I.G. Danilova, P.P. Dik, O.V. Klimov, V.Y. Pereyma, E.Y. Gerasimov, I.V. Dobryakova, E.E. Knyazeva, I.I. Ivanova, A.S. Noskov, Hydrocracking of vacuum gas oil over NiMo/Y-Al 2 O 3 : Effect of mesoporosity introduced by zeolite Y recrystallization, Catal. Today, 305 (2018) 117-125.
[94] Z. Cao, X. Zhang, C. Xu, X. Huang, Z. Wu, C. Peng, A. Duan, Selective hydrocracking of light cycle oil into high-octane gasoline over bi-functional catalysts, Journal of Energy Chemistry, 52 (2021) 41-50.
[95] D. Kubička, N. Kumar, P. Mäki-Arvela, M. Tiitta, V. Niemi, T. Salmi, D.Y. Murzin, Ring opening of decalin over zeolitesI. Activity and selectivity of proton-form zeolites, J. Catal., 222 (2004) 65-79.

[96] J. Garcia-Martinez, K. Li, G. Krishnaiah, A mesostructured Y zeolite as a superior FCC catalyst--lab to refinery, Chem Commun (Camb), 48 (2012) 11841-11843.
[97] B.M. Santos, W. Zhao, J.L. Zotin, M.A.P.d. Silva, L. Oliviero, F. Maugé, Impact of proximity between NiMoS and zeolitic HY sites on cyclohexene hydroconversion: An infrared operando study of sulfide catalysts, J. Catal., 396 (2021) 92-103.
[98] J. Horáček, F. Homola, I. Kubičková, D. Kubička, Lignin to liquids over sulfided catalysts, Catal. Today, 179 (2012) 191-198.
[99] J. Pu, N. Thanh-Son, E. Leclerc, C. Lorentz, D. Laurenti, I. Pitault, M. Tayakout-Fayolle, C. Geantet, Lignin catalytic hydroconversion in a semi-continuous reactor: An experimental study, Applied Catalysis B-Environmental, 256 (2019).
[100] R.A. Anja Oasmaa, Dietrich Meier, CATALYTIC HYDROTREATMENT OF SOME TECHNICAL LIGNINS, Bioresour. Technol., 45 (1993) 189-194.
[101] R. DietrichMeier, OskarFaix, Catalytic hydropyrolysis of lignin: Influence of reaction conditions on the formation and composition of liquid products, Bioresour. Technol., 40 (1992).
[102] C.R. Kumar, N. Anand, A. Kloekhorst, C. Cannilla, G. Bonura, F. Frusteri, K. Barta, H.J. Heeres, Solvent free depolymerization of Kraft lignin to alkyl-phenolics using supported NiMo and CoMo catalysts, Green Chem., 17 (2015) 4921-4930.
[103] A. Narani, R.K. Chowdari, C. Cannilla, G. Bonura, F. Frusteri, H.J. Heeres, K. Barta, Efficient catalytic hydrotreatment of Kraft lignin to alkylphenolics using supported NiW and NiMo catalysts in supercritical methanol, Green Chem., 17 (2015) 5046-5057.
[104] S.G. Parto, J.M. Christensen, L.S. Pedersen, A.B. Hansen, F. Tjosås, C. Spiga, C.D. Damsgaard, D.B. Larsen, J.Ø. Duus, A.D. Jensen, Liquefaction of Lignosulfonate in Supercritical Ethanol Using Alumina-Supported NiMo Catalyst, Energy & Fuels, 33 (2019) 1196-1209.
[105] D. Kubička, J. Horáček, Deactivation of HDS catalysts in deoxygenation of vegetable oils, Appl. Catal., A, 394 (2011) 9-17.
[106] M. Argyle, C. Bartholomew, Heterogeneous Catalyst Deactivation and Regeneration: A Review, Catalysts, 5 (2015) 145-269.
[107] C.H. Bartholomew, Mechanisms of catalyst deactivation, Appl. Catal., A, 212 (2001) 17-60.
[108] O.İ. Şenol, T.R. Viljava, A.O.I. Krause, Effect of sulphiding agents on the hydrodeoxygenation of aliphatic esters on sulphided catalysts, Appl. Catal., A, 326 (2007) 236-244.
[109] H. Ojagh, D. Creaser, S. Tamm, P. Arora, S. Nyström, E. Lind Grennfelt, L. Olsson, Effect of Dimethyl Disulfide on Activity of NiMo Based Catalysts Used in Hydrodeoxygenation of Oleic Acid, Ind. Eng. Chem. Res., 56 (2017) 5547-5557.
[110] P.M. Mortensen, D. Gardini, C.D. Damsgaard, J.-D. Grunwaldt, P.A. Jensen, J.B. Wagner, A.D. Jensen, Deactivation of Ni-MoS2 by bio-oil impurities during hydrodeoxygenation of phenol and octanol, Appl. Catal., A, 523 (2016) 159-170.
[111] M. Badawi, J.F. Paul, S. Cristol, E. Payen, Y. Romero, F. Richard, S. Brunet, D. Lambert, X. Portier, A. Popov, E. Kondratieva, J.M. Goupil, J. El Fallah, J.P. Gilson, L. Mariey, A. Travert, F. Maugé, Effect of water on the stability of Mo and CoMo hydrodeoxygenation catalysts: A combined experimental and DFT study, J. Catal., 282 (2011) 155-164.
[112] E. Laurent, B. Delmon, Influence of water in the deactivation of a sulfided NiMoγ-Al2O3 catalyst during hydrodeoxygenation, J. Catal., 146 (1994) 281-291.
[113] F. Diez, B.C. Gates, J.T. Miller, D.J. Sajkowski, S.G. Kukes, Deactivation of a nickel-molybdenum/. gamma.-alumina catalyst: influence of coke on the hydroprocessing activity, Ind. Eng. Chem. Res., 29 (1990) 1999-2004.
[114] M.G.P. Magnoux, Organic chemistry of coke formation, Appl. Catal., A, 212 (2001) 83-96.
[115] E. Furimsky, F.E. Massoth, Deactivation of hydroprocessing catalysts, Catal. Today, 52 (1999) 381-495.
[116] S. Eijsbouts, X. Li, J. Bergwerff, J. Louwen, L. Woning, J. Loos, Nickel sulfide crystals in Ni-Mo and Ni-W catalysts: Eye-catching inactive feature or an active phase in its own right?, Catal. Today, 292 (2017) 38-50.

[117] B. Guichard, M. Roy-Auberger, E. Devers, C. Legens, P. Raybaud, Aging of Co(Ni)MoP/Al2O3 catalysts in working state, Catal. Today, 130 (2008) 97-108.
[118] M. Abdus Salam, D. Creaser, P. Arora, S. Tamm, E. Lind Grennfelt, L. Olsson, Influence of Bio-Oil Phospholipid on the Hydrodeoxygenation Activity of NiMoS/Al2O3 Catalyst, Catalysts, 8 (2018) 418.
[119] H. Ojagh, D. Creaser, M.A. Salam, E.L. Grennfelt, L. Olsson, Hydroconversion of abietic acid into value-added fuel components and chemicals over sulfided NiMo catalysts with varying support acidity Fuel Process. Technol., 190 (2019) 55-66.
[120] H. Ojagh, D. Creaser, S. Tamm, P. Arora, S. Nyström, E. Lind Grennfelt, L. Olsson, Effect of Dimethyl Disulfide on Activity of NiMo Based Catalysts Used in Hydrodeoxygenation of Oleic Acid, Ind. Eng. Chem. Res., (2017).
[121] W.-C. CHENG, K. RAJAGOPALAN, Conversion of Cyclohexene over Y-Zeolites: A Model Reaction for Hydrogen Transfer, J. Catal., 119 (1989) 354-358.
[122] C. Li, X. Zhao, A. Wang, G.W. Huber, T. Zhang, Catalytic Transformation of Lignin for the Production of Chemicals and Fuels, Chem. Rev., 115 (2015) 11559-11624.
[123] S. KRISHNAMURTHY, S. PANVELKER, Y.T. SHAH, Hydrodeoxygenation of Dibenzofuran and Related Compounds, AIChE J., 27 (1989) 994-1001.
[124] J. Zhang, C. Li, X. Chen, W. Guan, C. Liang, Insights into the reaction pathway of hydrodeoxygenation of dibenzofuran over MgO supported noble-metals catalysts, Catal. Today, 319 (2019) 155-163.
[125] J. Zhang, C. Li, X. Chen, Y. Chen, L. Zhang, B. Zhang, C. Liang, Promotional effects of magnesia on catalytic performance of Pt/SiO2 in hydrogenolysis of dibenzofuran, J. Catal., 371 (2019) 346-356.
[126] J. Zhang, L. Wang, C. Li, S. Jin, C. Liang, Selective Hydrogenolysis of Dibenzofuran over Highly Efficient Pt/MgO Catalysts to o-Phenylphenol, Organic Process Research & Development, 22 (2018) 67-76.
[127] L. Wang, H. Wan, S. Jin, X. Chen, C. Li, C. Liang, Hydrodeoxygenation of dibenzofuran over SiO2, Al2O3/SiO2 and ZrO2/SiO2 supported Pt catalysts, Catalysis Science & Technology, 5 (2015) 465-474.
[128] H.H. Ingelsten, M. Skoglundh, E. Fridell, Influence of the support acidity of Pt/aluminum-silicate catalysts on the continuous reduction of NO under lean conditions, Appl. Catal., B, 41 (2003) 287-300.
[129] R.J. Gorte, What do we know about the acidity of solid acids?, Catal. Lett., 62 (1999) 1-13.
[130] A. Wang, B. Lin, H. Zhang, M.H. Engelhard, Y. Guo, G. Lu, C.H.F. Peden, F. Gao, Ambient temperature NO oxidation over Cr-based amorphous mixed oxide catalysts: effects from the second oxide components, Catalysis Science & Technology, 7 (2017) 2362-2370.
[131] W. Zhou, Y. Zhou, Q. Wei, L. Du, S. Ding, S. Jiang, Y. Zhang, Q. Zhang, Gallium Modified HUSY Zeolite as an Effective Co-support for NiMo Hydrodesulfurization Catalyst and the Catalyst's High Isomerization Selectivity, Chemistry, 23 (2017) 9369-9382.
[132] N. Kunisada, K.-H. Choi, Y. Korai, I. Mochida, K. Nakano, Novel zeolite based support for NiMo sulfide in deep HDS of gas oil, Appl. Catal., A, 269 (2004) 43-51.
[133] W. Zhou, M. Liu, Q. Zhang, Q. Wei, S. Ding, Y. Zhou, Synthesis of NiMo Catalysts Supported on Gallium-Containing Mesoporous Y Zeolites with Different Gallium Contents and Their High Activities in the Hydrodesulfurization of 4,6-Dimethyldibenzothiophene, ACS Catalysis, 7 (2017) 7665-7679.
[134] E.J.M. Hensen, J.A.R. van Veen, Encapsulation of transition metal sulfides in faujasite zeolite for hydroprocessing applications, Catal. Today, 86 (2003) 87-109.
[135] H. Wang, M. Feng, B. Yang, Catalytic hydrodeoxygenation of anisole: an insight into the role of metals in transalkylation reactions in bio-oil upgrading, Green Chem., 19 (2017) 1668-1673.
[136] Q. Yan, J. Li, J. Zhang, Z. Cai, Thermal Decomposition of Kraft Lignin under Gas Atmospheres of Argon, Hydrogen, and Carbon Dioxide, Polymers, 10 (2018).
[137] J. Weitkamp, Catalytic Hydrocracking-Mechanisms and Versatility of the Process, ChemCatChem, 4 (2012) 292-306.
[138] Y. Zhang, F. Lu, L. Pan, Y. Xu, Y. Yang, Y. Bando, D. Golberg, J. Yao, X. Wang, Improved cycling stability of NiS2 cathodes through designing a “kiwano” hollow structure, Journal of Materials Chemistry A, 6 (2018) 11978-11984.

[139] G.A.J.A. Manish Chhowalla, Thin films of fullerene-like MoS_2 nanoparticles with ultra-low friction and wear, Chhowalla, Manish, and Gehan AJ Amaratunga. "Thin films of fullerene-like MoS_2 nanoparticles with ultra-low friction and wear." 407.6801 (2000): 164-167., Nature, 407 (2000) 164-167.
[140] L. Yang, X. Cui, J. Zhang, K. Wang, M. Shen, S. Zeng, S.A. Dayeh, L. Feng, B. Xiang, Lattice strain effects on the optical properties of MoS2 nanosheets, Sci Rep, 4 (2014) 5649.
[141] X. Xi, F. Zeng, H. Cao, C. Cannilla, T. Bisswanger, S. de Graaf, Y. Pei, F. Frusteri, C. Stampfer, R. Palkovits, H.J. Heeres, Enhanced C3+ alcohol synthesis from syngas using KCoMoSx catalysts: effect of the Co-Mo ratio on catalyst performance, Appl. Catal., B, 272 (2020).
[142] N. Li, L. Wei, R. bibi, L. Chen, J. Liu, L. Zhang, Y. Zheng, J. Zhou, Catalytic hydrogenation of alkali lignin into bio-oil using flower-like hierarchical MoS_2 -based composite catalysts, Fuel, 185 (2016) 532-540.
[143] M.F. Wagenhofer, H. Shi, O.Y. Gutiérrez, A. Jentys, J.A. Lercher, Enhancing hydrogenation activity of Ni-Mo sulfide hydrodesulfurization catalysts, Science Advances, 6 (2020) eaax5331.
[144] H. Lin, X. Chen, H. Li, M. Yang, Y. Qi, Hydrothermal synthesis and characterization of MoS2 nanorods, Mater. Lett., 64 (2010) 1748-1750.
[145] J.C. F. Solymosi , A. Szöke , T. Bánsági and A. Oszkó, Aromatization of Methane over Supported and Unsupported Mo-Based Catalysts, J. Catal., 165 (1997) 150-161.
[146] G.M. Bremmer, L. van Haandel, E.J.M. Hensen, J.W.M. Frenken, P.J. Kooyman, The effect of oxidation and resulfidation on (Ni/Co)MoS2 hydrodesulfurisation catalysts, Appl. Catal., B, 243 (2019) 145-150.
[147] D.G. L. Benoist , G. Pfister-Guillouzo , E. Schmidt , G. Meunier and A. Levasseur, XPS analysis of oxido-reduction mechanisms during lithium intercalation in amorphous molybdenum oxysulfide thin films, Solid State Ionics, 76 (1995) 81-89.
[148] L. Bomont, M. Alda-Onggar, V. Fedorov, A. Aho, J. Peltonen, K. Eränen, M. Peurla, N. Kumar, J. Wärnå, V. Russo, P. Mäki-Arvela, H. Grénman, M. Lindblad, D.Y. Murzin, Production of Cycloalkanes in Hydrodeoxygenation of Isoeugenol Over Pt- and Ir-Modified Bifunctional Catalysts, Eur. J. Inorg. Chem., 2018 (2018) 2841-2854.